Development of Novel Devices and Methods for Blood Pressure Measurement

Sub-title: Design and Validation of Mercury-free BP apparatus – Merkfree, and a new AI driven method for measurement of BP using ultrasound.

A Thesis Submitted

In Partial Fulfillment of the Requirements

for the Degree of

Doctor of Philosophy

by

"Ravinder Kumar"

(2018bmz0007)

DEPARTMENT OF BIOMEDICAL ENGINEERING
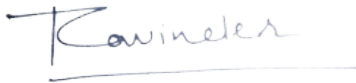
INDIAN INSTITUTE OF TECHNOLOGY ROPAR

May 2023

Ravinder Kumar: *Development of Novel Devices and Methods for Blood Pressure Measurement*

DEDICATED

TO

FAMILY & FRIENDS

DECLARATION

I hereby declare that the work described in the thesis entitled **"Development of Novel Devices and Methods for Blood Pressure measurement"** submitted for the degree of **Doctor of Philosophy** in Biomedical Engineering to the Indian Institute of Technology Ropar has been carried out under the supervision of **Dr. Ashish Kumar Sahani**. This thesis is the result of my own independent investigation, except where otherwise stated. I have acknowledged all the other sources by stating the references explicitly. I declare that any idea/data/fact/source stated in my thesis has not been fabricated/falsified/misrepresented. All the principles of academic honesty and integrity have been followed. I understand that any violation of the above will be cause for disciplinary action by the Institute and can also evoke penal action from the sources which have thus not been properly cited or from whom proper permission has not been taken when needed. I hereby give consent for my thesis, if accepted, to be available online in the Institute's Open Access repository and for inter-library loan, and for the title and abstract to be made available to outside organizations.

Name: Ravinder Kumar

Entry Number:2018bmz0007

Program: PhD

Department: Biomedical Engineering

Indian Institute of Technology Ropar

Rupnagar, Punjab, 140001

Date: 17 May 2023

ACKNOWLEDGMENTS

CERTIFICATE

This is to certify that the thesis entitled **Development of Novel Devices and Methods for Blood Pressure Measurement,** submitted by **Ravinder Kumar** (2018bmz0007) for the award of the degree of **Doctor of Philosophy** of Indian Institute of Technology Ropar, is a record of bonafide research work carried out under my guidance and supervision. To the best of my knowledge and belief, the work presented in this thesis is original and has not been submitted, either in part or full, for the award of any other degree, diploma, fellowship, associateship or similar title of any university or institution. In my opinion, the thesis has reached the standard fulfilling the requirements of the regulations relating to the Degree.

Dr Ashish Kumar Sahani,

Research Supervisor

Department of Biomedical Engineering

Date: 17 May 2023

Indian Institute of Technology Ropar
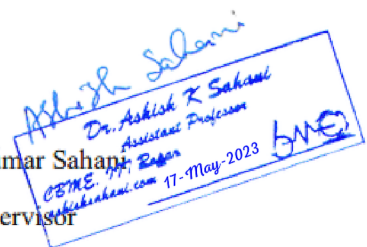
ABSTRACT

Hypertension, a common condition that affects over 25% of the global population, is a significant risk factor for various cardiovascular and renal complications. It is also a leading cause of death worldwide. In India, hypertension is responsible for a significant number of stroke deaths (57%) and coronary heart disease deaths (24%). Accurate measurement of blood pressure is critical for managing hypertension and reducing the risk of cardiovascular morbidity and mortality. This thesis presents research on developing new blood pressure monitoring technologies that can potentially replace traditional methods that use mercury. The focus is on two specific methods: a mercury-free sphygmomanometer called Merkfree and a cuffless method using ultrasound. We have developed Merkfree, which is a mercury-free sphygmomanometer that looks, feels and operates just like a traditional mercury sphygmomanometer. It uses Galinstan as a substitute for mercury which is a non-toxic alloy of Gallium, Indium and Tin. Galinstan is nearly half as dense as mercury and sticks to glass. To work with the lower density, an enclosure and scale that is nearly double the length of MS was designed. The issue of stickiness with glass was resolved by maintaining a small meniscus of a reducing agent in the measuring tube and tank of Merkfree. Clinical trials have been conducted to validate the accuracy of Merkfree against MS and oscillometric sphygmomanometer (OS) over 252 patients at DMC&H, Ludhiana. The results show a good correlation of the systolic and diastolic BP measurements from Merkfree with respect to MS and the OS. The mean absolute percentage error is less than 10% for both systolic blood pressure (SBP) and diastolic blood pressure (DBP). We also found that Merkfree has lower rounding-off errors compared to MS.

Another direction that we have explored is cuffless measurement of BP using ultrasound. In this method, the arterial wall is pushed with an acoustic radiation push impulse (ARFI). After the completion of the ARFI pulse, the artery undergoes impulsive unloading which stimulates a hoop mode vibration. The author designed two machine learning (ML) models which make it possible to estimate the internal pressure of the artery using ultrasonically measurable parameters. To generate the training data for the ML models, extensive FEM eigen frequency simulations were done for different tubes under pressure by sweeping through a range of values for inner lumen diameter (ILD), tube density (TD), elastic modulus, internal pressure (IP), tube length, and Poison's ratio. Through image processing applied on images of different eigen modes supported for each simulated case, the hoop mode frequency (HMF) was identified. Two different ML models were designed based on the simulated data. One is a four-parameter model (FPM) that takes TT, TD, ILD, and HMF as the inputs and gives out IP as output. Second is a three-parameter model (TPM) that takes TT, ILD, HMF as inputs and IP as output. In addition to the accuracy of these models on simulated data, their performance was verified experimentally on two arterial phantoms at a range of pressures.

In conclusion, this thesis presents new blood pressure monitoring technologies that can potentially replace traditional methods that use mercury. The focus is on two methods: a mercury-free sphygmomanometer called Merkfree and a cuffless method using ultrasound. Both methods have been tested and shown to have good correlation with traditional methods and have the potential for use in clinical settings. These technologies can aid in achieving the goal of eliminating mercury from healthcare while also providing accurate and accessible blood pressure measurement for clinicians and patients.

Keywords: Hypertension, Blood pressure, Merkfree, Acoustic radiation push impulse (ARFI), Ultrasound, Galinstan, 3D printing, Superhydrophobic coatings, Physical Vapor Deposition (PVD), Auscl-D, Machine learning (ML), Hoop mode frequency (HMF).

LIST OF PUBLICATIONS

Journal papers

1. **R. Kumar**, A. K. Sahani, and G. S. Wander, "A survey to gauge confidence of Indian clinicians on three primary devices for blood pressure measurement," Blood Press. Monit., pp. 196–199, 2021.

2. V. Kumar, **R. Kumar,** M. Kumar, G. S. Wander, and A. Sahani, "Auscl-D: a mercury-free digital auscultatory sphygmomanometer," J. Med. Eng. Technol., pp. 1–8, Jul. 2021.

3. **R. Kumar** and A. Sahani, "Role of superhydrophobic coatings in biomedical applications," Mater. Today Proc., vol. 45, Mar. 2021.

4. **R. Kumar**, S. Jallu, K. Pasricha, B. Basumatary, B. P. S. Parmar, and A. K. Sahani, "Laparoscopic Lens Defogging: a Review of Methods to Maintain a Clear Operating Field," Indian J. Surg., 2021.

5. **R. Kumar**, V.Ghai, and A. K. Sahani, "A surface modification approach to overcome wetting behaviour of gallium based liquid metal droplets," IEEE Transactions in Nanotechnology., 2021.

6. **R. Kumar**, M. Kumar, G. S. Wander, and A. K. Sahani, "Concept, hardware development, and clinical trials of a Galinstan based Mercury free sphygmomanometer: Merkfree," Scientific. Reports., vol. 12, no. 1, pp. 1–10, 2022

7. **R. Kumar**, V. Kumar[1], C. Rich, D. Limmerhirt, B. Kushwa, B. Fowlkes, A. K. Sahani," Machine Learning Models based on FEM Simulation of Hoop Mode Vibrations to Enable Ultrasonic Cuff-less Measurement of Blood Pressure" (under submission).

8. M.Kumar, V.Kumar, A. Chander, **R. Kumar**, Abhinav Airan, A.K. Sahani, Dr. Rajesh Arya, "Design and Technical Evaluation of an AMBU-BAG Based Low-Cost Ventilator-AARMED", ASME Journal of Medical Devices (under review)

9. M.Kumar, A. Chander, **R.Kumar**, A.K. Sahani, Dr. Rajesh Arya, "AMLEX- A Smart Patient Driven Oxygen Rationing Device", IET Technical Review (under review)

Conference papers

1. **R. Kumar** and A. K. Sahani, "A Device to Reduce Vasovagal Syncope in Blood Donors," Annu. Int. Conf. IEEE Eng. Med. Biol. Soc. IEEE Eng. Med. Biol. Soc. Annu. Int. Conf., vol. 2021, pp. 2136–2139, Nov. 2021, doi: 10.1109/EMBC46164.2021.9630891.

2. M. Kumar, **R. Kumar,** V. Kumar, A. Chander, V. Gupta, and A. K. Sahani, "A Low-cost Ambu-bag Based Ventilator for Covid-19 Pandemic," 2021 IEEE Biomed. Circuits Syst. Conf., pp. 1–5, Oct. 2021, doi: 10.1109/BIOCAS49922.2021.9644985.

3. A. N. Mallick, M. Kumar, A. Chander, **R. Kumar**, K. Arora, and A. K. Sahani, "Automatic Pasteurized Formula Milk Preparation Machine with Automatic Sterilized Containers," Annu. Int. Conf. IEEE Eng. Med. Biol. Soc. IEEE Eng. Med. Biol. Soc. Annu. Int. Conf., vol. 2022, pp. 2663–2667, Jul. 2022.

4. **R. Kumar,** A.Adatia, and A. K. Sahani, "Hypertension Prediction by using Machine Learning Algorithm based on Physiological Parameters," Annu. 3rd Int. Comsys, 2022.

Book Chapters

1. **R. Kumar**, H.Singh, and A. K. Sahani, P.Sarkar, "3D printing with biomaterials a prospective view for biomedical applications" Innovative Processes and Materials in Additive Manufacturing, Elsevier 2022.

2. A Mukherjee, S Sarker, **R Kumar**, A Sahani, B Das, "Optimization of bio-ink using machine learning", Artificial Intelligence in Tissue and Organ Regeneration, Elsevier 2023.

Patents

1. A. K. Sahani, **R. Kumar**, G. S. Wander, "Mercury-free Sphygmomanometer", Indian Patent, (Published).

Table of Contents

LIST OF FIGURES

LIST OF TABLES

NOTATIONS AND ABBREVIATIONS

CHD	Coronary heart disease
BP	Blood Pressure
PPG	Photoplethysmography
ECG	Electrocardiogram
BCG	Ballistocardiograph
PTT	Pulse transit time
PAT	Pulse arrival time
PWA	Pulse wave velocity
PVD	Physical vapor deposition
CVD	Chemical vapor deposition
PEE	Personal protective equipment
PMMA	Polymethylmethacrylate
3DP	3D Printing
SLA	Stereolithography apparatus
SLS	Selective laser sintering
STL	Stereolithography
P_{ma}	Mean arterial pressure
P_s	Systolic pressure
P_d	Diastolic pressure
PPM	Parts per million
eV	Electron volt
PLA	Polylactic acid
CAD	Computer aided design
MS	Merkfree sphygmomanometer
WHO	World health organization
FEM	Finite element method
ARFI	Acoustic radiation force impulse
HMF	Hoop mode frequency
ILD	Inner lumen diameter
TD	Tube diameter
TT	Tube thickness
ML	Machine learning
DNN	Deep neural network
OCR	Optical character recognition
FFT	Fast Fourier transform
PCB	Printed circuit board
OLED	Organic light emitting diode

Chapter-1: Introduction

1.1 Hypertension and its relation to cardiovascular disease (CVD), and Global disease burden.

More than a quarter of the world's population suffers from hypertension [1], [2]. It is the most important modifiable risk factor for multiple cardiovascular and renal complications as shown in Figure.1.1 [3] and is the single most important risk factor for death [4]. Globally, approximately 54% of strokes and 47% of coronary heart diseases (CHD) are accountable to high BP [5]. There are 57% of stroke deaths and 24% of CHD deaths in India directly attributable to hypertension [6]. The Lancet Commission on hypertension has identified an overall improvement in the quality of blood pressure (BP) measurements as the preliminary step towards addressing the worldwide burden of high BP [7]. As per the report issued by the National Health Service of UK, they have spent 2.1 bn Euro every year on diseases caused by high blood pressure [8] (Figure.1.2).
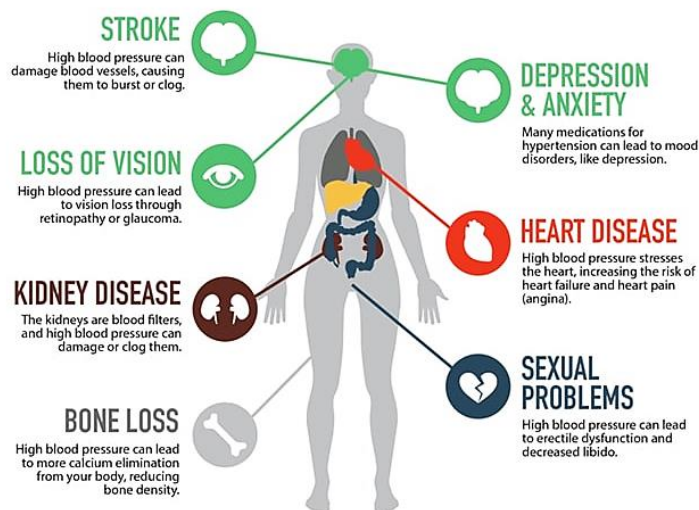
Figure 1.1 Effects of hypertension on human health [2].
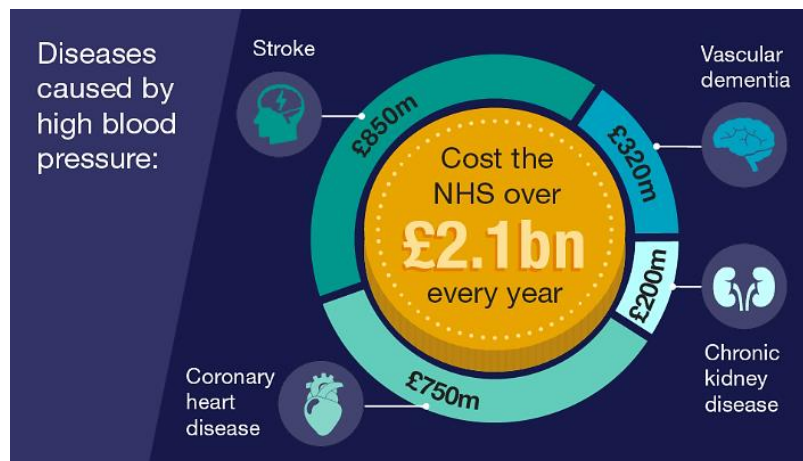
Figure 1.2 Pie chart of spent analysis on diseases caused by high blood pressure born by the UK government every year [7].

1.2 Blood pressure Basics

Blood is pumped from the heart through the arteries to the body's periphery and returned through the veins. As the heart pumps, the blood pressure in arteries cycles between a maximum, known as systolic blood pressure, and a minimum, known as diastolic blood pressure. Typically, a healthy person has a systolic pressure of 120 mmHg and a diastolic pressure of 80 mmHg (1 mmHg is equivalent to approximately 133.3 Pa). Figure.1.3 shows how the fluctuation of pressure in the arteries takes a characteristic shape. Pulse pressure is the difference between systolic and diastolic pressures. An average of the curves in the figure can be used to calculate the mean arterial pressure.

$$P_{ma} = \frac{1}{3}P_s + \frac{2}{3}P_d$$

In an approximate back-of-the-envelope calculation, P_{ma} represents the mean arterial pressure, P_s represents systolic pressure, and P_d represents diastolic pressure. The blood pressure in the aorta is referred to as the central blood pressure. It has been shown that central blood pressure is more closely related to intermediate cardiovascular risks than brachial artery blood pressure [9].

1.3   Importance of accurate blood pressure measurement.

The accurate measurement of BP is correlated to better hypertension management and a decrease in cardiovascular morbidity and mortality [10]. Overestimates of BP are associated with issues like psychological effects of misdiagnosis, side effects of antihypertensive medications, higher treatment costs and increased insurance. Having said that, the aftermath of underestimates of BP could not only deprive patients of therapy but could also potentially increase the current levels of fatal strokes and myocardial infarctions.

1.4 Evolution of blood pressure measurement methods.

The Ayurvedic system of Nadi Pariksha has thousands of years of experience with strong literature support, but is subjective in nature, and it is vital to study Nadi with a scientific approach. As per classical texts, qualities, or properties of pulse such as pulse movement (gati), speed of the pulse (vega), stability of the pulse (sthiratva) and hardness of the artery (kathinya) play major role in Nadi Pariksha and these properties were analyzed and compared with the modern pulse parameters namely pulse wave velocity, pulse rate variability and arterial stiffness. The speed, stability, and gati of the pulse differ with aggravated doshas, and assessing those variations with Nadi Pariksha is a science unto itself. In the traditional ayurvedic practice, pulse-based diagnosis was used to diagnose diseases effectively by touching the radial artery with fingers. It is quite evident from the texts that gati plays a significant role in assessing the dosha predominance and traditional ayurveda doctors were adept in assessing gati from nadi [11]. Galen (130-200 AD) classified pulse strength, rate, and rhythm by palpation, but it wasn't until 1733 when Stephen Hales measured arterial pressure directly in an unanesthetized horse. Nevertheless, it wasn't until 1828 that the mercury U-tube manometer was developed by Poiseuille that we were able to measure blood pressure (mm Hg). In 1864, Fick employed a Bourdon tube and a stylus to inscribe a record on a smoked-drum kymograph in order to accurately measure systolic and diastolic pressures [12].

1.5 Different methods of blood pressure measurement.

There are two most accepted methods of blood pressure invasive and non-invasive, the most known example of invasive based is arterial catheter, and non-invasive blood pressure measurement method are subdivided into cuff and cuffless based.

1.5.1 Arterial Catheter

Invasive arterial catheters are inserted most commonly near the wrist to measure blood pressure directly [13]. A catheter can be inserted into most patients; however, it cannot be inserted into patients with Raynaud's phenomenon, thromboangiitis obliterans, infection at the insertion site, or traumatic injuries at the insertion site [14]. Invasive procedures carry risks, including a (0.09) percent chance of permanent ischaemic damage, a (19.8%) chance of temporary occlusion, an infection (0.3%), a pseudoaneurysm (0.9%), haematoma (14.4%), and bleeding (0.53%) [13]. Other risks include abscess, cellulitis, median nerve paralysis, suppurative thrombarteritis, air embolism, compartment syndrome, and carpal tunnel syndrome. However, its invasive nature makes it impractical outside of hospitals, despite the low-risk percentages. Further, when a catheter is used in the radial artery, it can only measure peripheral blood pressure, which is different from central blood pressure in the aorta.

1.5.2 Cuff based methods

In the cuff-based BP measurement, a cuff is wrapped around the upper arm and takes about 10 minutes to measure systolic and diastolic measurement points. In cuffless as name suggests without cuff, it is a point of time continuous BP measurement method. Three most widely accepted cuff-based devices for the measurement of BP are the mercury sphygmomanometer, the aneroid sphygmomanometer, and the oscillometric digital BP monitor.

Location of blood pressure

The brachial artery is the standard location for measuring blood pressure. A growing number of wrist and finger pressure monitors are available, but it is important to keep in mind that the systolic and diastolic pressures vary significantly along the arterial tree, with the systolic pressure increasing as you get further away from the heart, and the diastolic pressure decreasing.

The auscultatory method

Mercury sphygmomanometers are considered as the gold standard in BP measurement. They are based on Bernoulli's principle and the auscultatory method. The pressure gauge indicator itself is basically a column of mercury. The pressure indicated is simply a function of density and height of the mercury column. Density being a physical property of mercury ensures that the readings are reliable even under low maintenance conditions. Korotkoff sounds have well-established markers for identifying systolic and diastolic BP points and all clinicians are trained to identify them [15]. New devices known as "hybrid" sphygmomanometers have been developed as replacements for mercury devices. Essentially, these devices combine the features of both electronic and auscultatory devices by replacing the mercury column with an electronic pressure gauge, like oscillometric

devices. However, blood pressure is taken by an observer using a stethoscope and listening for Korotkoff sounds, just as with mercury or aneroid devices [16].

The aneroid method

The aneroid type of sphygmomanometer uses mechanical springs and dashpot systems. These use the same auscultatory method of measurement as that of mercury sphygmomanometer. It is made worse by the fact that aneroid manometers, which use this technique, are less accurate and often require frequent calibration [17].

The oscillometric method

The digital BP monitors are the most popular as home use self-monitoring devices. They use the oscillometric method of BP measurement which measures the mean pressure accurately, but Systolic and diastolic pressures are derived based on different empirical methods which varies from company to company and mostly maintained as trade secrets [18], [19].
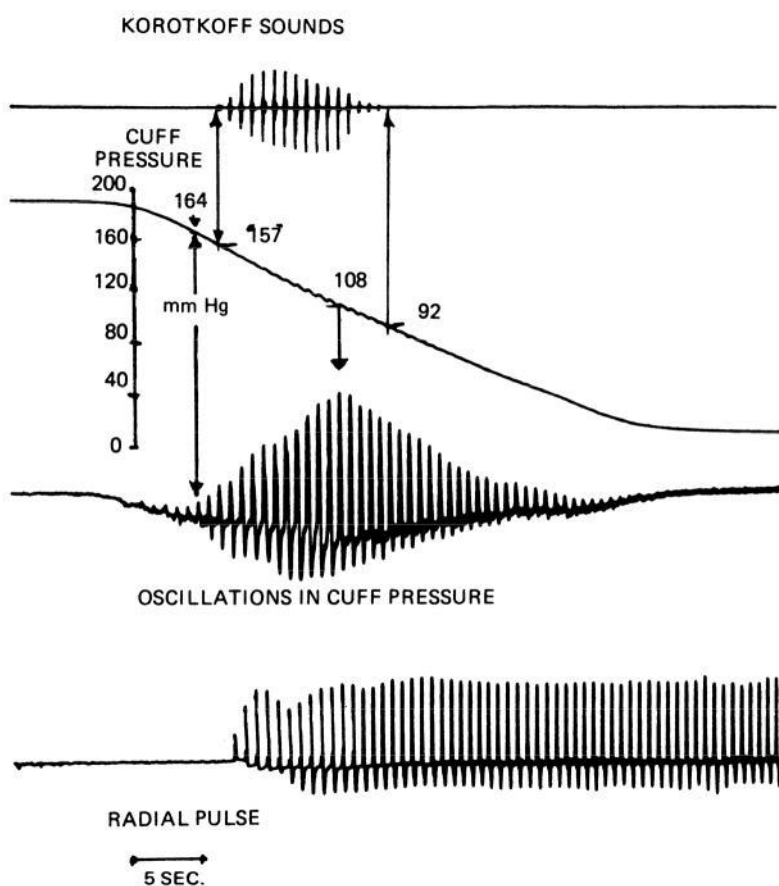
Figure1.3. During deflation, changes occur distal to the sphygmomanometer cuff. The upper trace represents Korotkoff sounds. The second trace shows the pressure in the cuff. The third trace shows oscillations in the cuff pressure. The maximal oscillation occurs at a mean arterial pressure of 108 mm Hg. The bottom trace shows the radial pulse (permission taken from [20])

1.5.3 Cuffless based methods

Cuffless blood pressure monitoring technologies are based on directly measuring physiological parameters without occluding the artery.

Tonometry

Tonometry, also called applanation tonometry, is a technique designed for taking blood pressure at the wrist. The method involves placing a pressure transducer next to an artery supported by a bone and assuming that the transducer readings relate to blood pressure within the artery [21]. Tonometric measurement means 'measure a pressure', whereas applanation means 'flatten' [22] . The central blood pressure can be estimated using tonometry by using system models (e.g. transfer functions) [23]. Tonometry has the advantage of capturing the entire pressure waveform; however, it does require calibration with an external device, such as a cuff. It is also important to place the device correctly in tonometry [24].

Photoplethysmography method

A plethysmograph is an instrument used to estimate an organ's volume or volume change. A pulse oximeter is normally used in photoplethysmography (PPG) to measure the artery's volume. When blood pulses through the finger, light is reflected and transmitted differently. As a result of pulse oximetry, light transmission or reflection is measured, which is related to blood volume in an artery. In a PPG graph, the amplitude of the signal is plotted against the time. There are many ways to estimate absolute blood pressure using PPG, both with and without calibration; the literature does not seem to be primarily focused on estimating relative blood pressure changes using PPG. A description of each PPG-based technique and its calibration details is given in the following subsections.

Pulse transit time

Pulse transit time has been linked to blood pressure inside arteries. Pulse wave velocity, V, for elastic arteries is defined as follows [25]:

$$V = \sqrt{\frac{Et}{2R\rho}} \qquad\qquad (1.2)$$

Where E is the elastic modulus of the artery, t is the artery thickness, R is the inner artery radius, and ρ is the density of the blood.

There are numerous physiological parameters, but only a few are helpful for the BP measurement. There are two main variables used to measure BP: the estimation of time required for a pressure wave to travel between two points and the amplitude of the arterial waveform. After measuring one or more of these variables, cuffless BP devices use several approaches to estimate BP. The most common approaches include pulse transit time (PTT), pulse arrival time (PAT), pulse wave analysis (PWA), and tonometry [26]. PTT is the time required for the arterial pressure wave to travel from the proximal to the distal site. PTT is contrary to blood pressure and is dependent on the arterial radius, arterial compliance, blood density, and arterial wall thickness [27]. PWV relates to BP by applying the Moens-Kortewegz [28] and Huges [29] equations.

The general equation of PWV is defines as follows:

$$PWV = \frac{L}{PTT} \qquad (1.3)$$

Some of the cuffless technologies use these approaches or a combination of them to estimate, such as photoplethysmography (PPG), electrocardiogram (ECG), mobile phone sensors [30] microelectromechanical [31], magneto-plethysmography [32] , ballistocardiography (BCG) [33], bioimpedance [34], ultrasound image processing [35].

Finger Cuff

In another PPG-based blood pressure measurement technique, a finger cuff is used to record the PPG signal. This method is also known as vascular unloading. In order to maintain a constant blood volume in the finger, the cuff automatically inflates or deflates as the PPG is recorded. Keeping blood volume constant requires a constant blood pressure within the vessel [21], [36]. In 1973, Penaz introduced a finger cuff device called Finapres that used this method [37]. This method has been shown to provide accurate estimates of pressure changes; however, one author suggests that it is not clinically used due to its cost, inconvenience, and high degree of variability when measuring absolute pressures [38].

Other Techniques

Researchers are developing other methods for estimating arterial blood pressure non-invasively through ultrasound contrast agents in the bloodstream [39]–[41]. Blood pressure can be estimated by examining cavitation frequency, radial oscillations, and general microbubble behaviour [39]. Injection of microbubbles might not be optimal in every instance based on some reports [39], and accuracy has been reported to be low with some variations of this method. A method similar to ours uses ultrasound and image processing methods to measure noninvasively central venous pressure [42]. Ultrasound is typically used for non-invasive imaging of tissues. In normal imaging mode operations, plane and focused waves of a few microseconds pulse duration are used. Ultrasound in its imaging modality has been used with limited success to measure BP. For instance, Beulen et. al. developed an innovative approach to measuring internal pressure by monitoring the changes in the ratio of flow and cross-sectional area using ultrasound probes but requires a flow sensor to be directly inserted into the system [43]. Zakrzewski et. al. have used ultrasound imaging to monitor internal pressure by recording changes in the diameter of the tube under the application of external force from the ultrasound probe [44]. However, this method requires the continuous application of external loading, which may be uncomfortable and may dislodge plaque in atherosclerotic arteries. Weber et. al. proposed a system for measurement of blood pressure at the wrist using a balloon inflation system pushing against the radial artery that works like a cuff [45]. A single element ultrasound probe is aimed at the artery that measures the diameter change of the radial artery and identifies when it is completely blocked by pressure from the inflating balloon. The system is quite bulky and cumbersome for regular use. Apart from that, radial arterial pressure is not used in most clinical measurements. The summary of all measurement methods of BP is shown in Table.1.1

1.6 Advantages/limitations of different BP measurement techniques.

Mercury sphygmomanometer has been considered as the gold standard of BP measurement for more than 100 years. Its advantages are its accuracy, minimal calibration requirement and infrequent breakdown. In comparison, the aneroid type of sphygmomanometer uses mechanical springs and dashpot systems. These use the same auscultatory method of measurement as that of mercury sphygmomanometer but are prone to run out of calibration within six months to a year due to loosening of springs, especially in heavy use environments of hospitals [17], [46], [47]. Once spring becomes loose, these are nearly impossible to recalibrate. The digital BP monitors are the most popular as home use self-monitoring devices. The advantage of these devices is that white coat hypertension is not associated with them, self-monitoring devices, no rounding off errors, and portable. Automatic BP monitors are considered to be of the lowest accuracy among the three methods.

Over the last 10 years or so a lot of interest has come in cuffless blood pressure monitoring devices. The advantage of these devices is that they do the point in time measurement of blood pressure without occluding the arteries. The disadvantage of these devices is that they have low accuracy with respect to gold standard BP measurements performed with mercury type.

1.7 Toxic effects of mercury and Minamata convention.

Unfortunately, mercury is found to be detrimental to human and environmental health. Exposure to mercury – even in small amounts – may cause serious health problems. There were past episodes like kodaikanal in Tamil Nadu, Minamata Tragedy in Japan which showed Mercury toxic effect on the environment as well as on humans [48], [49]. To limit the use of mercury, in year 2013, governments across the world agreed to the Minamata Convention on Mercury to limit production, export and use of mercury [50]. Minamata convention is aimed to protect human health and environment from anthropogenic emissions and releases of mercury and mercury compounds. The major focus of the treaty is to control and regulate mercury supply and trade along with ban on manufacturing of mercury containing products. As discussed earlier, the aneroid and oscillometric types are still inadequate compared to the accuracy or reliability of the mercury sphygmomanometer [51]. Mercury devices are being banned not because of the invention of any new technology of BP measurement but because of the harmful effects of mercury.

1.8 Regulations and guidelines of various governments worldwide and Indian prospective towards Mercury Sphygmomanometer.

Around 128 countries are signatories to the Minamata convention as per the 2014 reports [52]. Following its commitment at the Minamata Convention, the Indian government has taken steps towards elimination of mercury sphygmomanometers from the Indian healthcare systems. Advisory has been issued as far back as 2010 to avoid usage and procurement of the mercury sphygmomanometer [19] and India is required to ban mercury sphygmomanometer by end of year 2020 [53]. However, mercury sphygmomanometers are still widely used in India. The recent India Heart Study conducted by Kaul et al. [54] indicates that nearly 69.3% of clinicians in India still use the mercury sphygmomanometer in their practice. We hypothesized that there is an unmet need for a more reliable replacement of Mercury sphygmomanometer which is not being fulfilled by aneroid and oscillometric types and is the cause behind resilience of clinicians to still stick to the mercury sphygmomanometer.

1.9 Clinical need

To measure blood pressure, doctors use three non-ideal techniques: an invasive arterial catheter, an oscillometric blood pressure cuff, or an auscultatory cuff. Although catheters provide continuous and accurate data but inserting them is an invasive procedure. As oscillometric cuffs occlude arteries, they cannot provide continuous pressure measurements and have been shown to significantly underestimate mean arterial pressure in patients with atherosclerosis [21]. To validate our hypothesis, we have conducted an anonymous survey among Indian clinicians across all specialities. We found that the majority of clinicians are in favour of the mercury sphygmomanometer in terms of accuracy. Moreover, if an alternative to a mercury sphygmomanometer is given to them with the same principle and accuracy, they will buy it and use it.

1.10 Aims and objectives.

The motivation of the presented work is derived from the necessity to provide an effective, efficient, and accurate blood pressure monitoring technology. Due to changed government policy of phasing out mercury-based sphygmomanometers and preference of clinicians for a reliable auscultatory pressure monitor there is an open and unmet need for reliable and accurate replacement of mercury sphygmomanometer. There were past episodes like Kodaikanal in Tamil Nadu, Minamata Tragedy in Japan which showed Mercury's toxic effect on the environment as well as on humans prompted us to explore new avenues in the direction of cuff based and cuffless BP monitoring technologies.

The main objective of the present research work is to develop alternatives to the mercury sphygmomanometer that are comparable in terms of accuracy, and robustness. The research objectives of the thesis are summarized as follows.

1. First, to understand the need of an alternative devices among Indian clinicians, we conducted an online survey among Indian clinicians irrespective of their specialties. The answers show that there is a large market for such a device in India and worldwide, owing to phasing out of mercury and clinician preference of a reliable auscultatory pressure monitor.

2. We aim to develop a Merkfree device which aims at being very close to the mercury sphygmomanometer while getting rid of the mercury. The innovation is in the use of Galinstan and the specially designed tubing and enclosure to hold it. Although there are Galinstan based thermometers available in the market, there has been no attempt to develop a Galinstan based sphygmomanometer.

 3. We aim to explore a novel method to measure BP through ultrasound. In this method, the arterial wall would be pushed with an acoustic radiation push impulse (ARFI). After the completion of the ARFI pulse the artery undergoes impulsive unloading which stimulates a hoop mode vibration. We designed a machine learning model which makes it possible to estimate the internal pressure of the artery using ultrasonically measurable parameters.

4. We aim to develop Auscl-D, which displays BP reading digitally, like oscillometric devices, but measurements are performed using auscultation method employing traditional stethoscope and manual pumping system as in an aneroid device.

1.11   Structure of the thesis

The thesis comprises nine chapters as briefly discussed below.

- Chapter 1: This chapter includes the introduction of the thesis work. It defines the background of the problem associated with blood pressure monitoring technologies and including a literature survey, motivation, objectives, and thesis outline.

- Chapter 2: This chapter underlines about a survey to gauge confidence of Indian clinicians on three primary devices for blood pressure measurement.

- Chapter 3: This chapter explains about the replacement of mercury in sphygmomanometer with galinstan and its properties, challenges, and issues.

- Chapter 4: This chapter explains about the paradigm of Merkfree. It also explains about the aesthetics and additive manufacturing technology used in the manufacture of the Merkfree.

- Chapter 5: This chapter demonstrates about the clinical trial results of Merkfree device on 260 subjects at DMC&H Ludhiana.

- Chapter 6: This chapter underlines about exploration of new AI driven methods of cuff less blood pressure measurement using acoustic radiation force impulse (ARFI).

- Chapter 7: This chapters explains about the design a digital sphygmomanometer named 'Auscl-D' which is based on auscultatory method and its clinical trial results.

- Chapter 8: This chapter explains about the other different notable work in medical devices and its application of use.

- Chapter 9: The chapter concludes the findings of the thesis work. It summarizes the work presented in each of the chapters and also provides the future direction of the present thesis work.

1.12 Main intellectual contributions of the thesis and its impact on the field.

1) Development of Merkfree: The dissertation work developed a cuff-based blood pressure monitoring device called Merkfree as a replacement for the traditional mercury sphygmomanometer. The device uses Galinstan, a non-toxic alloy of Gallium, Indium, and Tin, as a substitute for mercury. Clinical trials validated the accuracy of Merkfree, and it was found to be a viable alternative to the mercury sphygmomanometer.

2) Development of Auscl-D: Another cuff-based device called Auscl-D, a handheld and compact digital version of BP measurement based on the auscultation method of measurement, was also developed.

3) Cuffless BP Measurement: The dissertation work explored the development of a cuffless measurement of blood pressure using ultrasound. Two machine learning models were designed to estimate the internal pressure of the artery using ultrasonically measurable parameters. Extensive simulations and experimental validation on arterial phantoms were done to verify the accuracy of these models.

4) Impact on the Field: The development of Merkfree and Auscl-D provides clinicians with a viable alternative to the mercury sphygmomanometer for accurate blood pressure measurement. The exploration of cuffless blood pressure measurement using ultrasound and machine learning models opens up the possibility of continuous, real-time, and non-invasive blood pressure measurement, which can have significant implications in hypertension management and reducing cardiovascular morbidity and mortality.

Table1.1 Summary of all BP measurement methods

Cuff based methods

Method	Description	Advantages	Disadvantages
Auscultatory method (Hybrid method)	Based on the method of auscultation where the doctor listens to Korotkoff sounds [21].	- Comparable to gold standard mercury sphygmomanometer [55].	• Rounding of error [21]. • Inter-observer error [55]. • White coat hypertension [56]. • Errors occur due to improper rate of deflation [57][58]. • Optimal cuff size and placement required [55].
Proposed method (Merkfree)	A doctor listens to Korotkoff sounds	- Accuracy compared with the mercury sphygmomanometer. - No calibration is needed - Minimal rounding of errors	• A small meniscus of NaOH is maintained. • White coat hypertension • Errors occur due to improper rate of deflation
Oscillometric method	Based on oscillometric method of BP measurement which measures mean pressure accurately, but systolic and diastolic pressures are derived based on different empirical formulas [59].	- Less susceptible to external noise [21] - No rounding of errors [60] - Portable and easy to use [61]. - No transducer needed [21].	• Low accuracy among three cuff-based methods [61]. • Most algorithms are proprietary [21] • Many devices have not been validated with published standards [61] • Readings are varying from devices to devices [21], [61].
Proposed method (Auscl-D)	Based on the method of auscultation.	- Portable - No rounding of errors - Accuracy comparable to mercury sphygmomanometer. - OLED display	• Timely calibration is required. • Errors occur due to improper rate of inflation and deflation. • Timely replacement of lipo battery. • Optimal cuff size and placement required.

Cuffless based methods

Method	Description	Advantages	Disadvantages
Microbubbles	Response under ultrasound [39]	- Non-invasive [62] - Potentially use for all chambers of heart [62]	• Requires ultrasound [62] • Requires an injection of microbubbles into blood stream [62]. • Low reliability and resolution [39].
Tonometry	Gauge measures force variation on skin surface [63]	- It better estimates central arterial pressure when used at radial artery than finger cuffs [64] - Less sensitive than finger cuffs to vasoconstriction and vascular disease [64].	• Requires calibration for each patient [21]. • Not applicable for routine clinical use [21]. • Position and handling specific [21], [64]. • Not reliable on elderly and large change in blood pressure [64].
Ultrasound	Use ultrasound image modality [43]	- Non-invasive [43] - Real time monitoring [43]	• Requires flow sensor invasively [43]. • Continuous external loading may cause dislodge plague in atherosclerotic arteries [44]. • Using balloon inflation system pushing against the radial artery [45].
Proposed method	Acoustic radiation force impulse is used to push the wall of the artery.	- Non-invasive - An empirically derived machine learning (ML) model to measure blood pressure using ARFI. - Real-time BP monitoring - Accuracy is within the clinical limits.	• Frequency down shift owing to damping. • Accuracy of hoop mode frequency reduces in damping medium.

Chapter-2: A survey to gauge confidence of Indian clinicians on three primary devices for blood pressure measurement

2.1 Purpose: As per its commitment at Minamata convention, and in line with other developed economies, the Indian government is set to ban the use of mercury sphygmomanometers by end of the year 2020. However, the Mercury sphygmomanometer is still widely used by clinicians in India. We conducted a survey to gauge the confidence of Indian clinicians on three primary devices of blood pressure (BP) measurement – mercury sphygmomanometer, aneroid sphygmomanometer and automatic digital BP monitor.

2.2 Materials and methods

To validate our hypothesis, we conducted an online survey among multiple clinician groups in India. We asked the following four questions.

(1) What is your clinical specialization?

(2) Which of these is the most accurate BP measuring device? (Only one option to be chosen)

 (a) Mercury sphygmomanometer

 (b) Aneroid sphygmomanometer

 (c) Digital automatic BP monitor

(3) Which type of manometer in your experience is most robust with least breakdown and calibration requirement? (only one option to be chosen)

 (a) Mercury sphygmomanometer

 (b) Aneroid sphygmomanometer

 (c) Automatic digital BP monitor

(4) If you are given an alternative to mercury manometer with same principle of operation and same accuracy (but mercury-free), will you buy it? (only one option to be chosen)

 (a) Yes

 (b) No

(c) May be

(5) Which is important to you in a BP monitoring device? (multiple options may be chosen)

(a) Portability

(b) Accuracy

(c) Convenience of use.

The survey was kept anonymous to avoid desirability bias [65]. The data were collected using Google forms that were sent to hundreds of clinicians across India through email and closed-messaging groups. We received 139 responses across specialties. The responders were not associated with any single program or any single center. The distribution of the specializations of the participating clinicians is shown in Table.2.1.

Table.2.1 Broad categorization of clinicians who participated in the survey

Clinicians filed of specialization	Number of clinicians participated
Graduate (MBBS)	3
Medicine and allied branch specialists (MD)	59
Super specialists	32
Other specialists MD's from non-medical specialists (basics, surgical, etc.)	45
Medicine and allied branch specialists (MD): anesthetist and intensivist, chest and TB, general physician and medicine. Super specialists: cardiology, clinical immunology and rheumatology, endocrinology, gastroenterology, nephrology, neurology, oncology and urology. Other specialists MD's from non-medical specialists (basics, surgical, etc.): ENT, Health Management, Microbiology, MS (Surgery), Obstetrics and Gynaecology, Ophthalmology, Orthopedics, Pathology, Pediatrics, Pharmacology, Psychiatrist and Radiology.	

2.3 Results

A summary of responses to the questions is shown in Figure.2.1. From Figure. 2.1(a), we can see that more than 80% of clinicians consider the mercury sphygmomanometer as the most accurate BP measuring device. Mercury sphygmomanometer is also the preferred choice of nearly half of the clinicians in terms of its reliability and minimal calibration requirement compared to the other two (Figure.2.1(b)). Aneroid comes second in both accuracy and reliability perception while automatic digital oscillometric device fares poorly on both, with only 6% clinicians grading it as most accurate and 14% as most reliable. Mercury sphygmomanometer is the preferred choice on both accuracy and reliability parameters by most clinicians. Also, 88% of respondents are willing to buy a mercury-free sphygmomanometer with the same principle of operation and the same accuracy as that of the mercury type (Figure.2.1(c)). This also indicates that the current resilience to stick to mercury type is because of the perceived superiority of the mercury type over others. From the perspective of the overall accuracy, reliability, calibration and maintenance, the study brings out an unmet need for a more effective alternative to mercury sphygmomanometer which is not currently being fulfilled by the aneroid and the oscillometric types. If such a device is offered, there will be a quick market acceptance for it. Answers to the fifth question indicate the perceived desirable characteristics of such a device. Accuracy is the most important parameter for in-clinic BP measuring device. Even if such a device requires more skill for use or less port- able, still it shall be readily accepted by the clinicians especially for in-clinic use. Although the oscillometric devices offer a high degree of portability and convenience of use, they are not a preferred choice with the clinicians due to lower perceived accuracy and reliability. This may be partially due to the lack of validated oscillometric BP measurement devices in India. The lack of uniformity and inconsistent accuracy as compared to the mercury sphygmomanometers is one of the major drivers for this perception. Reliable and validated oscillometric devices should become available in the country. Following that, physician's information, and education regarding the dependability of these devices will help in switching over to these devices in the office. Simply banning mercury devices will not be a solution. Either similar non-mercury devices become available or validated oscillometric devices have to be made available as in the rest of the world.

(a) Which of these is the most accurate BP measuring device?
- Mercury Sphygmomanometer
- Aneroid Sphygmomanometer
- Digital Automatic BP Monitor

(6%, 12%, 82%)

(b) If you are given an alternative to mercury manometer with same principle of operation and same accuracy (but mercury free), will you buy it?
- Yes
- No
- Maybe

(9%, 3%, 88%)

(c) Which type of manometer in your experience is most robust with least breakdown and calibration requirement?
- Mercury BP Monitor
- Aneroid BP Monitor
- Automatic BP Monitor

(14%, 49%, 37%)

(d) Which is important to you in a BP monitoring device?

CONVENIENCE OF USE	37(27%)
ACCURACY	128(93.5%)
PORTABILITY	25(18.2%)

Summary of all 139 responses to the last four questions.

Figure.2.1 A summary of responses to the questions

2.4 Conclusion

Mercury sphygmomanometers are already banned in many countries and are set to be banned in India by end of 2020. The survey conducted by us proves that there is higher perceived accuracy and reliability of the mercury sphygmomanometer compared to other competing devices in the market. Banning of this device may create an unmet need that is still not fulfilled adequately by the aneroid or oscillometric types. We believe that validated oscillometric devices should be promoted to bring about change in perspectives of Indian clinicians towards adopting non-mercury alternatives of BP measurement.

Chapter-3: Galinstan and its properties, challenges, and issues.

Gallium-based low melting point metals are an exciting new material that could have widespread success in many emerging applications. Their good conductivities, large working temperature range, and fluid properties at room temperature make them appealing to many applications. However, their oxidation behavior must be either mitigated or embraced depending on the application. Here in our case, we require an oxide-free Galinstan surface to maintain its fluidity property up to 1 part per million (ppm), or 0.0001%, of oxygen. Gallium which is a key component in Galinstan would show a more viscous behaviour that is caused by the thin oxide layer. Generally, gallium forms two oxide phases that are mentioned in the equations (1) and (2). The most stable state of the Gallium oxide when it interacts with atmospheric oxygen is mentioned in equation

$4Ga\ (s) + 3O_2\ (g) \rightarrow 2Ga_2\ O_3\ (s)$ ……………………… (1)

$4Ga + O_2\ (g) \rightarrow Ga_2\ O$…………………………………. (2)
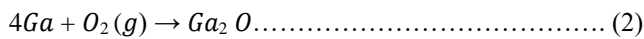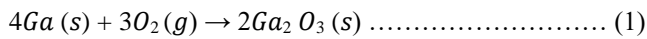
In an ambient environment, a droplet of Galinstan is oxidized instantaneously and adheres to the surface it is being dispensed on.

3.1 Various solutions to overcome wettability.

The problem of forming oxide by gallium is very severe and would impact the flow of Galinstan. Various methods have been proposed in literature to negate this issue. Following are the categories of methods to make Galinstan non-sticky to glass as per the available literature:

1. Surface modification methods for the substrate (glass) where the Galinstan is always in close contact.
2. Chemical treatment and surface modification on the Galinstan surface to remove or protect the thin oxide layer.
3. By varying the doping concentration of gallium and incorporation of other metals into Galinstan.

3.1.1 Surface modification techniques.

i) *Superhydrophobic coatings*

Superhydrophobic coatings repel water and, in some cases, other liquids as well. The non-adhesiveness is actuated by topographically elements at the nano-/micro scale and low surface energy. There are various applications which use superhydrophobic coatings such as biomedical, marine, auto- motive and energy sectors etc. Only a few superhydrophobic coatings are suitable for the biomedical applications because of the synthesis compounds' toxic behaviour [66].

(ii) *Molecular beam epitaxy*

It has been found in the literature that thin film of gallium oxide coated on a substrate show non-wettability with gallium containing alloys. Kazuo Aok and his group have done an experiment where they have successfully grown a thin transparent, colourless, and mirrorlike film of *β*-Ga2O3 on to *β*-Ga2O3 substrate using molecular beam epitaxy [67] .

(iii) *Atomic layer deposition*

Another method to deposit gallium oxide can be atomic layer deposition technique that is based on the successive use of a gas-phase chemical process. It is a type of chemical vapor deposition. Richard et. al.

successfully developed a thin layer of Gallium oxide on Si (100) substrate. This process yielded second-highest growth rates (1.5 A^0 per cycle) gallium oxide thin film at a low temperature range (60-160 ^{0}C). The deposited layers were homogenous, amorphous, nearly stoichiometric, and free of any major (carbon and nitrogen) impurities [68].

(iv) Physical Vapour deposition

PVD is a deposition method that involves vaporizing atoms of a material from either solid or liquid phase into a vapor phase, under the conditions of high vacuum or low vacuum gaseous atmosphere. This technique is employed to deposit thin films for various applications, such as optical, chemical, mechanical, and electronic applications. The thickness of the deposited thin films usually ranges from 10-100 μm. There are several types of PVD processes available, which are as follows: [69]

    a) Sputter deposition

The deposition of thin films onto a substrate can be achieved through a process known as sputtering. This process involves the generation of plasma and the subsequent forceful collision of ions onto the source material, causing erosion of the material in the form of individual atoms or molecules. Sputtering is categorized into two types: high-pressure and low-pressure sputter deposition.The process schematic is shown in Figure.3.1 (c)

    b) Vacuum evaporation:
Vacuum evaporation is a process in which the gas molecules present between the source and substrate are heated until they undergo thermal evaporation without colliding with each other. This results in the deposition of thin films onto the substrate. The process schematic is shown in Figure 3.1 (a)

c) Arc vapour deposition
Arc vapor deposition is a deposition technique that involves the use of a high-current electric arc and a low-voltage arc to erode the cathode electrode. The arc is moved to melt the anode electrode, and the resulting plasma is then used to deposit a thin film onto the substrate. The process schematic is shown in fig 3(d)

d) Ion plating
Ion plating is a deposition method that involves bombarding atomic-sized particles to deposit a thin film and alter the properties of the deposited film. In this technique, either arc vaporization or vacuum evaporation is used as a source for depositing the thin film onto the substrate. The process schematic is shown in Figure 3.1 (e)
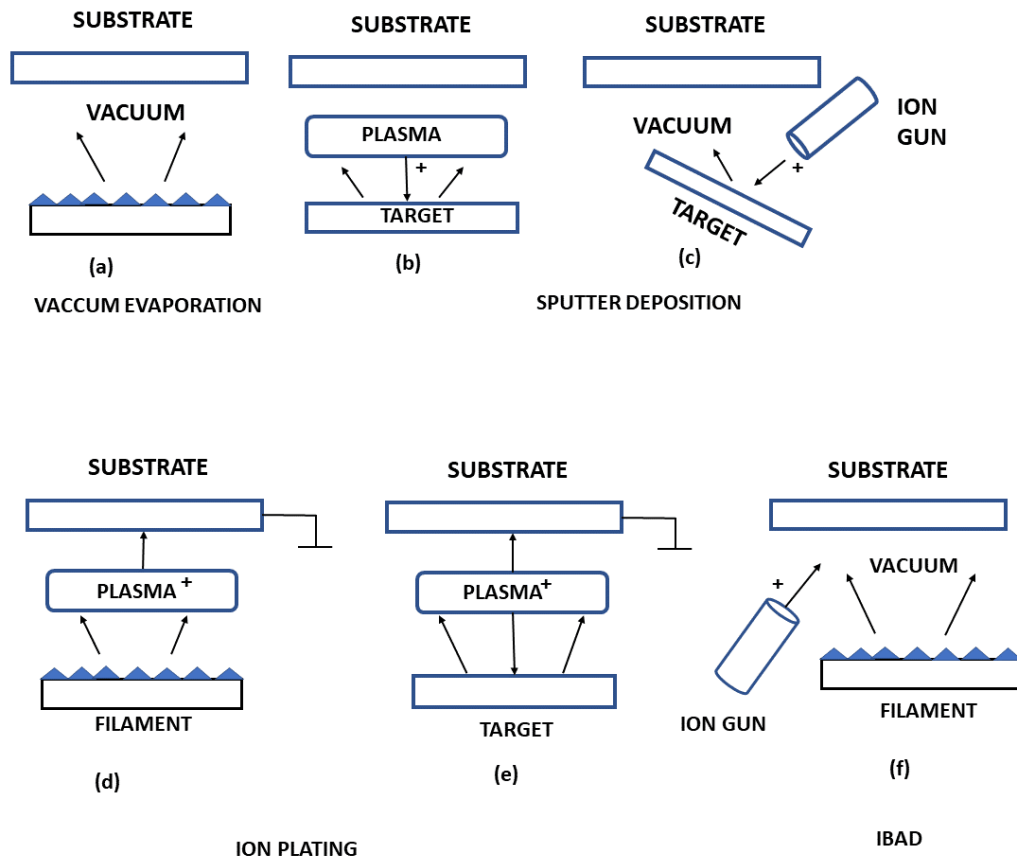
Figure. 3.1. (a) Vacuum evaporation (b,c) Sputter deposition (d,e) Ion plating (f)IBAD

(v) Chemical vapour deposition

Chemical vapor deposition (CVD) is a versatile process suitable for the manufacturing of coatings, powders, fibers, and monolithic components. With CVD, it is possible to produce most metals, many non-metallic elements such as carbon and silicon as well as a large number of compounds including carbides, nitrides, oxides, intermetallic, and many others. This technology is now an essential tool in the manufacturing of semiconductors and other electronic components, in the coating of tools, bearings, and other wear resistant parts and in many optical, optoelectronic and corrosion applications. In CVD, a solid on a heated surface from a chemical reaction in the vapor phase. It belongs to the class of vapor-transfer processes which are atomistic in nature, that is the deposition species are either atoms or molecules or a combination of these.

Advantages of the CVD process:

1. CVD or Chemical Vapor Deposition is a deposition process that offers advantages over other PVD processes like sputtering and evaporation. One such advantage is that CVD is not limited to line-of-sight deposition, which means it has high throwing power. This feature enables it to coat deep recesses, holes, and other difficult three-dimensional configurations with ease. For example, CVD tungsten can be used to completely fill integrated circuits via holes with an aspect ratio of 10:1.

2. CVD can achieve a high deposition rate, allowing for the production of thick coatings, which can be several centimeters thick in some cases. The process is also generally competitive and, in some cases, more economical than PVD processes.

3. CVD equipment typically does not require ultrahigh vacuum and can be adapted to many process variations. Its flexibility allows for changes in composition during deposition, and the co-deposition of elements or compounds can be achieved easily. This feature enables the production of complex multi-layered coatings with a high degree of control over the composition and properties of each layer.

P.R. Jubu et.al demonstrated that the polycrystalline Ga2O3 can be obtained at low substrate temperature by the vapour-solid (VS) mechanism in CVD. This was achieved by the reduction of gallium (III) oxide powder in a hydrogen environment at high temperature and subsequent deposition of -Ga_2O_3 NSs onto a Si substrate at low temperature ~260 °C [70]. As part of this proposal, we plan to explore PVD process in detail to achieve non-wetting coatings inside cylindrical glass surface.

(vi) Surface micromachining by using laser

Surface micromachining is the process in which a surface has been textured by using laser, texturing of the surface creates a more surface roughness and due to which there is less interaction between surface and matter. Nano and micromachining provide a particularly feasible and highly reproducible means for surface texturing. Laser ablation, utilizing an ultrashort (picosecond or femtosecond) pulsed laser source, can be used for high precision machining in almost any material [71].

3.2 Role of superhydrophobic coatings in biomedical applications.

We have already explored various surface modification methods in our previous section and now in this subsection we have explained more about superhydrophobic coatings in detail, and their application in biomedical field. Here we explored these coatings to address the issue of Galinstan wettability but to achieve a transparent nano coating inside the cylindrical tube having an inner diameter of 2.5 mm was a challenging or touch task.

3.2.1 Introduction

The first superhydrophobic behavior was seen in lotus leaves [72], [73]. later, scientist discovered sub- merged superoleophobicity in ''fish scales and the slipperiness of pitcher plants, shark skin and insect wings, gecko foot, mosquito compound eye, water strider leg, Salvinia leaf, stenocara beetle" [74], [75]. Typically, superhydrophobicity is observed as water acquires a contact angle (CA) more than 150°and a sliding angle (SA) less than 10°. A superhydrophobic surface can be created by using a rough surface on a low surface energy material (CA > 90°) or by manipulation of a rough surface using low surface energy materials [76]. There are a few techniques which are being used to obtain such surfaces such as phase separation [77], sol–gel and chemical processing [78], [79], electrospinning [80], laser or plasma treatment [81]–[83], layer- by-layer deposition, template-based techniques, colloidal self-assembly, physical vapour deposition (PVD) and chemical vapour

deposition (CVD) [84]. Nano architecture is the promising geometries for creating nanoscale roughness on the solid surfaces. This can be done in two ways, either by a top-down approach or bottom-up approach. Nanomaterials exhibit dimensions in the range of 1– 100 nm due to which these nanostructures show unique physical and chemical properties, mainly due to their high surface area to volume ratio [85]. Biofouling is a significant challenge in biomedical devices, and proper rectification must be required in biomedical applications. Biofouling is the continuous deposition and growth of unwanted cells, biomolecules, and microorganisms such as fungi, bacteria, protozoa, algae and invertebrates on the surface. Bacteria is one of the most active microorganisms that shows a frequent biofouling effect in biomedical applications such as biosensors, biomedical implants, and other equipment of microbiology labs or pathology labs. Biofouling caused by bacteria on medical devices like implants of knee and hip, cardiovascular stents, artificial organs, voice, and vascular prosthesis, contact lenses, and catheters poses a high risk of infection. Sometimes the infection rate goes very high which leads to reduce the proper functioning of medical devices and the extra cost imposed on removing and reinserting of implants into the body, similarly, increasing the medical cost on antibiotic treatment [86]. The high rate of biofouling infection causes an increase in the mortality rate [87]. Superhydrophobic materials have played a magnificent role in addressing various problems, including many biological, industrial, and medical devices. The primary vital features of these materials are self- cleaning of windshields and antennas, de-icing of glass surfaces, outdoor textiles, antibacterial and antifouling surfaces for biomedical and marine industries [76]. Superhydrophobic coatings are also used in personal protective equipment (PPE) kits, face shield, face- masks to fight the COVID-19 pandemic [88][89].There are lots of materials available to synthesize superhydrophobic material, some of them are organic-based, and few are inorganic-based. However, for biomedical application, suitable biocompatible material has to be chosen. Synthetically developed most suitable biomaterials are PMMA (polymethylmethacrylate), cellulose acetate, Dacron, polyester-urethanes, PEG (polyethylene glycol), silica- based nanoparticles. Mainly, fluorine and chlorine-based superhydrophobic materials do not exhibit biocompatibility due to their cytotoxicity properties [90]. In this brief review, we focused on the fundamentals of wettability and its applications in the field of medical diagnosis, medical devices, and hospital hygiene management.

3.2.2 Fundamentals of wettability

If the contact angle is above 150°and a roll-off angle less than below 5° it is known as superhydrophobic surface. Whereas sur- face with the contact angle below 90° is known as hydrophilic sur- face. The relationship of contact angle with the states of the surface is shown in Figure. 3.2. The contact angle is usually measured when a drop of water resides on a surface. It performed both statically and dynamically [91]. The contact angle value is fundamentally constrained by the free surface energy of the strong material. The link between the surface tension and the contact angle of the inter- face between liquid, solid and gas can be explained by Young's equation (1).

$$Cos\theta = \frac{\gamma_{sv} - \gamma_{sl}}{\gamma_{LV}} \dots \dots \dots \dots \dots \dots \dots (1)$$

Where θ is the contact angle. γ_{SV} corresponds to surface tension at the solid- vapour interface. Similarly, γ_{SL} is the surface tension at solid liquid interface and γ_{LV} is the surface tensions at liquid– vapour interface. This equation only holds for the plain and refined surfaces. The Wenzel model and Cassie-Baxter model define the behavior of water droplets on rough surfaces. The above- mentioned models were first and foremost proposed in 1936 and 1944, individually. The Wenzel model states that when the droplets of liquid fall on to the rough surface, it fills

the gaps of rough surface as illustrated in Figure. 3.3. Furthermore, such Wenzel states have low contact angle and cannot easily roll-off. The Wenzel state is only stable for homogenous material surfaces. However, the modified Young's equation by Wenzel as follows;

$$Cos\theta_r = rCos\theta \dots \dots \dots \dots \dots \dots \dots \dots \dots (2)$$

Where θ corresponds to Young's angle, r corresponds to roughness factor, and θ_r equal to measured contact angle on the rough surface. The Cassie-Baxter phenomena is observed in heterogeneous surfaces. Phased area fraction is the ratio of percentage of uneven surface each phase contact angle vs percentage of total contact area. The Cassie- Baxter equation is defined as:

$$Cos\theta_{CB} = f_{SL}(1 + Cos\theta R) \dots \dots \dots \dots \dots \dots (3)$$

where, f_{sl} is the phase area fraction and θ_{CB} is the apparent contact angle. However, there are ''Gecko'' states and ''Lotus'' leaf states that are the mimic of gecko feet and lotus leaf. Gecko states give the high adhesion, and lotus leaf states give the auto clean surface property [76].

| (a) | (b) | (c) |
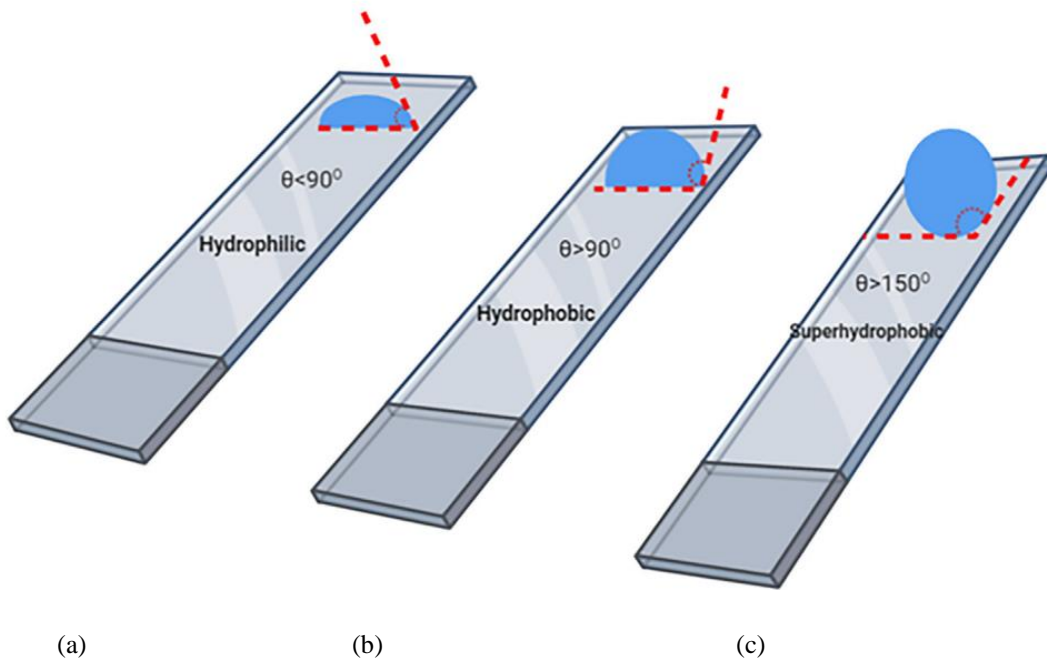
Figure.3.2. Relationship of contact angle with the states of the surface.
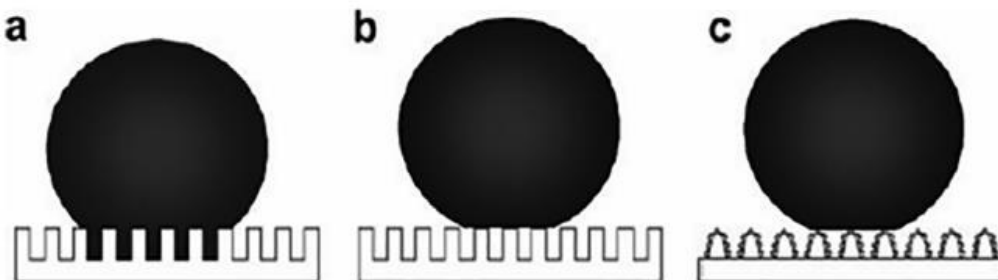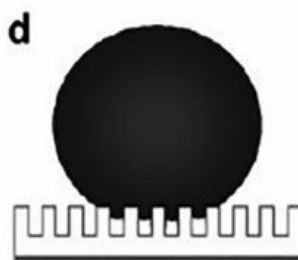
Figure.3.3 Water droplets on different states of superhydrophobic surfaces. (a) Wenzel sate (b) Cassie-Baxter state (C) Lotus leaf state (d) Transitional state of Wenzel and Cassie-Baxter states [92].

3.2.3 Medical diagnosis

(a) Biosensors

Biomarkers are well-known signaling parameters for cancer and tumor diagnosis. The accurate and precise detection of these biomarkers will help in early diagnosis of cancer. Superhydrophobic based biosensors are a new generation approach compared to conventional ones in terms of accuracy, stability, less analyte is required and high surface area to volume ratio. Oxidase type of enzymatic biosensors requires oxygen on to their surfaces for their complete enzymatic reaction. So, the superhydrophobic coatings contain trapped air pockets those are significant for supplying the oxygen molecules. These novel superhydrophobic coatings have solved the problem of oxygen diffusion constraint that can help in controlling the biosensing reaction's kinetics. In this con- text, Lei et al [93]. designed a biosensor incorporated with super- hydrophobic material by using platinum modified fibrous carbon mesh and glucose oxidase immobilized on it. Here glucose oxidase acts as a catalyst and platinum modified fibrous carbon mesh acts as a superhydrophobic surface which performs a significant act in inhibiting the detection, precision and accuracy of the biosensor. De Ninno et al [94]. fabricated a novel plasmonic biosensor which can detect the specific protein biomarkers of Alzheimer's disease. Here, they can detect ferritin protein in small blood samples by using plasmonic effects and superhydrophobic surface together [95]. Xu et al. described the detection mechanism of biomarkers of prostate cancer by using a superhydrophobic based biosensor. These sensors have excellent capabilities to detect microRNA (miRNA) in small samples [96].

3.2.4 Medical devices

(a) Medical implants

Superhydrophobic surfaces are anticorrosive, antibacterial and biocompatible, (Figure.3.4) and these properties make it best suitable for the application for biomedical implants. These coatings prevent the rejection of biomedical implant in the human body. Liu et al. reported the method of making magnesium alloy-based implants superhydrophobic by first treating the alloy with anodic oxidation method and further treated with stearic acid for an hour. Treatment of steric acid makes the surface of implant superhydrophobic. However, they achieved a water contact angle of 163°. Here, magnesium alloy is made anticorrosive by anodic oxidation method. Stearic acid is nontoxic and is used to enhance surface roughness. The annealing process is used for refining the nano/microstructures on the surface. Thus, this will give different water contact angles [97]. Supriadi et al.

developed a superhydrophobic dental implant by using commercial stainless steel 17-4PH, stearic acid and chemical etching compounds ($CuCl_2$ and HCl). These implants have the property of low adhesivity for food and bacteria. They reported a contact angle of 150° with this implant [98]. Patil et al. reported a composition of Ti-6Al-4 V alloy surface as one of the most prominent medical anti-septic materials. These implants have the property of anti-biofouling [99]. Nowadays, metallic sub- stances based vascular stents and valves are being used which are always in direct contact with blood. The prominent choices are Titanium and stainless steel. The anodic oxidation process is used to make Titanium superhydrophobic. Various titanium structures have been used with fluorinated coatings to reduce the platelet adhesion and thrombosis in valves and stents [100]. Superhydrophobic films also have been used in a plasma separator device [101]. Titanium dioxide nanoparticles are crosslinked with a poly dimethyl siloxane (PDMS) matrix used in blood repellent dressings and bandages [102].

(b) Superhydrophobic coating use in COVID-19 and in other medical instruments

COVID-19 is an airborne transmission disease, and aerosol can carry SARS-COV-2 virus in it. To check its transmission rate, researchers have developed a superhydrophobic coating for the face mask and personnel protective equipment. There are many materials which have low surface energy, but silica and graphene are biocompatible materials. Silver, copper, titanium nanoparticles are allocated on these surfaces because of their antibacterial and antiviral properties [89][88]. Transparent superhydrophobic titanium oxide-based coatings can be used for self-cleaning and antifogging, and such coatings might be very quiet useful for laparoscopic and endoscopic equipment. These coatings exhibit high optical transparency and nontoxic for the human body [84].

3.2.5 Hospital hygiene

Superhydrophobic nano septic coatings are explored and used in various surgical applications where the infection rate is so high. This coating acts as a barrier against the infection caused microorganisms and provides extra safety to doctors while doing surgical operations. Nano septic coatings are also explored in areas where the chance of getting an infection is high, such as in hospitals' examination rooms, frequently used devices like thermometers, stethoscopes, those generally come in contact with different patients. Few companies like Pureti and NanoLabs Corp use silver and titanium nanoparticles mixed in hydrophobic material provide coatings for surgical rooms, bathroom surfaces, doctor's boots, surgical gloves and walking aids [103].

3.2.6 Proposed and Supported Novel Materials and Fabrication of Superhydrophobic Nanocoating for biomedical applications.

Superhydrophobic materials have an interface of air between the solid and liquid phases when they are in contact with water. As a result, they exhibit a high-water contact angle, i.e., exceeding 150°. Superhydrophobicity is also attributed to a low roll off or sliding angle. The material which was used for fabrication of superhydrophobic surfaces has an intrinsically low surface energy and stable closely packed atomic structures which lead in high contact angles [104]. This is done without increasing the roughness of the material. Either the rough materials are coated with low energy materials which is known as the bottom-up method. Or else, these low energy materials are treated to induce roughness. Examples of this method are layer-by-layer methods, chemical deposition, electro spraying, electrospinning, and self- assembly. There is another method known as the top- down approach. An example of this method is lithography and ball milling [97]. The interpretation of various states of liquid contact

with the surface is shown in Figure.3.2. For a surface to be hydrophobic, it must possess high surface roughness. However, when surface roughness is increased, it leads to opacity of the surface due to increase in light scattering. As it is evident from this, due to surface rough- ness, transparency and surface roughness are two opposing properties. It is very important to strike a balance between the two in order to achieve appropriate properties. It can be done by carefully calibrating roughness size and selection of coating material [105]. Self-cleaning properties allow super- hydrophobic material to have antifouling, antibacterial, fog proof properties which makes it a suitable coating material over surfaces like glass and metals [106]. Also, owing to its blood-compatible nature, restricted protein binding, sup- pressed platelet adhesion, and cell phobic properties make superhydrophobic material a potential candidate for coating over laparoscopic surgical instruments [95]. Many strategies for fabrication of artificial superhydrophobic surfaces have been reported in literature for biomedical applications. FTIR-based chemical composition analysis of naturally present superhydrophobic coating over plant leaves revealed presence of organic film containing C, H, and O element [107]. Analysis also showed that low surface energy and high surface roughness are vital for achieving super hydrophobicity [108]. Inspired by nature, heterogeneity of material for artificial superhydrophobic transparent coating can be seen in literature. Use of both inorganic and organic materials along with their hybrids is reported [106]. Various promising materials such as silica-based nanoparticles, metallic oxide like zinc and titanium oxide nanoparticles, polymers having poly (methyl methacrylate) (PMMA) and polydimethylsiloxane (PDMS), hybrid materials having mixture of polydimethylsiloxane (PDMS) and hydrophobic silicon dioxide (SiO2), and micromachining by nanosecond laser are some of the available materials as a future potential solution for self-cleaning of lenses. Some of the materials and their fabrication methods were listed in Table 3.1.

3.2.7 Conclusion

This short review comprehensively summarizes the fundamentals of superhydrophobic coatings and their recent progress in medical diagnosis, medical devices, and hospital hygiene. Bio-inspired transparent and superhydrophobic coatings are gaining popularity in the research field as there is a growing demand for these materials in the medical industry. Explicit physiochemical and structural properties of superhydrophobic coatings make it suitable for many biological and biomedical system characteristics like fast response, sensitivity, accuracy and antifouling. The trapped air inside the roughness of these surfaces not only disrupt the growth of bacteria but also improve the consequences for enzyme-based sensors. These miraculous coatings are used in various applications like bandages to stop hemolysis, stents to prevent thrombosis and cell adhesion, plasma separator, and many more. To date, these coatings have been extensively used in a face mask, protective personal protective kits and face shields to protect and limit the transmission of coronavirus. Numerous materials and procedures are now accessible for the manufacture of these surfaces. The only constraint is with the large-scale production cost, biocompatibility and sustainability of the superhydrophobic coatings. Therefore, more focus must be laid on discovering suitable biomaterials for invasive procedures which are the most suitable methodologies for manufacture.

Table: 3.1 Superhydrophobic nano coatings methods for various biomedical applications

Superhydrophobic nano coatings

Silica-based nanoparticles

References	Method	Remarks	Transmittance	Contact angle (C.A)/ sliding angle (S.A)
[109]	Layer by layer deposition	Compatible for acidic and basic medium	89%	C.A = 160°, S.A < 1°
[110]	Sol–gel	Large-scale coating can be achieved	88%	C.A = 158°, S.A < 2°
[111]	Chemical vapor deposition (CVD)	High transmittance	90%	C.A = 152°, S.A < 8°
[112]	Surface functionalized by using perylene diimide (PDI) on silica nanoparticle surface	Useful for substrates that are heat sensitive	N.A	C.A = 150°, S.A < 10°
[113]	Solvothermal, dip coating	Biocompatibility might be an issue	90%	C.A = 150°, S.A = 4°
[114]	Sol–gel	Biocompatible and optical efficient	90%	C.A = 171.8°
[115]	Sol–gel and Spray coating	Eco-friendly	84.6%	C.A = 155.6°
[116]	Sol–gel	Biocompatible and highly transparent	90.22%	C.A = 172°, S.A = 2°
Metallic oxide				
[117]	Thin-film deposition	Biocompatible	85%	C.A = 175°
Polymers				
[118]	Photolithography	High optical transmittance	90%	C.A = 161.33°, 133.33°
[119]	CVD	Fluorine free	83%	C.A = 165°, S.A < 3°
[120]	Multilayer deposition	Biocompatibility might be an issue	98%	N.A
[121]	Spin coating	Biocompatibility might be an issue	88%	C.A = 159°
[122]	Plasma etching technique	Polystyrene is used	NA	C.A = 162°
[123]	Two-step process (synthesis and oxygen plasma treatment)	Biocompatible	NA	NA
[124]	CVD	NA	90%	C.A = 150°
Hybrid materials				
[125]	Solvothermal	Biocompatible	90%	C.A = 152°, S.A = 6°
[126]	Solvothermal	Biocompatibility might be an issue	90%	C.A > 150°
[127]	Flame soot deposition	Biocompatible	80%	C.A = 168°, S.A < 1°
[128]	Spin coating	Biocompatibility might be an issue	70%	C.A = 166°, S.A = 6.6°
Micromachining				
[126]	Nano-second laser	Biocompatible	NA	NA

3.2.3 A surface modification approach to overcome wetting behaviour of gallium based liquid metal droplets.

Here in this work, we report gallium oxide coating as a simple approach to convert mercury manometer glass tube, which has glass as a substrate to a nonwetting surface against surface-oxidized gallium-based liquid metal alloys. These alloys form an oxidized layer in ambient air (O2 >1ppm) and show stickiness to almost all surfaces that impact the residue-free movement of the liquid metal droplets. Herein, the physical vapor deposition technique was used for gallium oxide coating on substrates such as silicon wafer and glass slide. Moreover, various characterizations were carried out to support our outcomes. This method does not require any micro/nano machining or specific nanoscale surface topology.

(a) Transparent glass slide

(b) Fume hood where cleaning of glass slide has taken place.

(c) Glass slide holder of the instrument.

(d) Control unit of the device

(e) High vaccum chamber where glass slide has been placed.
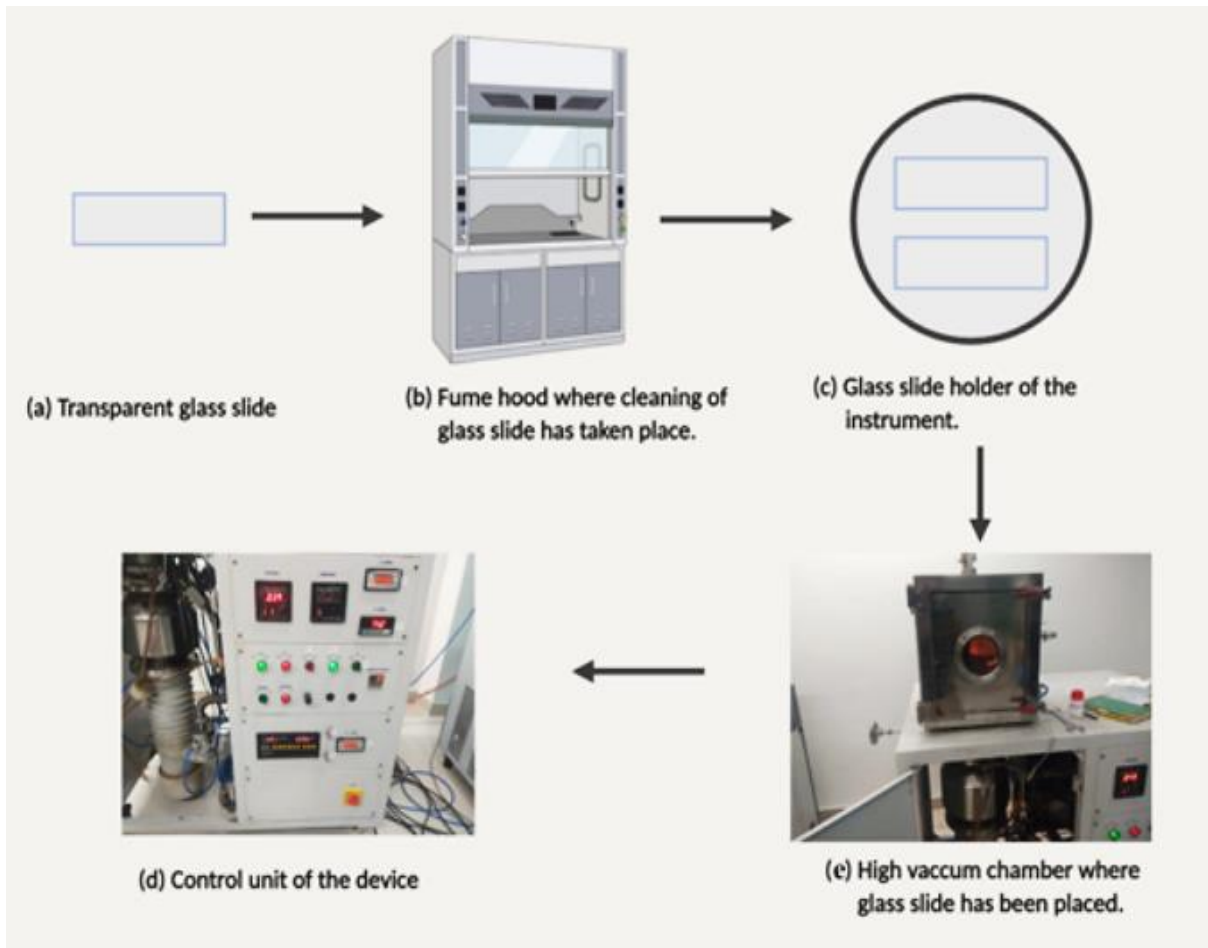
Figure.3.4 A PVD process used for coating gallium oxide on glass slide under ultra-high vacuum conditions.

3.2.3.1 Introduction

Mercury has traditionally been used as a measuring fluid in sphygmomanometers and thermometers. Mercury metal is toxic and harmful to the ecosystem. To mitigate this problem, Galinstan is utilized in thermometers as a suitable material to replace mercury; as per its commitment at the Minamata convention, the world health organization and various government agencies have issued guidelines regarding the ban of mercury sphygmomanometers in healthcare sectors. There is a pressing need for an alternative fluid with the same appearance and functionality to cater to this vacated space. The alternatives for mercury manometer are aneroid and the oscillometric type of blood pressure monitors. Both of these technologies suffer from inaccuracies, unreliability and higher maintenance issues. Clinician communities do not place the same faith in these methods as the mercury sphygmomanometer due to established standard procedures, the inertia of change, and accuracy issues [19]. Gallium based liquid metals are eutectic alloys that exist in a liquid phase at room temperature. The most prominent example is Galinstan (Gallium 68.5 %, Indium 21.5 %, and Tin 10 %), which is biocompatible, non-toxic, and the best alternative to mercury [129]. These alloys exhibit significant research interests in recent years due to their excellent thermal, electrical, and infinite deformability properties [130]. Gallium containing liquid metals have been explored for various applications, including energy harvesting [131], wireless power transfer [132], synthesis of 2D graphitic materials at room temperature [133], using as an interface for selective migration of dopants in 2d materials [134], mechanical energy induced CO_2 conversion [135], reconfigurable radiofrequency devices and biomedical devices [136], [137]. Recently, Galinstan has been replacing mercury in

28

thermometers while preserving the method and ergonomics of the measurement [138]. The only drawback of gallium-based alloys is that they are readily oxidized in an environment with oxygen content as low as 1 part per million (ppm), forming a thin oxide layer Ga2O, Ga2O3 of several nanometers forms on the surface of liquid metal droplets [139]. This viscoelastic oxide skin hinders the flow of liquid and changes the behaviour of liquid more like a gel. However, this oxide skin behaviour has been utilized in 3D printing of liquid micro components, reconfigurable electronics, and deformability applications [140]. This oxide layer is often considered detrimental because it sticks to almost any surface and leaves spot marks when trying to remove it. Such drawback has limited gallium- based liquid metal droplets in those applications where liquid metal movement is required, especially in microfluidic, energy harvesting, temperature monitoring, and blood pressure monitoring devices. Although Galinstan is a promising material to use in blood pressure monitoring devices, there is an issue of wettability with this material. However, various methods have been proposed in recent years to curtail this issue. Among them, chemical etching with acid (for e.g HCl) or treatment with base (NaOH) is a widely accepted effective method to eliminate the oxide skin [141], [142]. In contrast, the electrochemical process is also used to eliminate the surface oxide layer. Other methods are also being reported without removing the oxide layer, such as polytetrafluoroethylene (PTFE) solutions or submerging the naturally surface-oxidized liquid metal in water. These liquid materials work as a slippery layer on the oxide layer's surface, limiting the direct contact between the oxide layer and glass capillary use in measuring temperature, blood pressure, or microfluidics. Other surface modification techniques can lower the impact of adhesion, like coating the liquid metal droplets with PTFE powder [143], iron [144], and graphene [145]. Currently, super lyophobic surfaces are also gaining attention to reduce adhesion by surface oxidized liquid metal. This has included enhancing the surface roughness by using micro/nanostructured surfaces or using low surface energy materials, such as vertically aligned carbon nanotubes surfaces [146], sandblasted aluminum, and commercially available never wet spray coating [147]. All other methods have included foreign materials; in the present work, we are using a simple physical evaporation method to coat the surface of the glass with a gallium oxide layer. The step-by- step process of coating is shown in Figure.3.4. A gallium oxide coating mechanism is commercially used in thermometers by using a chemical vapour deposition (CVD) process [148], which includes many chemicals and gases. This process has lots of safety and handling issues.

3.2.3.2 Experimental Section

A. Materials and Methods

Borosilicate glass slide, silicon wafer, aqua regia (3:1 ratio of HCL and HNO3) solution was made and all above mentioned chemicals were purchased from SRL chemicals and used without any further purification. Gallium oxide powder was purchased from Sigma Aldrich with 99.99 % purity. Deionized (DI) water was used for washing and cleaning (18 MΩ resistivity). Firstly, the glass slide was properly cleaned with acetone and aqua-regia solution to remove all contamination of the glass slide. The glass slide was further ultrasonicated in the presence of DI water. The whole cleaning process was done inside the fume hood. The cleaned glass slide was further attached to

the rotating plate of the Physical Vapour Deposition (PVD) device with the help of insulated tapes, as shown in Figure.3.5. Gallium oxide (Ga2O3) powder was used as a precursor material, and a few milligrams of gallium oxide powder was placed inside the ceramic boat. PVD has an advantage over other coating methods such as CVD, dip coating, and Langmuir-Blodgett technique. The techniques mentioned above use various gases, chemicals, and layer-by-layer deposition, which encompasses toxic gases and residues. These techniques were not viable for industrial use, are cumbersome and time taking. Thus, we have used the thermal evaporation method amongst various PVD methods available because of its simplicity, and large quantity of material that can be evaporated on a variety of materials. In this method, material deposition was achieved in a vapour phase by heating source material in vacuum (pressure 5 x 10^{-6} mbar) with resistive heater and flow rate 0.1 A^{0}/sec. The vapor atoms were transported through a low-pressure zone in straight line path and deposited on the substrate. The step-by- step process of coating is shown in *the above* section in Figure.3.4.
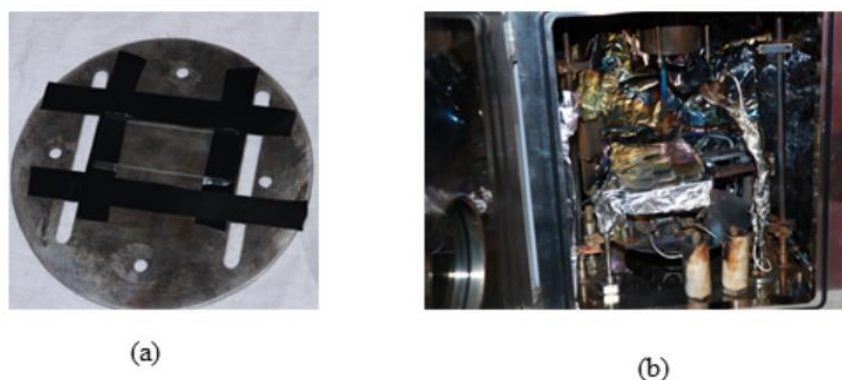
Figure.3.5 (a) Glass slide attachment on rotating plate of PVD device, (b) Chamber inside view where the rotating plate was placed.

B. Surface Characterization

The surface morphology of gallium oxide coating was characterized using a field-emission scanning electron microscopy (FESEM) (NOVA NanoSEM 450) at an accelerating voltage of 10 kV. The surface profile and the film thickness were measured by using a Bruker scanning probe microscope (SPM) in tapping mode with a tip radius of 5-8 nm (Bruker USA). The surface chemical composition of the gallium oxide coating was obtained using X-ray photoelectron spectroscopy (XPS). The pattern was recorded on a VG (ESCALAB250) electron photo spectrometer with a monochromatic AlKα (1486.6 ev) at 15 kV, and 10 mA and all the binding energies were referenced to the C1s peak (284.8 eV). To study the functional groups on the surface of the thin film, the fourier transform infrared spectroscopy (FTIR) was used. An Agilent Technology, model no Cary 660 FTIR spectrophotometer (Model No. K8002AA Cary 660, USA) operates at 4 cm^{-1} resolution. A diamond ATR plate was used for efficient data collection. FTIR analysis was performed using powder or film specimen samples, and scanning was done from the frequency range of 400 to 4000 cm^{-1}. FTIR spectra were recorded using the resolutions pro FTIR software by subtracting the background signal with the reference spectra. To study the optical properties of the film, the film was deposited on a transparent glass slide. Ultraviolet- visible (UV–vis) transmission spectrum was taken using a PerkinElmer spectrophotometer (wavelength range 190-800 nm).
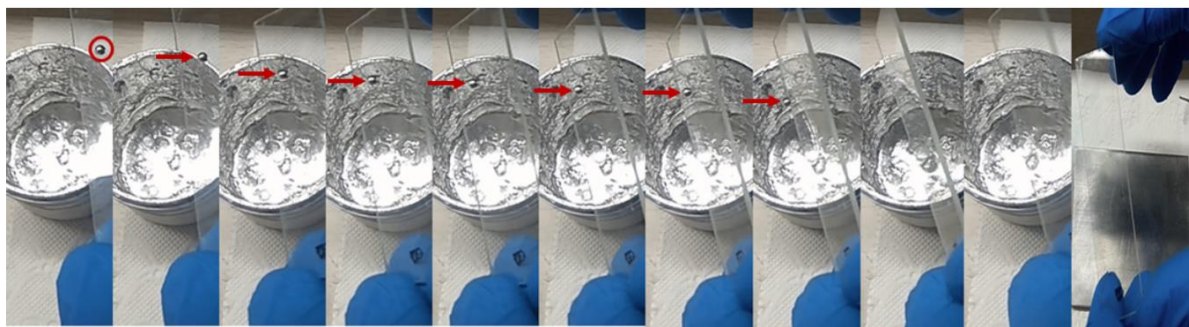
Figure.3.6 Dynamic flow test of liquid metal droplet marked in the red circle on a coated glass substrate.

C. Contact angle measurement

The contact angle measurement was performed by a contact angle analyzer (First Ten Angstroms, USA). The reported static contact angle was conducted at five different locations of the slide, and at the time of dispensing of Galinstan a still picture was captured, and with the help of the software, we calculated the contact angle. We have also conducted the dynamic flow test of the liquid metal over the coated surface. Figure.3.6 clearly illustrated that liquid metal droplets rolled down perfectly over the coated glass surface without residue. The sliding angle of the liquid droplet was approximately 5 to 8 degrees. All the contact angle measurements were conducted at ambient temperature (21–25 °C) and relative humidity (19–41%).

3.2.3.4 Results and Discussion

A. Surface Chemistry

XPS is performed to determine the elemental composition and the surface chemistry of the gallium coated glass substrate. The binding energy (B.E) range 0 to 1400 eV has been used in the full survey analysis, and it is shown in Fig.4 (a). Peaks C1s, O1s, Ga2p3 were identified in XPS full scan. The two prominent peaks Ga 2p1/2 and Ga 2p3/2 are coming at B.E (1144.9 eV) and B.E (1118.1 eV), respectively. The separation between the two peaks is 26.8 eV, and this value is agreed with the binding energy of Ga2p. Figure. 4(c) corresponds to the presence of C1s peak at 286 eV, Fig. 4(d) shows the O1s peak at 531.2eV, and this peak corresponds to the major contribution of Ga-O bonding. [149]. The FTIR analysis also brings forth the presence of gallium and oxygen and their bonding nature. The spectrum shows a band at 451.5 cm-1, and 613 cm-1, relating to the vibration mode of Ga-O as shown in Fig.5(a) [150]. The UV-Vis results revealed that a strong absorption peak observed at 270 nm [150], which is in direct correlation to UV- C radiation, and for the other region it is showing a good transmission rate of (96 %), our main area of interest is in visible region so, GaOx thin film exhibit a good transmission rate in the visible range as shown in Fig.5(b).
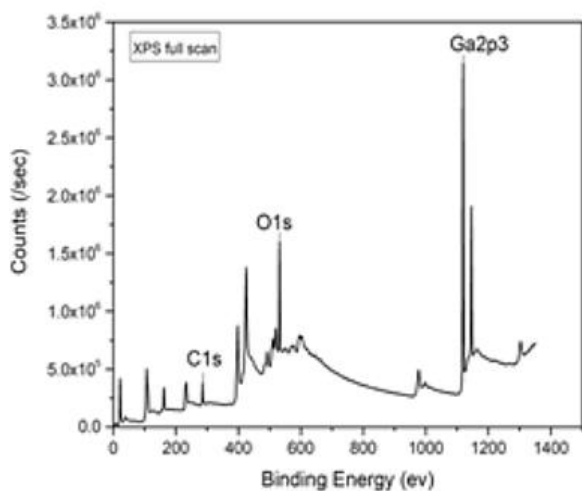
(a)
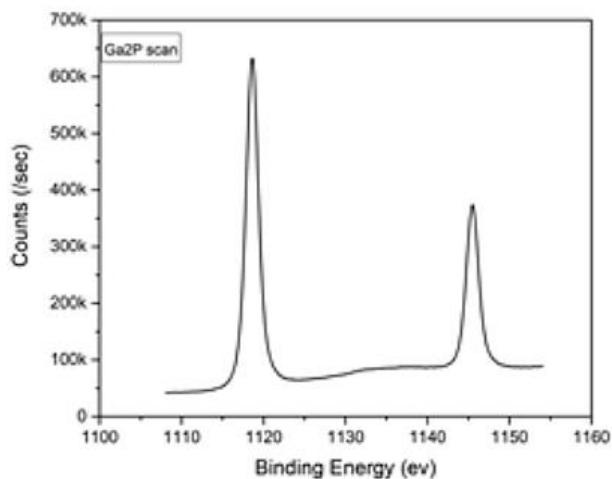
(b)
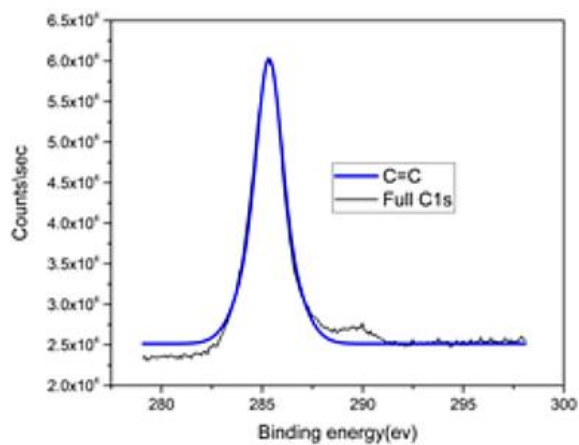
(c)
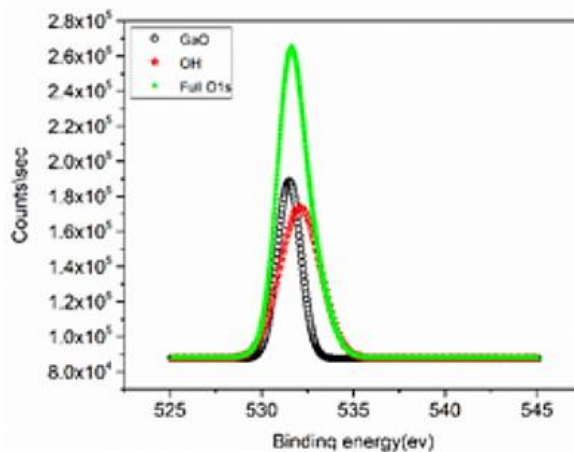
(d)

Figure.3.7. XPS spectra of GaOx-coated glass slide: (a) Full XPS survey, (b) High-resolution spectra of Ga2P, (c) Deconvolution of C1s high-resolution spectrum, (d) Deconvolution of O1s high-resolution spectra.
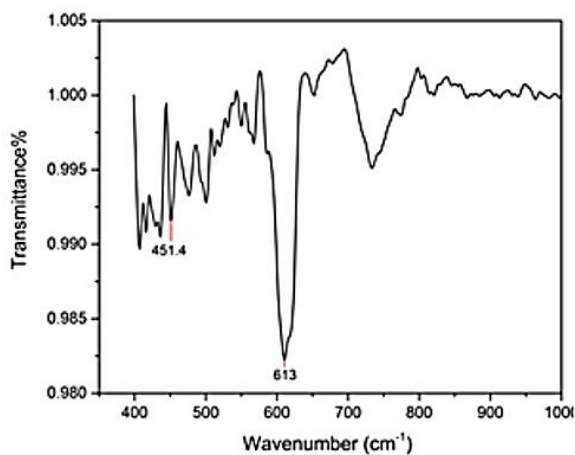
(a)
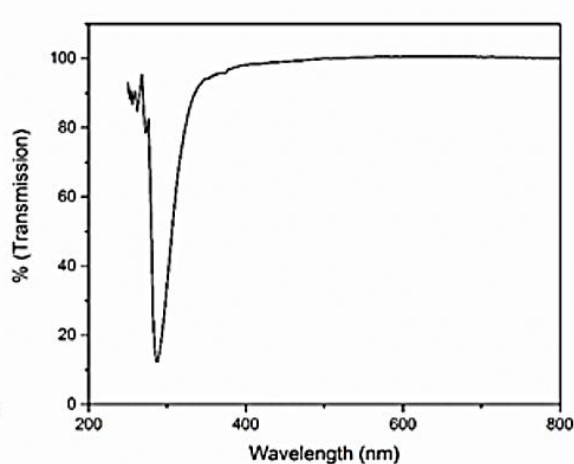
(b)

Figure.3.8 FTIR spectra of gallium oxide coated glass, (b) UV Spectra of gallium oxide coated glass.

B. Surface Characterization

The surface morphology of the fabricated coating film profile is observed through scanning electron microscopy (SEM). The thin layer of gallium oxide is coated on top of silicon, as shown in Figure.3.9 (a). Moreover, the gallium oxide layer consists of nanoparticles with varying sizes and has been uniformly distributed on the whole surface. Figure.3.9 (b) is taken from the edge, and it clearly shows the difference in surface areas of coating and the substrate material. In addition to this, atomic force microscopy is used to analyze gallium oxide coated Si surface's, surface topography in tapping mode is shown in Figure.3.10 (a), (b). The 3D topography confirmed the presence of gallium nanoparticles with various sizes, as visualized and is confirmed in SEM. The uneven spikes show the random size distribution of gallium nanoparticles, indicating a rough surface profile having a mean surface (Sa) 0.97 nm with coating on silicon substrate and 0.160 nm root mean square of bare silicon substrate. The mean surface profile is calculated on a coated glass substrate, and it came out to be 56.98 nm and bare glass 47.86 nm, respectively. As per the previously reported literature, studies have shown that very small amounts of roughness are sufficient to prevent adhesion [151], [152]. The 3D profile of gallium coated glass substrate and bare glass substrate is shown in Figure.3.10 (c) and (d), respectively. Moreover, the average thickness of gallium oxide coating is analyzed by using shadow masking of the substrate before coating with the help of insulated tape which gives the clear idea of coated and non-coated surfaces, the average thickness of the film is calculated and found out to be 80.12 nm.

C. Contact angle measurement

Contact angle measurement is conducted to check the lyphobicity of gallium oxide coated surfaces against surface oxidized Galinstan liquid metal droplets, as visualized in Figure.3.11. The Galinstan droplet is not spherical but has some irregular shapes. This demonstrates that Galinstan formed an oxide layer, which prohibits the droplet from forming a spherical shape. We have achieved a contact angle of 137.69°. Therefore, as a result, it has been observed that at this contact angle, Galinstan could not stick to the gallium oxide coated surface.

(a)   (b)
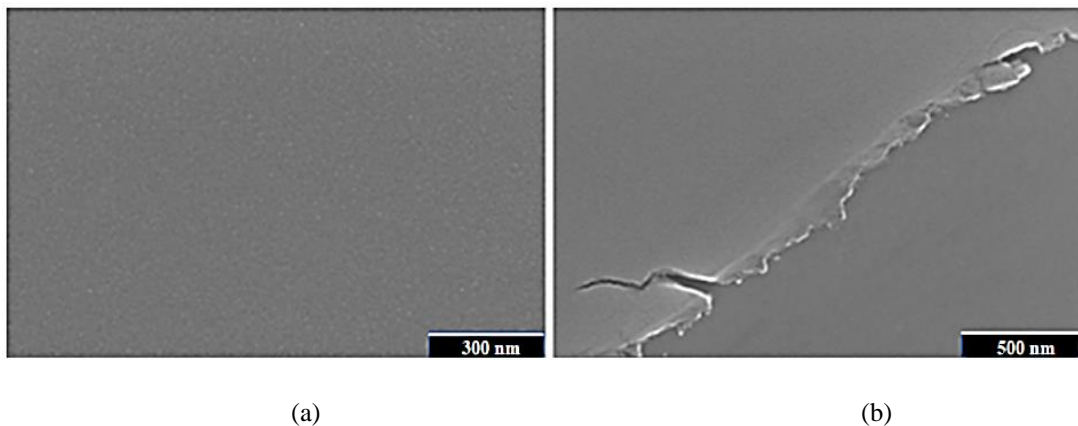
Figure.3.9. FESEM images of the gallium oxide-coated silicon wafer (a) Topographical view of the coated film, (b) Coated film view at the edge of the substrate.
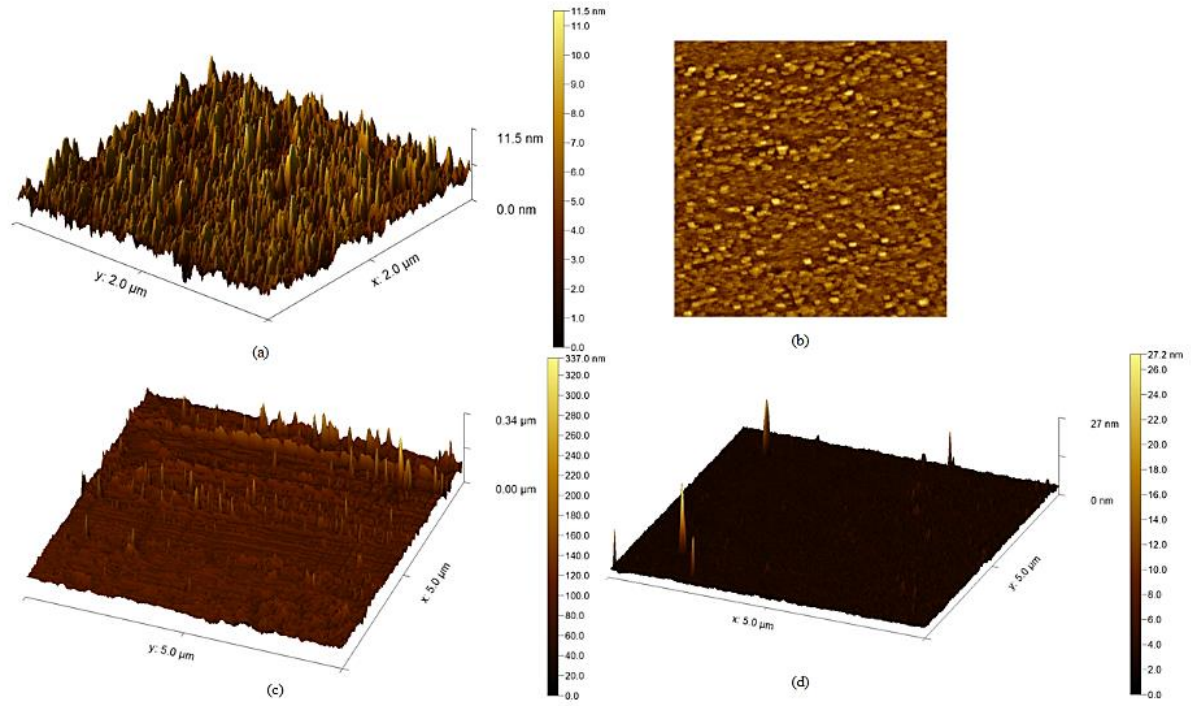
Figure.3.10 AFM images of the (a) 3D profile of silicon substrate coated with gallium oxide. (b) 2D view of gallium oxide coated thin film on silicon substrate. (c) 3D profile of gallium oxide coated glass substrate. (d) Bare glass surface 3D profile.
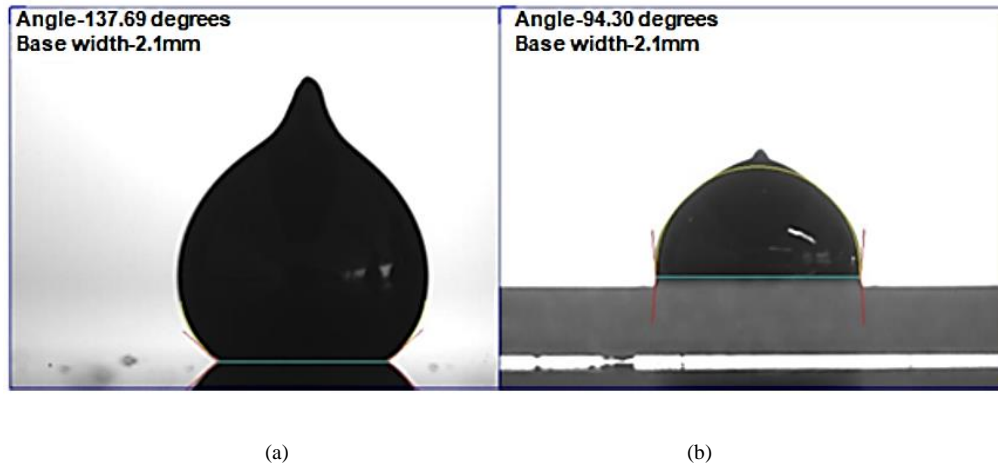
Figure.3.11. (a) Galinstan drop on the coated surface, (b) Galinstan drop on a bare glass surface

3.2.3.5 Conclusion

The thin native oxide layer of gallium metal is responsible for wetting almost all surfaces and spot with some residue onto the surface. We have used a simple and convenient method of coating physical vapour deposition to coat the gallium oxide coating in this work. The coating is capable enough to make any flat surfaces to non-wetting surfaces against surface oxidized gallium-based liquid. We have conducted various characterization to support that lyophobicity comes from the surface roughness innate to the gallium deposition technique. Finally, the gallium coating is capable enough and provides a non-wetting path on which surface oxidised liquid metal does move

34

freely. This homogenous material surface treatment for gallium-containing liquid metal may remove all barriers where wetting is an issue. On the other side, it can be the best substitute for exploring gallium-based alloys in various healthcare products like thermometers and blood pressure measurements. This technique is feasible for flat and for non-planar surfaces.

Chapter-4: Merkfree design and development and Manufacturing of the prototype using 3D printing.

4.1 Additive manufacturing use in biomedical engineering.

Additive manufacturing, also known as 3D printing, has the potential to revolutionize the production of medical devices. By building up successive layers of material based on a digital model, additive manufacturing allows for the creation of complex shapes and structures that would be difficult or impossible to manufacture using traditional techniques. One major advantage of using additive manufacturing for medical devices is the ability to customize products to meet the specific needs of individual patients. For example, 3D printing can be used to create customized prosthetics and orthotics that are perfectly tailored to the patient's body. In addition to customization, additive manufacturing also offers the potential for reduced production costs and lead times. By eliminating the need for costly molds and tooling, and by allowing for the production of small quantities of customized products, additive manufacturing can significantly reduce the cost of producing medical devices. There are several different technologies that can be used for additive manufacturing in the medical field, including stereolithography, selective laser sintering, and fused deposition modeling. Each of these technologies has its own unique capabilities and limitations, and the choice of technology will depend on the specific requirements of the medical device being produced. Despite the many potential benefits of using additive manufacturing for medical devices, there are also some challenges that need to be addressed. These include ensuring the quality and safety of 3D printed products, as well as addressing regulatory issues related to the use of these products in the medical field. Overall, additive manufacturing has the potential to transform the way medical devices are designed, manufactured, and used. As technology continues to mature and become more widely adopted, it is likely to have a significant impact on the medical industry.

4.1.1 Evolution of 3D printing

3DP was first introduced by Hull and Freed in 1986 in the United States and further was patented as the first rapid prototyping device. The first commercial 3DP SLA-250 came in 1988. Following the invention of SLA came other rapid prototyping technologies. As per the time, the 3DP technology is growing day by day with the rapid maturing of various techniques, such as inkjet printing, various extrusion techniques for live cell printing, direct laser printing, and many more. Process architecture of the 3DP is shown in Figure. 4.1.
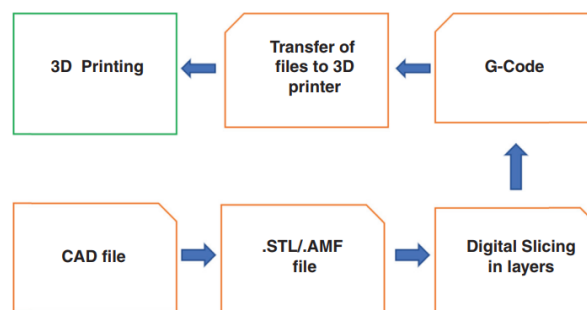
Figure.4.1 3D printing process.

4.1.2 Biomaterials

Biomaterials are materials that are compatible with the living species as well as with the environment. The origin of the biomaterial is from natural sources (such as collagen, chitin/chitosan, gelatin, and silk) or synthetic sources such as (metals, ceramics, polymers). The term biomaterial first came into existence in the 1970s, and with the flow, the society of biomaterials was formed in 1974. The functionality of biomaterials is analyzed by their performance characteristics, its specific usage, and ability to resist harmful effects on the environment during its usage. For example, various biomaterials have been developed, and employed in various medical devices used in implants, transplants, prostheses, and regenerative medicine. Therefore, biomaterials must follow the explicit criteria for 3D printing, as shown in Figure. 4.2.
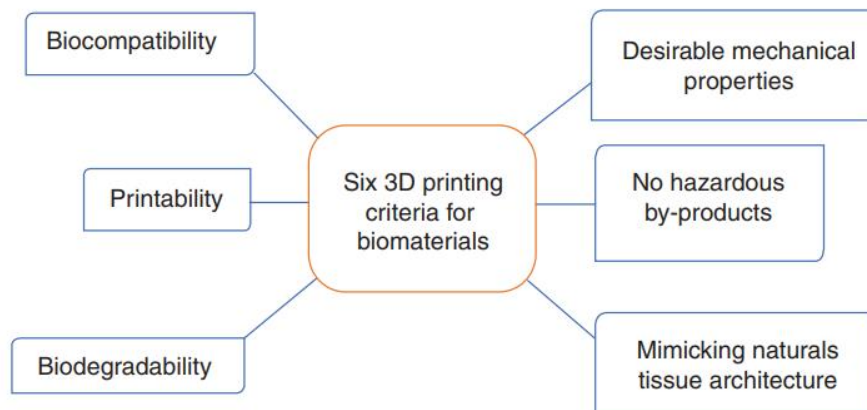
Figure 4.2 Selection criteria of biomaterials for 3D printing.

4.1.3 Overview of 3D printing technologies

The printing technique strictly decides the execution of printability of a biomaterial. Although it is possible to print the same material by using multiple printing techniques, selecting the accurate technique depends upon the application where it will be used. Similarly, the other factors like differences in cost, building time, accuracy, and characteristics will also define the pertinent printing approach. This chapter will focus mainly on four types of 3D printing technologies for biomedical applications: extrusion-based methods, optical-based (photopolymerization) methods, particle fusion-based methods, and inkjet printing, as shown in Figure.4.3 and provides insight about various biomaterial types in accordance with its applications and printability.
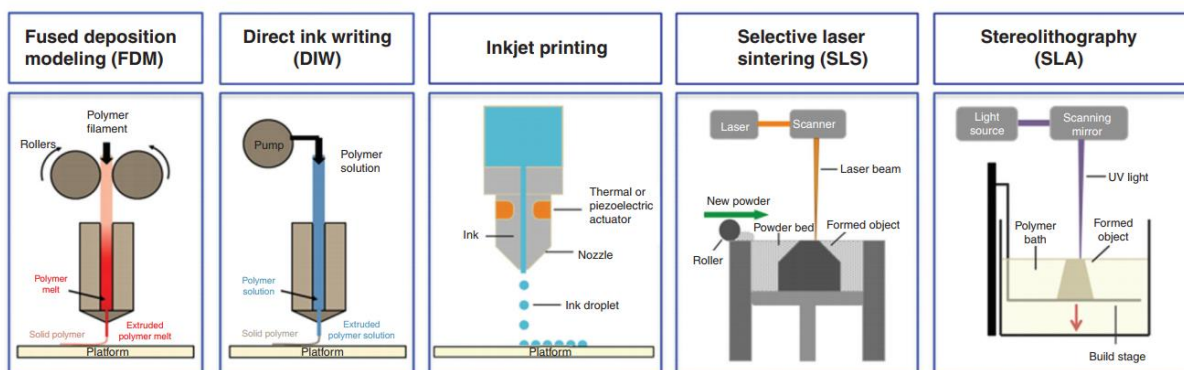
Figure. 4.3. Schematics depicting 3D printing techniques extrusion-based methods such as fused deposition modelling (FDM) and direct ink writing (DIW) inkjet printing, particle fusion-based method such as selective laser sintering (SLS), and light-based method stereolithography (SLA) [153] .

(a) Extrusion-based methods

Extrusion-based technology is something in which a material will be extruded using some extruder (mechanical actuator or DIW) pneumatically using a piston, and screw. It is one of the frequently used prototyping techniques for various biomedical applications such as making the body of medical devices, scaffolds, prosthetics, and tissue engineering. Hence, depending upon the extrusion type, it is further mainly classified into two types: FDM and DIW which are distinguished by non-identical extrusion mechanisms, as shown in Figure. 4.4. The idea behind FDM is that a filament is forced through a nozzle with the help of a gear motor; the first filament is in contact with an integrated heater nozzle (typical range 0–250°C), and then it melts to form individual lines that solidify onto a build plate (printer bed).The temperature of the nozzle is first set following the filament used, and when it starts extruding, the nozzle follows a predefined path as per the model defined in the G-code. G-code is a machine-level language for 3D printers, and it is converted by the various available software such as Voxelizer and Ultimaker Cura (open licensed). The typical diameter of the FDM nozzle ranges from 0.2 mm to 1.75 mm. The FDM-based technique is best suited for those biocompatible polymers whose melting point is somewhere around 200–250°C. The other type of extrusion-based printing is DIW; as the name indicates, it uses a viscous paste ink as a precursor; these inks are either polymer solutions in a preferably water-miscible or a buffer solution, low boiling point solvent (such as dimethyl sulfoxide (DMSO), dichloromethane (DCM), and tetrahydrofuran (THF). Moreover, these solvents evaporate just after the extrusion and leave a solid polymer matrix behind or hydrogels that maintain the architecture of the geometry following extrusion. This type of 3DP is Extrusion-based technology is something in which a material will be extruded using some extruder (mechanical actuator or DIW) pneumatically using a piston, and screw. It is one of the frequently used prototyping techniques for various biomedical applications such as making the body of medical devices, scaffolds, prosthetics, and tissue engineering. The idea behind FDM is that a filament is forced through a nozzle with the help of a gear motor; the first filament is in contact with an integrated heater nozzle (typical range 0–250°C), and then it melts to form individual lines that solidify onto a build plate (printer bed).The temperature of the nozzle is first set following the filament used, and when it starts extruding, the nozzle follows a predefined path as per the model defined in the G-code. G-code is a machine-level language for 3D printers, and it is converted by the various available software such as Voxelizer and Ultimaker Cura (open licensed). The typical diameter of the FDM nozzle ranges from 0.2 mm to 1.75 mm. The FDM-based technique is best suited for those biocompatible polymers whose melting point is somewhere around 200–250°C. The other type of extrusion-based printing is DIW; as the name indicates, it uses a viscous paste ink as a precursor; these inks are either polymer solutions in a preferably water-miscible or a buffer solution, low boiling point solvent (such as dimethyl sulfoxide (DMSO), dichloromethane (DCM), and tetrahydrofuran (THF). Moreover, these solvents evaporate just after the extrusion and left a solid polymer matrix behind or hydrogels that maintain the architecture of the geometry following extrusion. This type of 3DP is used for live cell and tissue printing because less stress is applied to hydrogels when they pass through the nozzle. In both the techniques, the extruder moves in x and z directions, and the bed moves in the y-direction, respectively. 3D-bioplotter is one of the extrusion-based printers used in medical applications such as tissue engineering and bio pattering. Further applications of the 3D bio plotter include bone regeneration, cartilage regeneration, soft tissue bio fabrication, drug release, organ printing, etc. It has an unsurpassed large choice of materials like ceramic/metal pastes, thermoplastic, hydrogels.

These types of bioprinters have multiple printheads which can be used to deposit different cell types (muscle cells, organ-specific, blood vessel), which is an important feature for fabricating whole heterocellular tissues and organs. Recently, Novogen MMX Bioprinter is another extrusion-based device using the suction and ejection technique enabling automatic reloading of material instead of manual loading. The printer works in a contactless environment reducing the chances of disinfection and cytotoxicity [154].
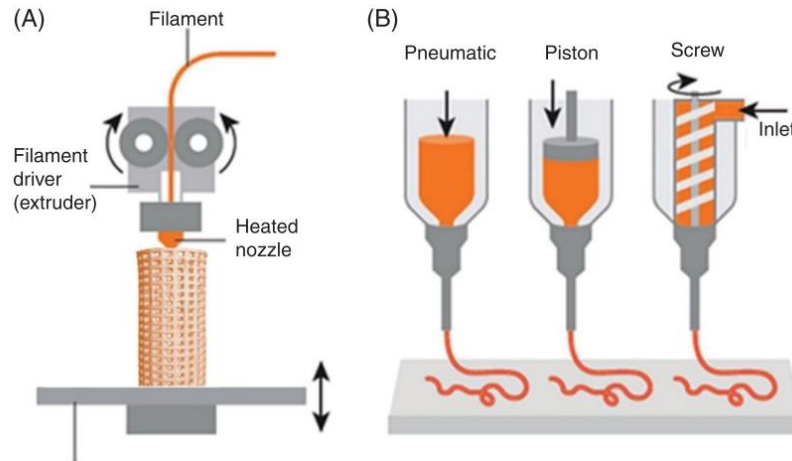
Figure. 4.4. Schematic representation of extrusion-based techniques (A) FDM method, (B) DIW method [155].

(b) Optical based (photopolymerization) methods

Optical guided 3D printing, also known as stereolithography (SLA), was first developed, and commercialized by Charles Hull and his team. SLA uses the UV, and laser for projecting the model over a bath of resin (photopolymerizable). The resin consists of a monomer unit, photo initiator, and binders. The whole process of printing is done layer by layer, first, a UV or laser is projected over the resin and then the resin gets polymerized and hardened, this whole process is controlled by the movement of the bed and the same process is repeated until the final model builds up. The final step is post-processing where all support structures are removed and cleaned. The best thing about this technique is that only projected light polymerizes the resin, which is focused, and the rest remains in the storage tank. Optical-based technique takes the least amount of time compared to the FDM technique and it reaches up to a few micrometers of resolution. There are a variety of resins available according to the colour and material type. The features available in the software are settings related to exposure time and curing time which is prior to input before printing. The biocompatible resin is used for various applications such as manufacturing medication-laden tablets [156], dental implants, and tissue engineering.

Process steps involved in SLA printing are as follows:

1. First, the design is either imported from CT or MRI or designed in CAD software.

2. The CAD model is converted into. stl format.

3. The. stl format is then imported into a 3D formatting software, where necessary operations related to printing are implemented such as quality, infill, build plate adhesion, and support generation.

4. To give a better understanding of the processing of CAD files in 3DP chitubox (open-source software).

(c)   Particle fusion-based 3D printing methods

The best-known examples of particle fusion-based techniques are selective laser sintering (SLS) and particle binding (PB) (Figure.4.3). Both SLS and PB have found a variety of applications in industrial prototyping because they are able to produce complex geometries using metals, polymers, and ceramics. SLS works by using a directed laser beam to heat materials, such as polymers, metals, and ceramics, just above their melting point. The laser is then used to draw a pattern on the exposed surface, causing the area underneath to heat up and melt. The melted material is then fused to form a layer. This process is repeated, with powder being spread over the previous layer and flattened with rollers, until the final model is complete. However, it should be noted that for SLS to be effective, the material should be able to be processed into fine powder form (ranging from 10 to 100 micrometers). In comparison to other 3D printing techniques, SLS machines are typically slower, bulkier, more expensive, and require a large amount of materials. It can also be challenging to remove materials in certain shapes. The PB technique is similar to SLS but utilizes a binding solution to fuse particles layer by layer, followed by a high temperature sintering step to solidify the powder into a final 3D object. Both SLS and PB have a resolution range of 700-1000 micrometers on the horizontal axis and 100 micrometers on the vertical axis. The resolution depends on the particle size of the powder, which typically ranges from 10-100 micrometers. Both techniques have been researched for use in hard tissue engineering applications, such as orthopedics and oral surgeries.

(d) Inkjet printing.

Inkjet printing is a technique that involves the precise placement of small droplets of ink onto a surface to create structures. This is achieved by using a nozzle to dispense droplets, which are then solidified. To speed up the printing process, multi-nozzle print heads are often used. There are two main types of inkjet printers available: continuous inkjet (CIJ) and drop-on-demand (DOD) printers. The main difference between the two is in the way ink is delivered - CIJ printers have a continuous output of droplets, while DOD printers produce droplets on demand as shown in Figure 4.5.   Any unused ink in CIJ printers is typically recycled and used again. Drop size in CIJ printers is around 100 micrometers in diameter, while drop size in DOD printers can range from 25 to 50 micrometers. The flow of droplets depends on the viscosity of the ink and is typically less than 10 centipoises. The overall shape of the droplets is affected by surface tension, which typically falls between 28 and 350 millinewtons per meter. Inks used in inkjet printing can include photocurable solutions, colloidal solutions of high-weight polymers, or ceramics with low viscosity. This technique is used in applications such as tissue engineering, scaffold production and living cell printing. However, it is important to consider factors such as shear forces and temperature during the process.
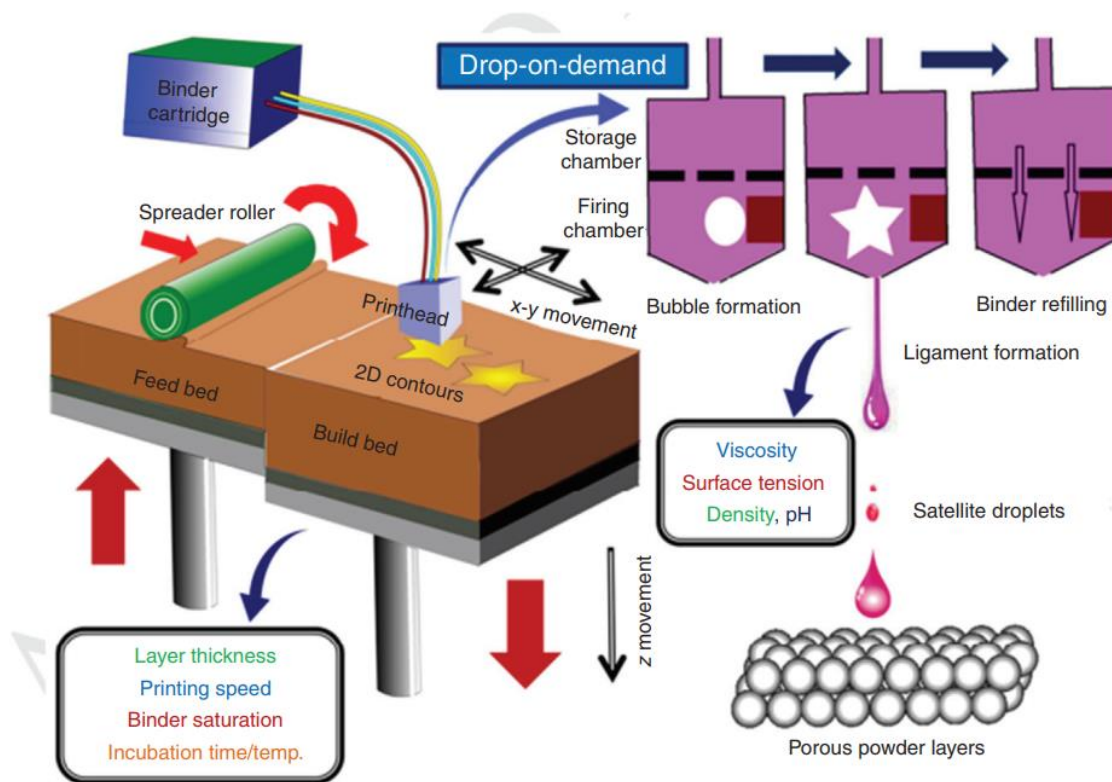
Figure.4.5. Diagram of the working principle of 3D printing and schematic of drop on demand.

4.1.4 Material selection and its advantages

The choice of materials in biomedical engineering plays a crucial role in the success of the resulting product. Biocompatibility and toxicity are important considerations, as well as other mechanical properties that may be necessary for the intended application. Table 4.1 provides information on various materials used in different 3D printing technologies, along with their advantages and disadvantages. While organ bioprinting and tissue engineering are still in the early stages of development, there have been some promising advances, including the successful 3D printing of knee menisci, heart valves, spinal disks, various types of cartilage and bone, and artificial ears. Researchers have also used 3D bioprinting to repair human articular cartilage and create artificial livers by depositing cells within biocompatible hydrogels. In a notable case study published in the New England Journal of Medicine, a 3D printer and CT images were used to create a bioresorbable tracheal splint, which was successfully implanted in a baby with a rare disorder. It is expected that the splint will fully dissolve within three years of the surgery.

Table 4.1 Provides information on various materials used in different 3D printing technologies

AM Process	Material	Biomedical Applications	Advantages	Disadvantages	References
FDM	Polymers, Carbon fibers, Polylactic acid (PLA), Acrylonitrile Butadiene Styrene (ABS), Polycarbonate (PC), Nylon, Medical grade titanium, Polyether-ketone-ketone, Polyether-ether-ketone (PEEK), Chiotin (CI), Chitosan (CS), Collagen (Col), Active pharmaceutical ingredients, Polyvinyl alcohol (PVA) containing paracetamol or caffeine	Scaffolds for cell culture, Tissue engineering, Prosthetic hand, Lower limb prosthetic, Trabecular bone, For the broken knee, Biomedical implant, For fabrication of calvarial bone, Cartilage and skeletal muscle, for drugs	Low cost, High strength, Composite materials, not using toxic solvents	Nozzle clogging, Anisotropy, Lower resolution, Thermal degradation of the polymer	[157][158][159][160][161][162][163]–[165]
DIW	Alginate (ALG), Chitosan (CHI), Collagen, Gelatin, Silk	Tissue regeneration, Wound healing, Drug delivery, Structures with different geometries, Sizes and materials, Formulation of Inks			[155]
SLA	Photocurable resin (epoxy or acrylate-based resin), Polycaprolactone (PCL), PLA, ABS, PLLA, Acrylonitrile butadiene styrene and TangoPlus Full Cure 930, Gelatin based matrix and	Scaffolds for cell culture, Tissue and organ, Prosthetic hand, For support and medical, For bone engineering applications, For osteonecrosis, osteoporosis, and bone	High Resolution, Fast, good cell viability, Nozzle free	Cytotoxicity, High cost, Material limitation, Possible harm to deoxyribonucleic acid (DNA) by UV	[164], [157], [166], [167], [168],[169],[170]

	extruded drug paste	defects, For training, Tissue Engineering			
SLS	Polycaprolactone (PCL), Polyamide (PA) power, PLA, ABS, PC-ABS, Laser-machined carbon fiber composite (CFC), Biocompatible ceramic HA/TCP, Nylon Powder and MB	Temporary and degradable rigid implants, Implant prostheses, Robotic sensing, For bone engineering applications, For soft materials in biological and pharmaceutical applications, Tissue Engineering	materials in biological and pharmaceutical applications, Tissue Engineering	High cost Medium resolution post-processing required	[164], [155], [166],[167], [168] [171], [170]

4.1.5 Conclusion

Additive manufacturing (AM) has revolutionized the manufacturing industry by introducing a variety of printing techniques that can quickly and easily create complex geometries. Research in AM has also unlocked new possibilities in the biomedical field, allowing for the creation of complex, custom-made products that would have been difficult or impossible to produce using traditional methods. This progress has given hope to individuals with disabilities, as it offers the potential for them to receive artificial organs and improve their quality of life.

4.2 Merkfree design

The Sphygmomanometer was first designed in solid works (CAD designing software). All attributes such as density of measuring fluid, volume requirement of fluid in tank and scale were taken into consideration. The enclosure and the tank were manufactured by 3D printing. The enclosure has been printed by fused deposition modelling (FDM) in which poly lactic acid (PLA) filament was used. The initial design of the tank in CAD are shown in Figure.4.8. The tank and the upper tube holder were printed with stereo lithography assembly (SLA) as shown in Figure.4.9. The device components are explained below. The filter unit contains filter paper which allows air to pass through but does not allow the measuring fluid to get out from it. It also holds the upper side of the glass tube in place. The tank is where Galinstan is stored when device is not in use. This needs to be air-tight to hold air pressure Figure.4.6. One end of the tank is connected with the rubber tube from the bulb and the other end is connected with the lower end of the glass tube. The scale was 3D printed by using dual colour filament using FDM technique. To display the measurement in mmHg the scale needs to be recalibrated using the formula shown in Eq. (1).

$$\Delta H_{tu} \ = \ 133.3/(\ \rho_m g \left(\frac{\pi r_{tu}^2}{A_{tn}} + \ 1 \right) \dots \dots \dots \dots \dots \dots \dots \dots . (1)$$

The ΔH_{tu} is the change in height of the fluid inside glass tube for every mmHg pressure, A_{tu} is the area of cross-section of the tank, r_{tu} is the inner radius of the glass tube, ρ_m is the density of the material. The display scale is calibrated to show the measurement in mmHg since this is the standard measure in all BP sphygmomanometers. Galinstan has a density of 6.44 g/cc which is almost half that of mercury (13.6 g/cc), the column height is nearly doubled. We use a tank with cross-sectional area of 695.6 mm² and a measuring tube with an inner diameter of 3 mm. Thus, by using Eq. (1), the scale is calibrated to 1 mmHg per 2.1 mm. The outer enclosure box has two components—the flap on which the tank, and the scale have been attached, and the base box, where all the accessories such as the cuff and the bulb are kept. The flap is connected with the base-box through 3D printed hinges to provide 0-to-120-degree freedom of movement. Magnetic locks were provided in the device between the flap and box as shown in Figure.4.7**.**

4.2.1 Chemical Treatment

Galinstan has Gallium in it, which forms a thin oxide layer when it is exposed to the environment. The thin oxide layer creates a low surface tension and makes it stick with the glass tube, disturbing the visibility of the fluid. To remove the stickiness behaviour of the fluid we have used reducing agents such as HCL and NaOH. 5 Molar NaOH solution was found to give best results. The NaOH solution only etches the oxide layer and does not hamper the Galinstan or the glass tube. We put a few milliliters of NaOH on the top of Galinstan in the tank. Because of its low density, a small meniscus of NaOH is always maintained above the Galinstan column. The weight of this meniscus is negligible, and it is transparent and hence nearly invisible.
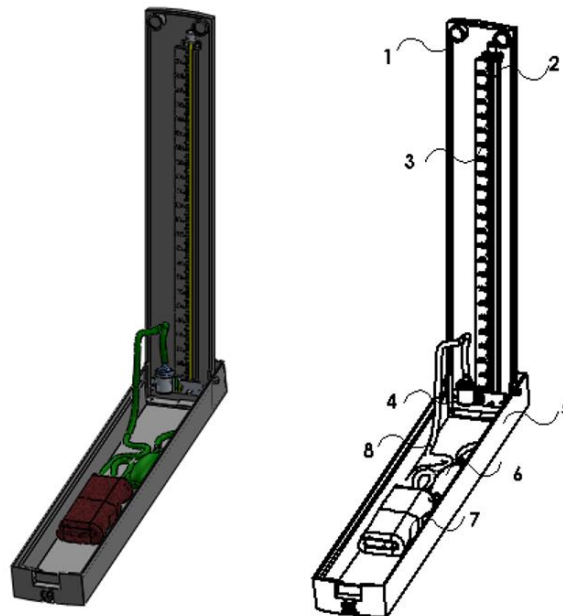
Figure.4.6. Merkfree 3D Design, 1) Magnetic lock, 2) Glass tube, 3) Scale, 4) Tank, 5) lower flap, 6) Bulb, 7) Cuff, 8) Connecting tube.

Figure.4.7. 3D manufactured full device end to end, enclosure box was manufactured by FDM method.

(a)   (b)   (c)
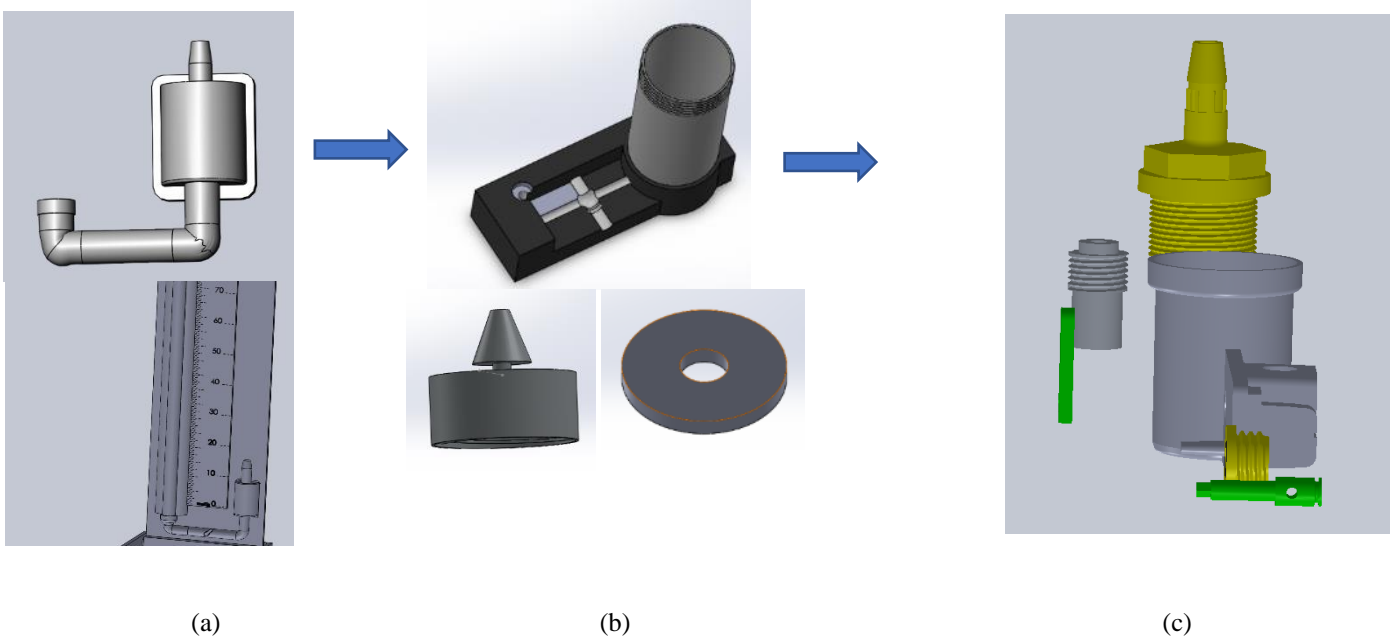
Figure. 4.8 Various transitions in tank design (a), (b) Initial CAD designs, (c) Final CAD design.

Figure.4.9 Final 3D manufactured part through SLA method.

Chapter-5: Clinical trial of Merkfree

5.1 Device operation.

The look, structure, and feel of the device remain the same as the conventional MS. Auscultatory method is used to measure BP using this device as with the MS. The prototype of the device is shown in Figure.5.1 (a). Galinstan has the same silvery color as mercury. Thus, there is no significant change in visualizing the fluid across the tube [172] .

5.2 Ethics approval.

This study was conducted in accordance with relevant guidelines, regulations and approved by the Institutional Ethics Committee (IEC:2021-654) of Dayanand Medical College Ludhiana, India. Written informed consent was obtained from all the participants of the study.

5.3 Clinical trial

To compare the performance of the proposed Merkfree sphygmomanometer against commonly used sphyg-momanometers in hospitals, we performed clinical trials after ethical clearance from the Institute ethical committee (IEC) of Dayanand Medical College and Hospital, Ludhiana. All methods were performed in accordance with the relevant guidelines and regulations. This clinical trial included all age groups except those who had recently undergone cardiovascular surgery and very old people who had vasomotor problems. All the measurements were performed by trained clinicians Figure. 5.1 (c). A total of 252 participants, across various age groups (12–80 years, mean ± standard deviation = 41.23 ± 15.56 years) and sex (143 male, 109 female), were tested for systolic blood pressure (SBP) and the diastolic blood pressure (DBP) measurements. Informed consent was obtained from all subjects and/or their legal guardians. We took comparative measurements with the Merkfree and compared these with the commonly used MS (BPMR-120 Mercurial BP Delux from Diamond company) and a validated digital oscillometric device (WatchBP Office, Microlife).

Figure. 5.1: (a) Complete alpha-prototype of Merkfree, (b) Technical comparison of Merkfree asainst MS through a T-connector joint. (c) Merkfree undergoing clinical trial at DMC&H Ludhiana.

(A) Technical validation study protocol

To check the technical accuracy of pressure readings of Merkfree, we compared Merkfree pressure readings against pressure readings of MS by connecting them to each other. For this, the air tube from cuff was split into

two using a T-connector, one tube goes to MS and the other to Merkfree, ensuring equal pressure build up in both devices as shown in Figure. 5.1 (b).

(B) Clinical study protocol

There were two teams appointed to measure BP. Each team had three members assigned to take readings. A 10-minute time interval was given for every successive measurement from the same subject. Separate sheets were provided to each medical staff to avoid any correlation or bias due to the previously taken readings. The measurement order was first by MS followed by Merkfree and digital oscillometric device

5.4 Results

(A) Results from technical validations

In this Merkfree & MS, were compared with each other directly through a T-connector joint. We took the data spanning wide pressures ranging from 50 mmHg to 150 mmHg. Results are presented in Figure.5.2 (a). The pressure readings from two sphygmomanometers are almost equal, with a correlation value of 0.9999. The Bland–Altman plot, reports the bias value of 0 mmHg with standard deviation (SD) of mere 0.67 mmHg, among the two values. All the pressure readings are well inside the upper (1.3067) and lower (-1.3067) limit-of-agreement (LOA) (bias $\pm$ 1.96xSD), as clear from Figure.5.2 (b). Moreover, the maximum difference between the readings of the two sphygmomanometers is a mere 1mmHg, which may be attributed to parallax or human errors associated with BP measurements. Both sphygmomanometers have least count of 1mmHg, rendering the differences depicted here negligible.
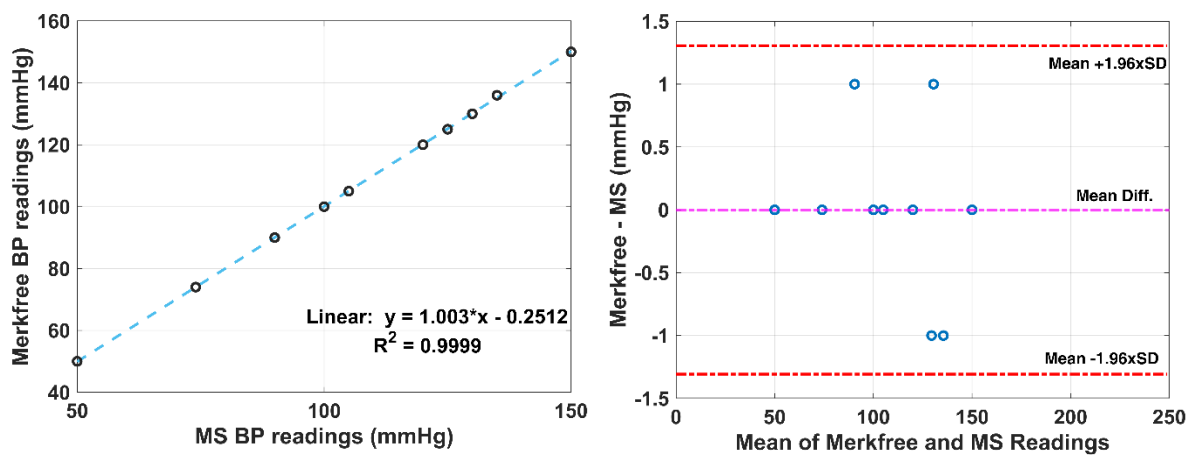
Figure.5.2. Comparison of pressure readings of Merkfree and Mercury sphygmomanometer. (a) The corresponding correlation values, (b) Bland Altman's plot.

(B) Clinical comparison of Merkfree & MS.

We have compared Merkfree with MS because Mercury type is the gold standard of BP measurement. For demonstrating accuracy of any new proposed BP measurement device, it is preferrable to compare it against the MS. The BP measurements done using Merkfree and MS have a coefficient of determination (R^2) of 0.6399 for SBP and 0.4264 for DBP measurements; shown in Figure. 5.3 (a) and 5.3 (b), respectively. The corresponding p-values of the correlation factor for SBP is 0.0216 and 0.115 for DBP. Bland–Altman's analysis comparing Merkfree, and MS reveals that BP measurements have a bias of 1.528 mmHg with SD value of 10.49 mmHg for SBP Figure.5.3 (c), and 0.916 mmHg with SD of 9.112 mmHg for DBP measurements Figure.5.3 (d). The upper and lower limits of agreement (LOA) were calculated to be 22.09 mmHg and -19.03 mmHg for SBP, and 18.78 mmHg and -16.94 mmHg for DBP, respectively. Additionally, the mean absolute percentage error between the measurements from two sphygmomanometers is computed to be 6.22% for SBP and 8.6433% for DBP measurements.
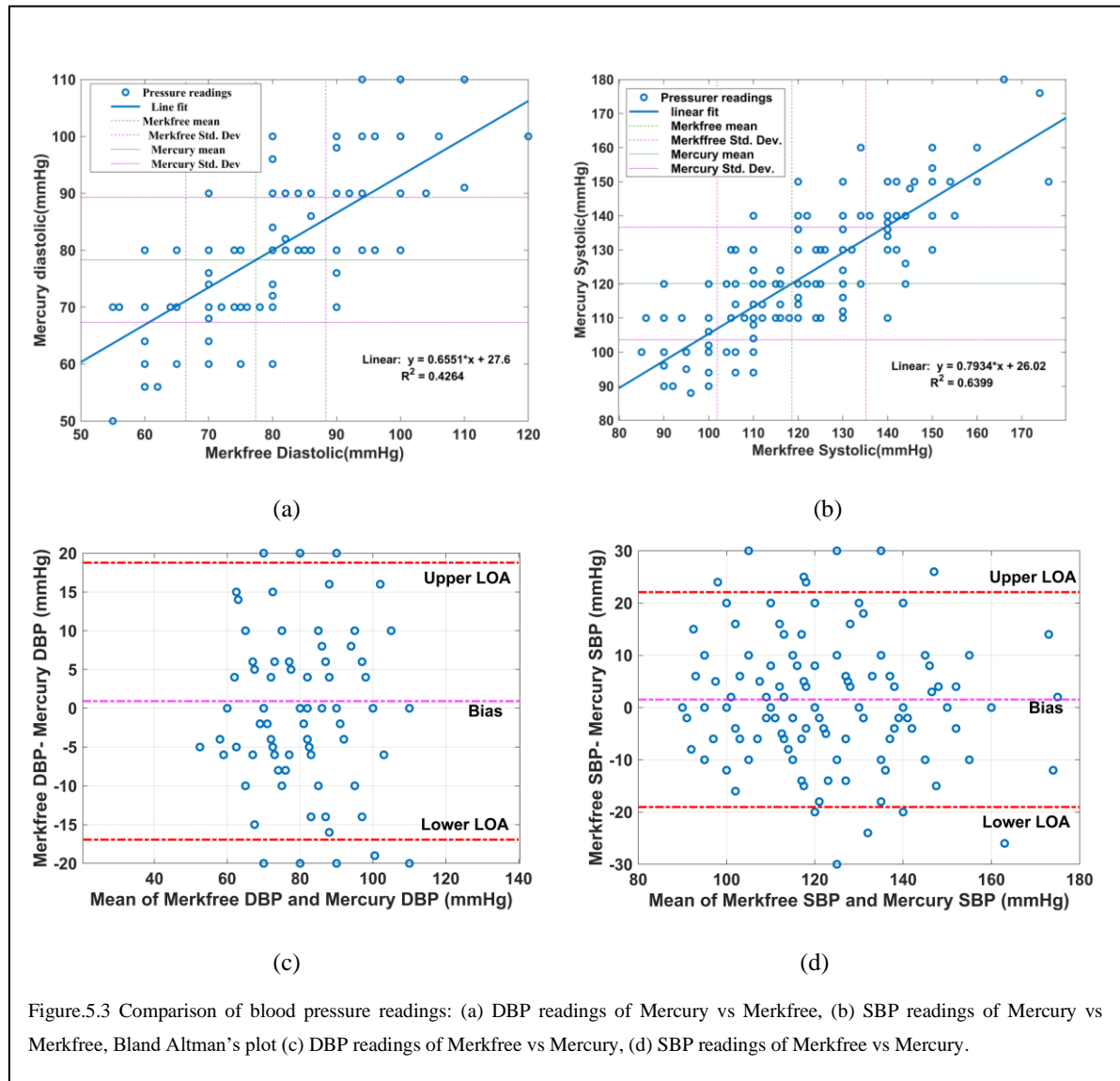
Figure.5.3 Comparison of blood pressure readings: (a) DBP readings of Mercury vs Merkfree, (b) SBP readings of Mercury vs Merkfree, Bland Altman's plot (c) DBP readings of Merkfree vs Mercury, (d) SBP readings of Merkfree vs Mercury.

(C) Clinical comparison of OS & MS.

We have compared OS with MS because there are many studies that already exist comparing MS and OS. The accuracy study is relatively redundant but has been provided for the sake of completeness. However, this study established the baseline accuracy of MS with respect to OS and while comparing OS and Merkfree we show that

Merkfree has higher accuracy with respect to MS as compared to OS. To understand the level of agreement between MS and OS, a comparison analysis was done. The BP measurements correlate with a R^2 value of 0.6083 for SBP and 0.3473 for DBP measurements, as shown in Figure.5.4 (a, b), respectively. Bland–Altman's analysis shows that bias between the readings taken using these two sphygmomanometers is -1.563 mmHg with SD value of 10.85 mmHg for SBP Figure.5.4 (c) and 2.401 mmHg with SD of 9.753 mmHg for DBP measurements Figure.5.4 (d). The upper and lower LOA were computed to be 19.69 mmHg and -22.82 mmHg for SBP and 21.52 mmHg and -16.71mmHg for DBP, respectively. In addition, the mean absolute percentage error between the measurements from two sphygmomanometers is computed to be 6.72% for SBP and 9.84% for DBP measurements.

(a)   (b)

(c)   (d)

Figure.5.4 Comparison of blood pressure readings: (a) DBP readings of Mercury vs Oscillometric (b) SBP readings of Mercury vs Oscillometric, Bland Altman's plot (c) DBP readings of Oscillometric vs Mercury, (d) SBP readings of Oscillometric vs Mercury.
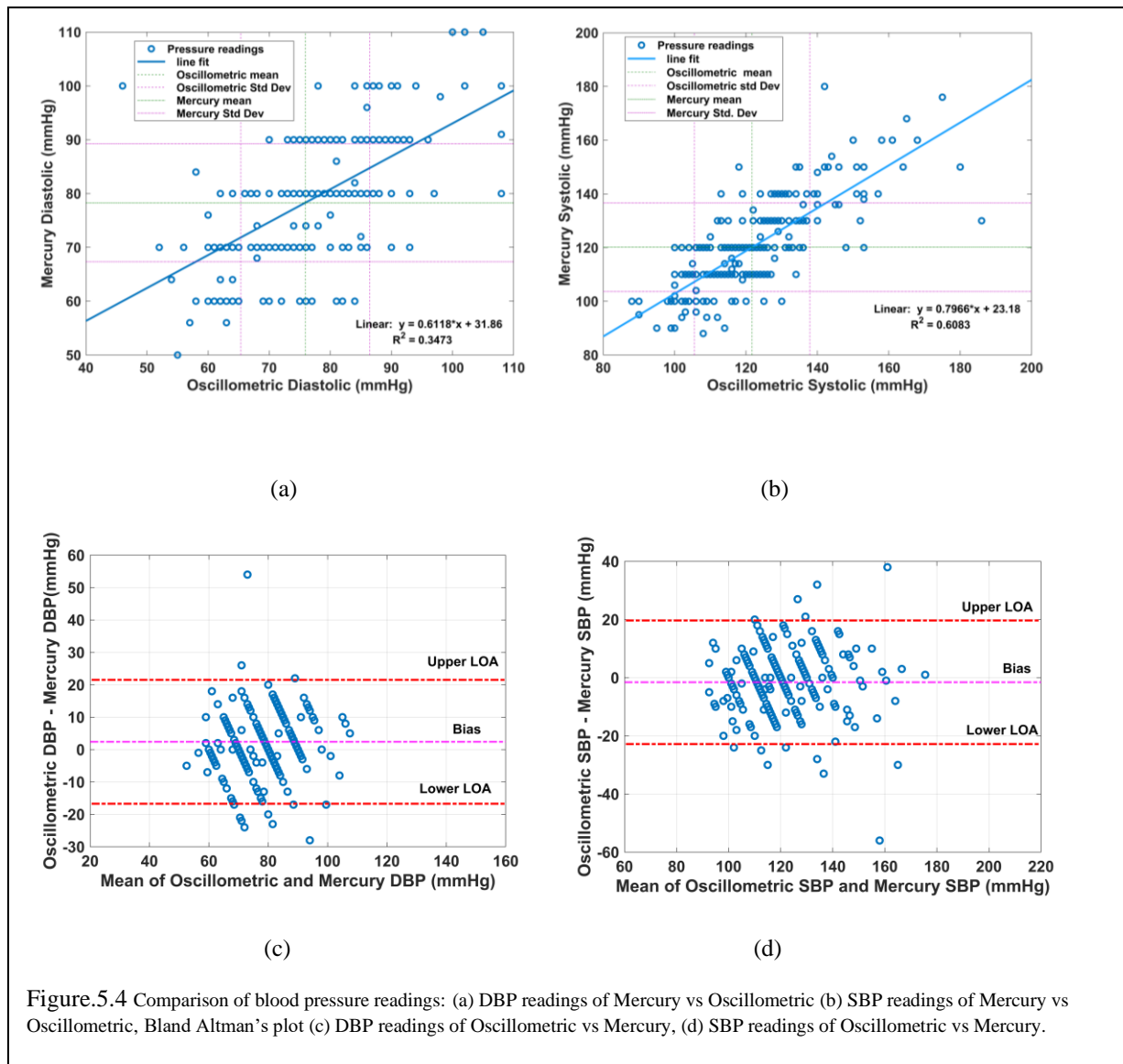
(D) Clinical comparison of Merkfree & OS.

We have compared the Merkfree with OS towards characterization of rounding off errors which has very little quantitative studies in literature. OS is the most widely used device for BP measurement in homes. It has lower accuracy than MS but has no rounding error due to lack of human intervention. Hence, comparative study with it helped us to characterize the rounding errors in MS as well as Merkfree. Finally, a comparison of readings from Merkfree and OS was performed. The R^2 for SBP and DBP were 0.62 and 0.41 as shown in Figure.5.5 (a, b), respectively. Bland–Altman's analysis shows that bias between the readings taken using these two sphygmomanometers is -3.091 mmHg with SD value of 10.68 mmHg for SBP Figure.5.5 (d) and 1.484 mmHg with SD of 9.034 mmHg for DBP measurements Figure.5.5 (c). The upper and lower LOA were computed to be 17.85 mmHg and -24.03 mmHg for SBP and 19.19 mmHg and -16.22 mmHg for DBP, respectively. The mean absolute percentage error between measurements from two sphygmomanometers is 7.015% for SBP and 8.94% for DBP measurements.

Figure.5.5 Comparison of blood pressure readings: (a) DBP readings of Oscillometric vs Merkfree, (b) SBP readings of Oscillometric vs Merkfree, Bland Altman's plot (c) DBP readings of Merkfree vs Oscillometric, (d) SBP readings of Merkfree vs Oscillometric.
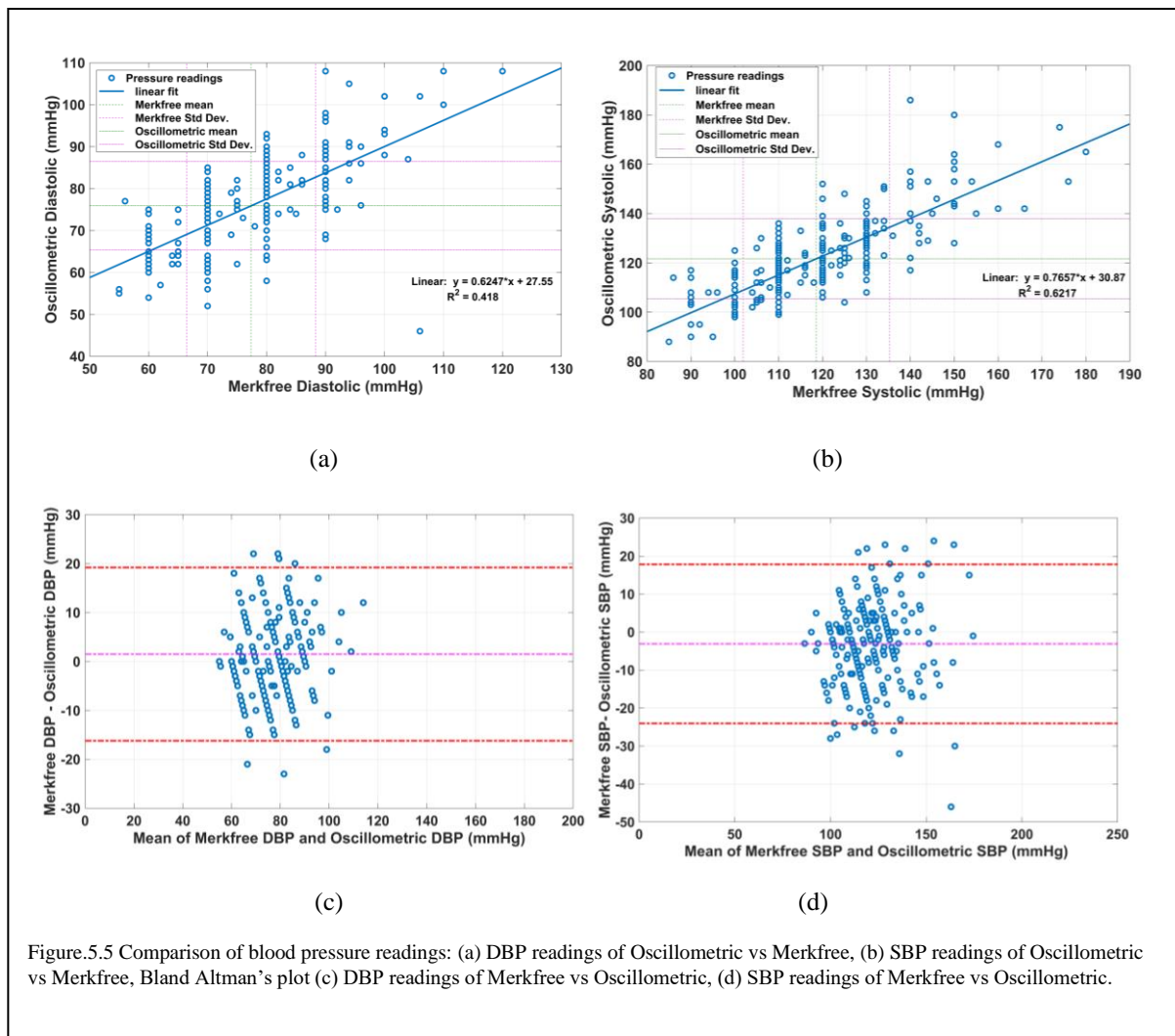
Table 5.1. Kl divergence between ideal and actual distribution of readings for sbp and dbp of all three devices

Column Name	KL-Divergence Value
MS SBP	0.4088
MS DBP	0.4756
Merkfree SBP	0.1991
Merkfree DBP	0.2581
OS SBP	0.0848
OS DBP	0.0423
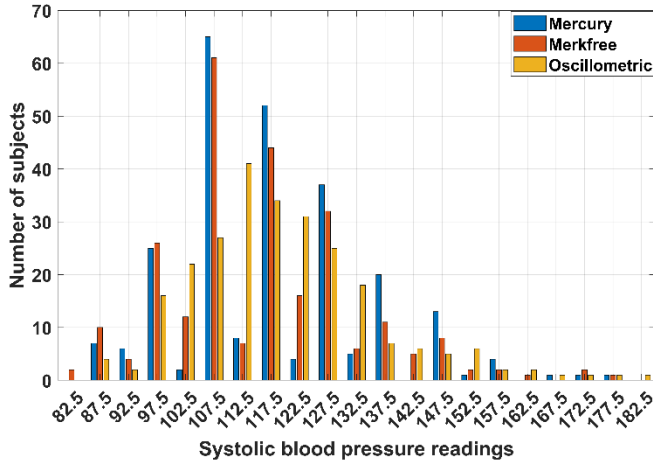
(a)
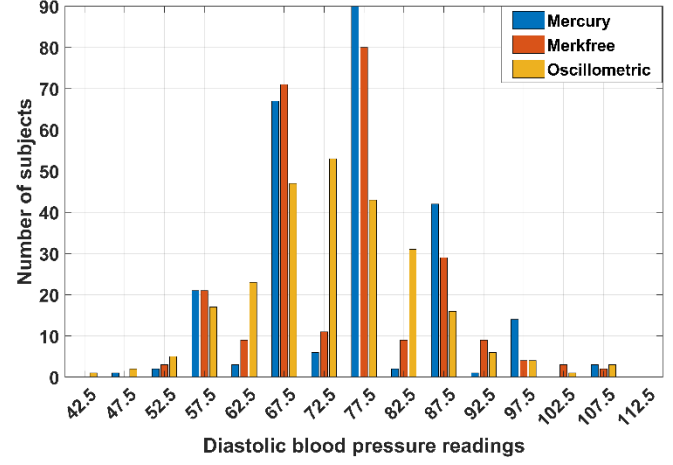
(b)
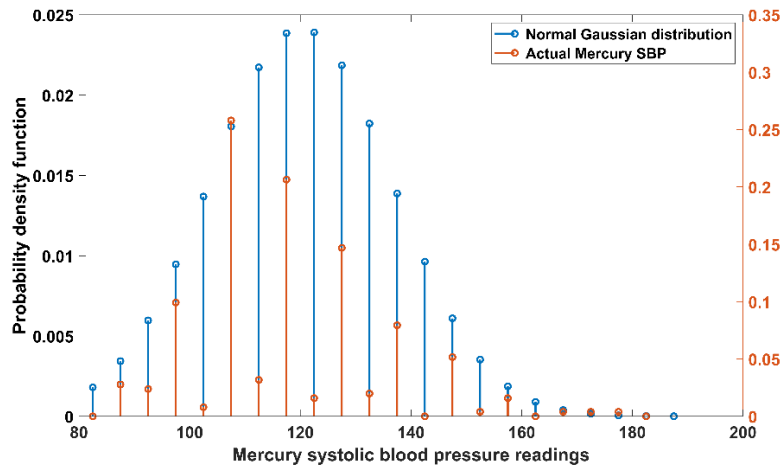
(c)

Figure.5.6 (a) Histogram plot of three devices for SBP, (b) Histogram plot of three devices for DBP, (c) A plot showing normalized ideal expected gaussian distribution plotted over frequency distribution obtained clinical study for the particular case of MS SBP. These two series are used to obtain the KL divergence for MS SBP. Similar series is obtained for all other measurements and to ultimately obtain the values in Table 5.1.

5.5 Discussion

BP measurements using the proposed Merkfree sphygmomanometer has good agreement with commonly used MS and OS. Assuming that MS readings are the true readings of BP, in terms of percentage error, Merkfree readings have lower error compared to OS readings for both SBP and DBP. Merkfree readings also have a higher correlation with MS as compared to correlation obtained between OS and MS. Merkree SBP has lower agreement with OS SBP than MS SBP. Interestingly, this reverses in case of DBP, and Merkfree DBP has higher an agreement with OS SBP than MS SBP.

Merkfree shows comparable performance with respect to the gold standard MS during direct one-to-one comparison of pressure readings in technical validation using a T-connector joint. The Merkfree has a 0.9999 correlation factor with MS in one-to-one direct comparison in technical validation. The bland Altman's analysis also reveals that bias is zero, which corresponds to the zero-measurement error, all data points lie within the limit of agreements and shows the good agreement between pressure readings of two devices. However, the same results were not reproduced during clinical trials, which can also be associated with the accumulation of various errors, such as hearing and concentration variation among individuals while measuring BP, white coat hypertension, and patient anxiety [56].

Bar graphs for SBP and DBP for both all three devices were plotted by taking a frequency interval of 5 Figure.5.6 (a, b). A bar at x represents the number of readings lying between x-2.5 to x+2.5, where x is the multiple of five. Three bars are bunched together at every multiple of 5 for a side-by-side comparison of distribution of readings from all three devices. All three devices show a broad normal distribution which is expected for a random population study like this. It is well known that MS suffers from rounding-off errors due to operator bias towards rounding the readings to the nearest multiple of 10 [173]. This specifically happens as the mercury sphygmomanometers scale has major calibration tick marks at multiples of 10. This can be clearly visualized by comparing at the histogram bar heights at multiples of 10 and multiples of 5 in Figure.5.6 (a) and Figure.5.6 (b). We can see that frequency of readings are in general higher at multiples of 10 than at multiples of 5. In case of Merkfree, we have a longer scale and calibration marks at multiples of 5. Hence, we see that the bias towards rounding off to nearest multiple of 10 is reduced and we have comparable heights of frequency bars even at multiples of 5. OS type doesn't have rounding-off error at all because human in the loop is eliminated. Distribution of the yellow bars in Figure.5.6 (a) and Figure.5.6 (b) demonstrate this quite clearly. To quantify the extent of the mismatch in the distribution with respect to the expected normal distribution, we created the theoretically expected distribution and calculated its KL divergence with respect to the expected distribution. We have SBP and DBP data for all three devices which are 6 variables in total. For each variable X, we found the mean and standard deviation. An ideal gaussian distribution was calculated for MS SBP Fig. 7(c) using just the mean and the standard deviation. This distribution was then sampled at multiples of 5 starting from 85 mmHg to 195 mmHg for SBP; and from 45 mmHg to 125 mmHg for DBP. These ranges cover all readings starting from lowest to the highest in all columns. KL Divergence was then calculated between this distribution and the actual distribution for all 6 variables. The results are listed in Table 5.1. Here we can see that MS has the highest KL divergence while OS has lowest indicated that MS have highest deviation from Normal distribution, primarily owing to rounding-off errors while OS has no rounding-off errors. Merkfree while maintaining better accuracy than OS, is also having lower rounding-off error compared to MS. This is apparent from the intermediate KL divergence values.

Most developed countries have already banned the MS, and most developing countries are in the process of doing so [53]. Merkfree is likely to be widely applicable and acceptable in these changed circumstances where MSs are discouraged. Digital BP measuring devices are independent of the operator, but their accuracy and repeatability have been questionable due to variability in proprietary software algorithms from company to company. As per the study conducted by us recently among Indian Clinicians [19], it was found that digital BP measuring devices are considered inferior in accuracy and robustness compared to auscultatory BP monitors by most respondents. Owing to auscultatory method and longer measurement scale, Merkfree is expected to have limited use in home monitoring of BP. However, it is expected to have wide acceptance for clinical measurement of BP.

5.6 Conclusion

We have designed a mercury-free sphygmomanometer – Merkfree, with the same structure and principle of operation as a MS. Merkfree aims at being very close to the MS while getting rid of the mercury. Merkfree will help in achieving the goal of the Minamata convention of WHO by promoting elimination of Mercury based sphygmomanometers. Merkfree measures BP using same principle of auscultation as that of MS and was demonstrated to have less than 10% error with respect to MS for both SBP and DBP. Key innovation in Merkfree is the use of Galinstan instead of Mercury. Galinstan has a lower density compared to Mercury hence, Merkfree has a longer scale height. However, this improves visibility and reduces rounding-off errors. The stickiness of Galinstan with glass had been a major impediment in the development of a BP monitor using it. This has been eliminated by developing an innovative technique of maintaining a small meniscus of a reducing agent in the measurement column. In this paper, we elucidated the different components of Merkfree device and conducted its clinical trials on 252 patients with respect to MS and OS.

Chapter-6: Exploration of a new method of cuffless blood pressure measurement using acoustic radiation force impulse (ARFI)
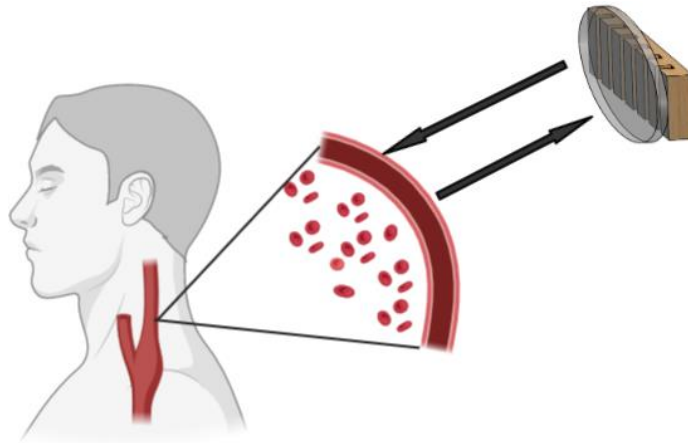
6.1 Introduction

Blood Pressure (BP) is one of the vital parameters that is often measured during hospital visits. Heart disease is a leading cause of death worldwide, and hypertension, or high blood pressure, is a leading risk factor for heart disease [19]. The four primary vital signs of the human body are pulse rate, respiration rate, temperature, and BP. While there are many wearable devices that can track pulse rate, respiration rate, and temperature discreetly and continuously without disturbing the patient, this is not yet possible for BP measurement [174]. Currently, BP measurements require cuff-based devices that can only take one-time measurements of systolic and diastolic pressure. This measurement is typically performed at the brachial artery and takes about 10 minutes to complete [175]. Several groups are working on the development of non-invasive, cuffless blood pressure monitoring technologies for fast and accurate BP measurements. These technologies are based on directly measuring physiological parameters without blocking the artery. There are many physiological parameters, but only a few are useful for BP measurement. Two main analysis methods used to measure BP are Pulse Transit Time (PTT) and Pulse Wave Analysis (PWA) [26]. PTT is the time it takes for the arterial pressure wave to travel from the proximal to the distal site. PTT is inversely proportional to blood pressure and depends on inner lumen diameter (ILD), tube diameter (TD), blood density, and tube thickness (TT) [27]. Pulse wave velocity can be calculated from PTT and PWA analysis and is related to BP through the Moens-Kortewegz [28] and Huges [29] equations. Signals from various modalities can be used for these methods, such as photoplethysmography (PPG), electrocardiogram (ECG) [30], microelectromechanical sensing [31], magneto-plethysmography [32], ballistocardiography (BCG) [33], bioimpedance [34], and ultrasound image processing [35]. However, these methods have limited success. Most of these techniques have low accuracy compared to gold standard BP measurements performed with mercury types. Cuffless BP measurement is still an active area of research. Many cuffless BP methods using PTT have shown great promise and relatively good accuracy in the short term [176] . Unfortunately, while these methods are quite accurate in measuring the pulse pressure, the absolute BP drifts due to low frequency drift in BP due to vasomotor tone variation makes can lead to inaccurate systolic [177].

Ultrasound is commonly utilized for non-invasive imaging of tissues. In normal imaging mode operations, plane and focused waves of a few microseconds pulse duration are employed. However, the use of ultrasound in its imaging modality for measuring blood pressure (BP) has had limited success. For instance, Beulen et al. developed an innovative approach to measuring internal pressure by monitoring changes in the ratio of flow and cross-sectional area using ultrasound probes, but it requires a flow sensor to be directly inserted into the system [43]. Zakrzewski et al. used ultrasound imaging to monitor internal pressure by recording changes in the diameter of the tube under the application of external force from the ultrasound probe [44]. However, this method necessitates the continuous application of external loading, which may be uncomfortable and may dislodge plaque in atherosclerotic arteries. Weber et al. proposed a system for measuring blood pressure at the wrist using a balloon inflation system pushing against the radial artery that works like a cuff [45]. A single element ultrasound probe is aimed at the artery, measuring the diameter change of the radial artery and identifying when it is completely blocked by pressure from the inflating balloon. The system is quite bulky and cumbersome for regular use, and radial arterial pressure is not used in most clinical measurements.

Ultrasound in its imaging mode of operation does not have any significant mechanical effects on tissues. However, newer applications of ultrasound technology use focused beams of a few hundred milliseconds duration to cause mechanical force on tissues, known as Acoustic Radiation Force Impulse (ARFI). Applications of ARFI include

creating tissue stiffness maps [178], nerve imaging [179], and monitoring thermal ablation procedures [180]. Typically, stiffness imaging through ARFI involves first sending one imaging pulse to image the original location of the tissue, followed by an ARFI pulse to push the location. Immediately after this, another imaging pulse is sent to locate the tissue shift due to ARFI. By repeating this process over a volume of tissue, a stiffness map can be created [181]. Based on this concept, it is hypothesized that it is possible to push the arterial wall through an ARFI pulse and monitor its impulsive unloading using high-frequency ultrasound imaging immediately following the ARFI pulse. The arterial wall is expected to undergo an unloading process followed by a hoop mode vibration, with the frequency of this vibration being related to its geometric dimensions, mechanical properties, and internal pressure. The difficulty in determining the exact relationship between internal pressure, hoop frequency, and other physical parameters due to the simultaneous dependence of hoop frequency on multiple parameters (IP, ILD, TT, TD, etc.), has led us to attempt to create an empirically derived machine learning (ML) model to measure blood pressure using Acoustic Radiation Force Impulse (ARFI). The model is designed to measure the internal pressure (IP) of any thin-walled pressure vessel by measuring its inner lumen diameter (ILD), tube thickness (TT), density of the material of the tube (TD), and hoop mode frequency (HMF). The proposed BP measurement system, as shown in Figure 6.1, involves sending a planar imaging pulse from an ultrasonic linear array probe. The same transducer will then receive reflected pulses and create an image of the artery in cross-sectional view through standard beam-forming methods [182]. The wall of the artery will be identified using image processing methods, and a focused ARFI pulse of a length of hundreds of microseconds will be aimed at this wall. As the arterial wall is elastic and under pressure, as soon as the ARFI is stopped, the wall will rebound towards its original shape undergoing damped hoop mode oscillations. The artery can be imaged at high frequency during this impulsive unloading process using plane wave imaging at KHz frame rates [183]. By using correlation-based image feature tracking, the hoop mode frequency can be measured. With this model at the core, it will be possible to develop ultrasound-based handheld systems for continuous cuffless BP measurement. To develop such an ML model, a large amount of data is needed from various tubes with different diameters, thickness, elasticity, and density of material held at different internal pressures. However, it is nearly impossible to collect such experimental data, therefore, we used FEM simulation-based eigenfrequency analysis of tubes. We have chosen a parameter range similar to the mechanical and geometrical parameters of the blood vessels. With proper parameter control, our analysis can be extended to analyze all kinds of thin-walled pressure vessels. Eigenfrequency analysis generates many different vibration modes, and we are only interested in hoop mode analysis. To automate the process of hoop mode identification to make data analysis tractable, we developed an image processing pipeline that could identify and segregate hoop mode images from the FEM simulations, automatically pull the physical parameters and hoop mode frequencies from them and store them in a tabular file. This table was then used to develop deep neural networks that are able to predict the internal pressure of the tube with an error of less than 6.5%.
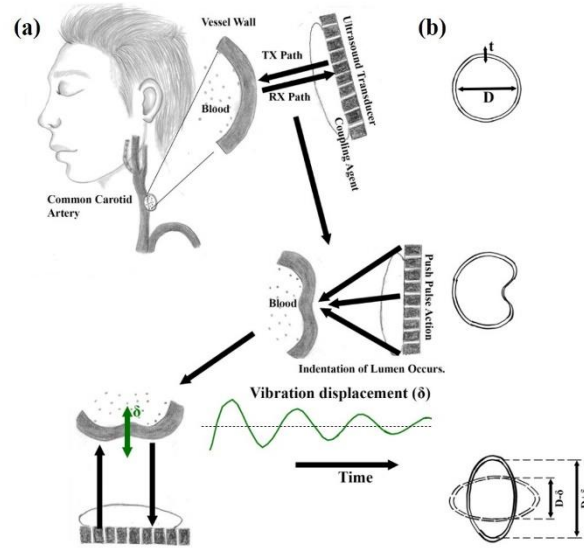
Figure. 6.1. (a) Schematic depicting high frequency ultrasound impingement causing artery deformation. Artery undergoes damped oscillation to attain its original shape, which is monitored via receiving tracking waves. (b) Shape of artery at each stage of cycle
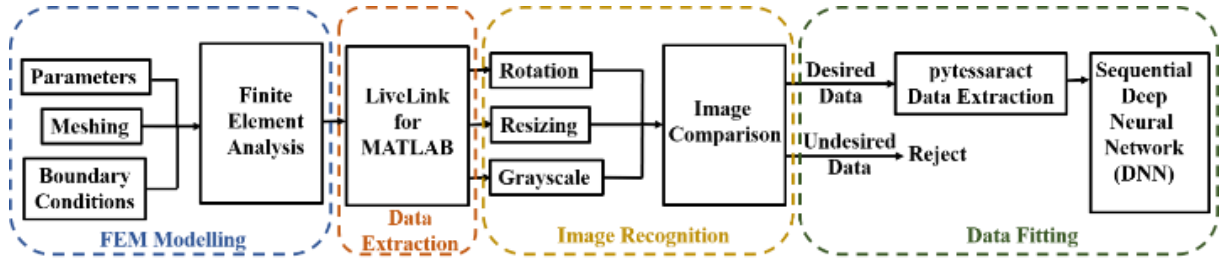
Figure.6. 2. Systematic workflow of model development: Modelling, automated data extraction, data recognition and data fitting.

6.2 Materials and Methods

A.   Simulation and Model Development Workflow

We developed a model to measure blood pressure (BP) using ultrasonically measurable parameters by performing eigenfrequency analysis. We simulated the various eigenmodes excited by an ultrasound probe in a thin-walled pressure tube using the COMSOL Multiphysics package, which is based on finite element analysis. We varied the radius and thickness of a hollow tube of 100 mm length (as shown in Table 6.1) and also the material properties, such as elastic modulus and density, to account for blood vessels of different ages, genders, and health conditions. We used free tetrahedral meshing, resulting in an average of 13,284 domain elements, 8,928 boundary elements, and 872 edge elements. For boundary conditions, we held the free end of the tube fixed and applied internal pressure on the internal faces of the hollow tube, while leaving the outer faces free to allow for free deformation of the tube. We performed FEA over the parametric range in two steps: first, we used a stationary solver to determine the deformation of the tube under variable loading, which allowed us to determine the change in diameter due to internal pressure. Secondly, we performed eigenfrequency analysis to determine the various resonant modes of the blood vessel subjected to variable internal pressures. We performed the numerical analysis under default solver settings using the MUMPS solver with a pivot threshold value of 0.1. In total, we performed

60

58,313 simulations, each containing 80 eigenmode images. Analyzing such a large dataset was only practical using automated algorithms, therefore, we extracted all the data to MATLAB using COMSOL Livelink. The overall workflow from simulation to ML model development is shown in Figure.6. 2.

Table.6.1 Geometric and Mechanical Parameters of Tube for Numerical Analysis

Parameter	Values
Inner Lumen Diameter [184]*	(4, 4.4, 4.8, 5.2, 5.6 and 6) mm
Tube Thickness [185]*	(0.2, 0.22, 0.24, 0.26, 0.28 and 0.3) mm
Internal Pressure	(60, 70, 80, 90, 100, 110, 120, 130, 140, 150) mmHg
Tube Density [186]*	(1110, 1130, 1150, 1170, 1190, 1210) kgm^{-3}
Elastic Modulus [187]*	(1000, 1100, 1150, 1250, 1300, 1400) kPa
Tube Length	100 mm
Poisson's Ratio	0.49

B. *Finding of hoop mode frequency*

The COMSOL simulation generates various eigenmodes on the tube and presents the results in the form of images with embedded text headers. The text and image sections are then separated, and the image is processed using the structural similarity index (SSIM) to identify the hoop mode among all the eigenmodes (Figure.6.3). This process is explained in more detail in our recent conference paper [188]. The text section is then processed using OCR with the pytesseract package to extract the frequency value of the hoop mode with high accuracy (>99%). However, there may be some inaccuracies in the dataset due to incorrect detection of text in the hoop mode image by pytesseract. These inaccuracies can be easily identified and removed through a threshold-based outlier detection process.

tube_Thickness=4E-4, tube_Radius=0.002, internal_Pressure=10666 Eigenfrequency=715.67
Surface: Total displacement (m)
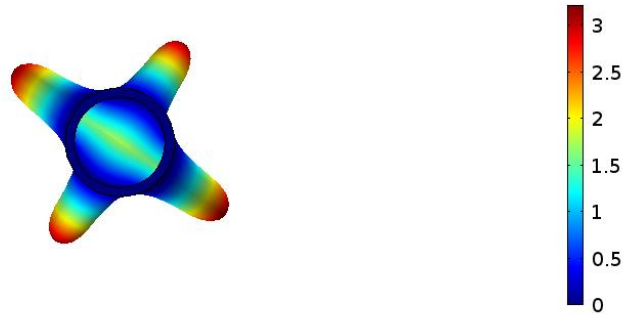
(a)
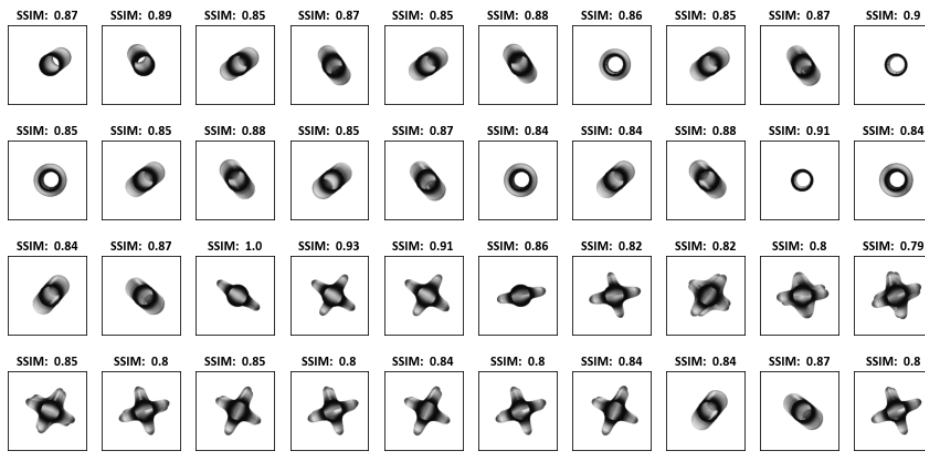
(b)

Figure.6 3. (a) A typical eigen mode image along with text containing the. Eigen frequency embedded in the image. This text was run through OCR to read the frequency values. (b) The hoop mode reference image is compared with all eigen modes obtained in simulation to identify the image corresponding to hoop mode (Only a subset of the 80 eigen modes are shown).

C. *Machine learning model*

We utilized deep neural networks to find an optimal model that can predict internal pressure (IP) when given the tube thickness (TT), density of the material of the tube, inner lumen diameter (ILD), and hoop mode frequencies (HMF). To do this, we organized the simulation-generated dataset into five columns. The first four columns were the inputs (ILD, TT, TD, and HMF) and the fifth column was the target variable (IP) to be predicted. The dataset consisted of 54966 rows which were randomly shuffled and split into 80% for training and 20% for testing.

1. *Normalization*

After that the data in the input columns were normalized by subtracting the mean and dividing by the standard deviation of the corresponding column.

2. ML model development

We created two different machine learning models to estimate internal pressure using simulated input parameters. The first model utilized all four input parameters as listed in Table 6.2. While the tube thickness (TT), inner lumen diameter (ILD), and hoop mode frequencies (HMF) can be measured using ultrasound methodology, the density of the material is not measurable. We believe that the density of human tissue falls within a relatively narrow range (1100-1200 Kg/m3) [186] and is unlikely to impact the accuracy of the model. However, this is a limitation of the first model, so we developed a second model without the density parameter and the performance of the model did not significantly decrease as expected.

Table. 6.2. Mean and Standard Deviations of Different Parameters in the Dataset

Parameters	Mean	Standard Deviation
Tube Thickness (mm)	0.4546	0.135
Diameter (mm)	5.3	0.748
Hoop Mode Frequency (Hz)	548.37	100.5
Density (Kg/m^3)	1159.84	33.76
Internal Pressure (Pa)	14096.72	3370.2

3. Hyperparameter Tuning

Both models are deep neural networks that were developed by searching through a range of parameters using the following general approach. We attempted to find a model with 2 to 4 hidden layers, where the number of units in each layer could be one of four values: 5, 10, 20, or 25. The activation functions for the hidden layers could be either 'relu' or 'tanh'. Batch normalization and dropout regularization were applied between these layers, with the dropout percentage varying randomly between 0 and 50%. Since we were only building a regression model to predict internal pressure, the output layer was always set to a single unit with a 'relu' activation. We used two optimizers, 'adam' and 'adagrad', and optimized the model to achieve the minimum mean absolute percentage error. The parameter space was searched using the Keras Tuner package [189]. Each parameter combination was tried for a minimum of five epochs. If the loss failed to reduce within these epochs, the current combination was abandoned, and the Tuner moved on to try the next set of parameters.

4. Optimized four input model.

An optimized model was obtained using the same hyperparameter optimization process as described in the previous section, which utilizes four input parameters: TT, ILD, HMF, and TD. The architecture of this model includes one input layer, two hidden layers and one output layer. The first hidden layer has 25 units, and the second hidden layer has 10 units. The activation function used for all layers is 'relu'.

5. *Optimized three input model*

To verify our hypothesis that the density of the wall has little impact on the model, we conducted a shapely feature analysis using SHAP (Shapley Additive Explanations). SHAP is a tool that allows for the visualization of the output of a machine learning model by computing the contribution of each feature. The results of the SHAP analysis are discussed in the results sub-section D. From the results, it was clear that the density plays a minimal role in the accuracy of the model. Therefore, we explored a three-parameter model by eliminating the density parameter. The architecture of this model is described in Table 6.3.

Table.6.3. DNN Architecture of Three Input Parameters for Internal Pressure Measurement.

Layer type	Layer shape (Rows, columns)	Parameters	Activations
Input Vector	(4,1) *	-	-
First hidden layer	(5,1)	25	Relu
Second hidden layer	(25,1)	150	Relu
Third hidden layer	(10,1)	260	Relu
Output	(1, 1)	11	Relu
*Input vector is 4x1 for 3 input parameters as first parameter is a constant in neural networks.			

D. *Verification of concept*

We have tested this workflow using a phantom of a latex tube suspended in a muscle mimicking gelatin [190]. The ARFI and imaging sequences were generated using a Verasonics Vantage 128 Research Ultrasound System. A complete control software package was created in MATLAB, which allows for imaging the phantom, aiming the ARFI at the tube wall, obtaining the fast ultrasound image sequences of hoop mode vibration and tracking the opposite walls of the tube. The Fourier analysis of the hoop mode vibration was performed to obtain the dominant frequencies. The hoop mode frequency is also

easily distinguishable from other frequencies for thin-walled tubes. For thin-walled pressure tubes ($r \gg t$), hoop stress is considerably larger than radial stress, causing a sharp rise in the vibration amplitude at a particular hoop frequency. Higher vibration modes are also present, but their intensity is exponentially attenuated in comparison to the hoop modes. Therefore, higher modes were ignored for our analysis. Hoop stress is strongly dependent on the internal pressure of thin-walled pressure vessels. Thus, hoop frequency is also strongly influenced by the internal pressure of the tube along with other material parameters. By directly correlating material parameters such as tube radius, thickness, and density of the material with the hoop frequency, internal pressure inside the tube can be accurately determined. A similar workflow can also be implemented for any other use case of non-intrusive pressure measurement in thin-walled vessels.

E. *Experimental verification of model performance*

To test the model's performance in experiments that closely mimic an artery in muscle tissue, we created arterial phantoms and insonated them using focused ARFI beams generated by a Verasonics Vantage 128 Research Ultrasound System. The hoop mode frequencies were captured using high-frequency ultrasound imaging, and the arterial walls were analyzed to determine the hoop mode frequencies.

1. *Phantom preparation*

The phantoms were created by using long tubes made of different types of materials with elastic modulus similar to that of human arteries. These tubes were suspended in two different substrates, water and 2% gelatin, within rectangular containers. The tubes were equipped with input and output ports connected to three-way luer locks, allowing for the pumping of water in and out of the tubes. An A-line pressure catheter (from Millar Corporation, Texas, USA) was placed at the center of the tube through one of the input ports. A plastic eye dropper was also connected through another channel of the input stopcocks with luer lock connectors. Water was filled within the tube, and the output port was locked. The pressure inside the tube could be varied by pressing and releasing the dropper alternatively.

2. *Ultrasound investigation*

We used the Verasonics Vantage 128 Research Ultrasound System to create imaging and ARFI sequences using the Philips L7-4 probe. To both push the wall of the phantom and capture its vibrations after the release of the push, a complete software package was created in MATLAB®. This software allows the operator to specify different ARFI parameters such as the position of the focal point, duration of the push pulse, and voltage of the push pulses (Figure.6.4). The operator can also specify the time points at which imaging pulses should be delivered. The typical sequence of events is as follows:

1. The phantom is placed in position.
2. Tube is visualized in transverse mode.
3. The focal point is set at the proximal wall of the tube.
4. The baseline image is recorded through a planar imaging pulse.
5. A one millisecond ARFI pulse is delivered at the focal point.

6. Immediately afterwards, a sequence of 40 image pulses were fired with a time gap of about 150 us each.

7. The diameter and thickness were measured from the baseline image.

8. The proximal and distal walls were tracked on the 40 images, and their distention waveform during vibration was plotted.

9. The hoop mode frequency was calculated by using Fourier analysis of the distention waveform.

10. The pressure within the tube was changed by pressing the eye dropper, and steps were repeated starting from step number 4.

(a)

(b)

(c)

(d)

(e)

(f)

(g)
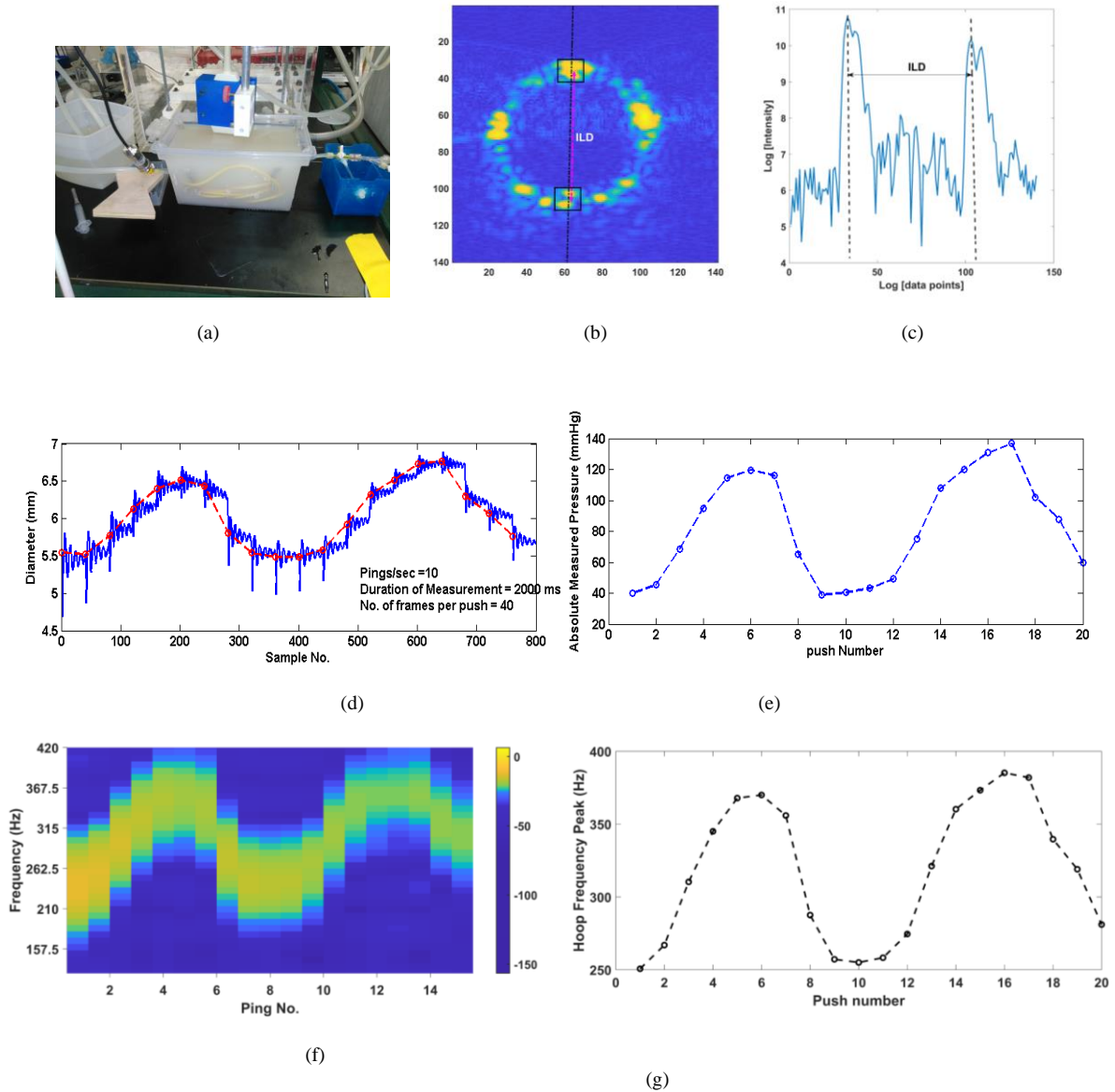
Fig. 6.4. Experimental setup demonstrating the hypothesis that hoop mode frequency is dependent on internal pressure of a tube and it is possible to obtain the vibrations in tube diameter after an ARFI push pulse. (a) A gelatin phantom was made with a latex tube embedded in it. A linear array ultrasound probe is used to create both the ARFI pulse sequence and the subsequent imaging sequence. (b) An image of the tube in the transverse mode plotted in heat a map colour scheme (c) Plot of a single line of data (in log scale) as marked with a dotted line in Fig.4 (b). ILD is approximately equal to the distance of two peaks. The special units in both Fig.4 (b) and (c) are in multiple of half-wavelengths. (d) 10 ARFI pulses are created every second while simultaneously pressure within the tube is taken through a range. After each push pulse the walls are tracked, and diameter waveform is plotted. The hoop mode vibrations are apparent on the measurements and a monotonically increasing relationship between frequency and internal pressure can be visualized, (e) Absolute measured pressure vs push number,(f) Shows a spectrogram of the diameter vibration curve shown in Fig 5 (d) with a window size of 40 and overlap of 0, (g) Shows the peaks of the frequency as identified in each window of the spectrogram. From this it can be observed clearly that changes in IP leads to corresponding changes in the HMF.

66

3. Fourier analysis

Two rectangular kernels placed at the proximal and distal apex of the tube were tracked using a correlation-based method, and a diameter distention waveform was obtained after every push. This 40-point distention sequence captured the hoop mode vibrations of the tube. This sequence was interpolated 100 times and an FFT was obtained. The peak of this FFT sequence corresponds to the dominant hoop mode frequency.

The diameter was calculated by measuring the distance of the two apex points through peak detection applied on the data line passing through the center of the tube. The thickness of the tube can be obtained using similar image analysis. However, for the purpose of simplifying this experiment, we assumed that the thickness does not change with pressure, and we measured it using a vernier caliper before starting the experiment.

The diameter variations for one experiment are shown in Figure. 6.4 (f). 20 push pulses were given within 2 seconds. A spectrogram of the whole sequence was obtained with a window size of 40 and overlap of 0 points. From the spectrogram, the dominant frequency variation with respect to pressure changes in the tube can be clearly visualized.

6.3 Results and discussion

A. COMSOL simulation results

An elastic model of the tube was designed in COMSOL using various parameters as shown in Table 1. The dependence of hoop frequency on different mechanical and geometrical parameters was studied by plotting HMF against one parameter at a time while keeping all other parameters fixed. In the simulation of eigen frequencies, various frequency modes are obtained, but the one of interest is the hoop mode, as shown in Figure.6.5(a). In Figure.6.5(b), we swept the IP within the tube between 60 and 150 mmHg while keeping other parameters such as tube TD, Young's modulus (E), TT, ILD, and Poisson's ratio fixed. There is a non-linear relationship between HMF and IP, but both are positively proportional to each other. The equation of the relationship between HMF and IP is shown in Figure.6.5 (b) an almost linear fit shows the strong correlation of hoop mode frequency with the internal pressure of the tube. Figure.6 5 (c) and 6.5 (d) shows that HMF has an inverse non-linear relationship with TT and ID respectively. Figure.6.5 (g) shows that HMF has a positive linear relationship with E. It is intuitive to think that E should play a linking role between pressure and diameter, hence a method like ours that tries to determine the IP from dynamic variations in ID of the artery should need E. However, we hypothesize that as E and HMF have a direct linear relationship, the information regarding E is contained in the HMF, and hence the ML model for IP determination developed by us will be able to model this information. Figure.6. 5 (e) shows that HM has a small negative linear relationship with TD. Later in Section III (*C*), we show that tissue density does not contribute significantly to our model and can be eliminated.

Figure.6.5 (f) and 5 (h) show that there is nearly no effect of Poisson's ratio and tube length on HMF and hence we did not consider them in any of our ML model design.
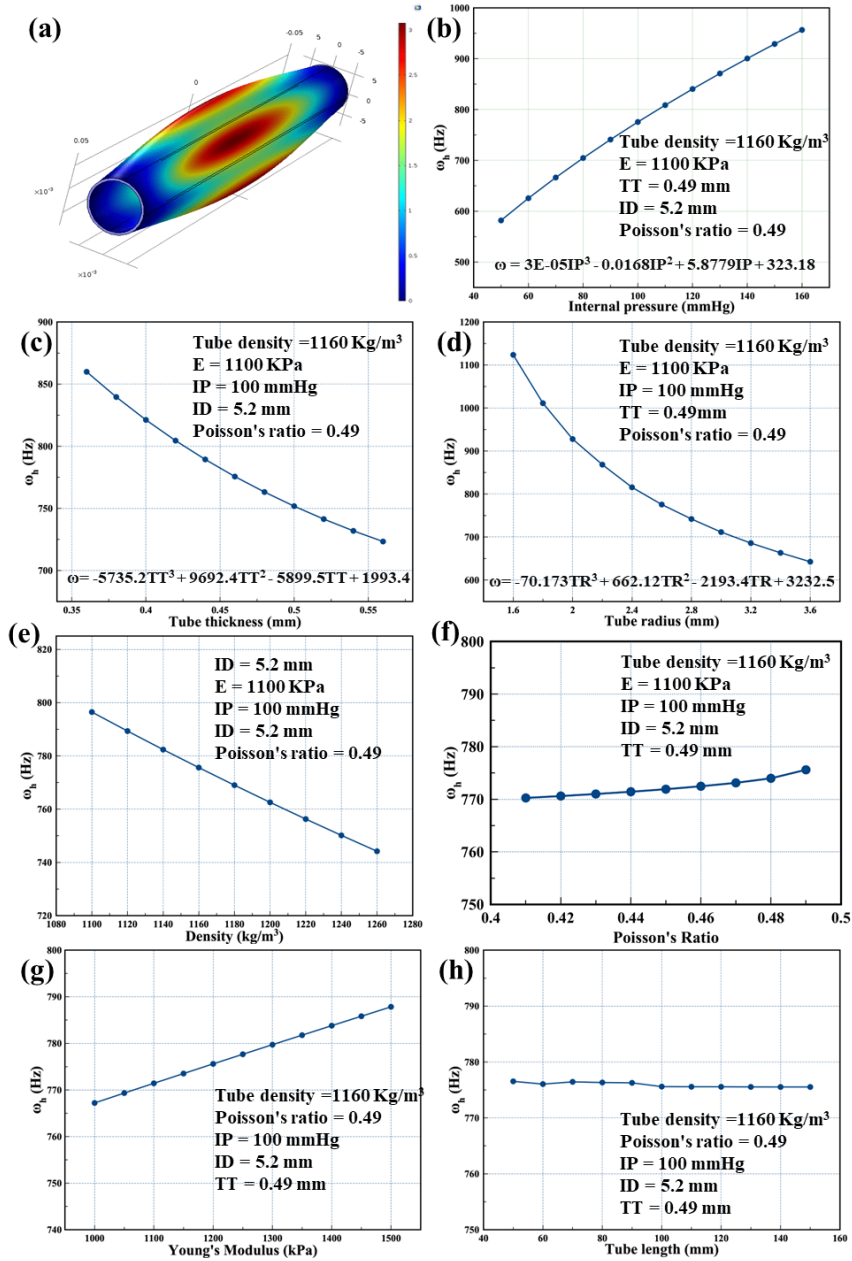
Figure. 6.5. Dependence of hoop frequency on various parameters.

B. *Accuracy of the four-parameter model*

A sequential DNN model was trained using Table 6.4 to predict the internal pressure (IP) of a material based on four input parameters: HMF, TT, ILD, and TD. The trained model had a mean absolute error of 5.45% on the training data and 5.63% on the testing data. The Bland-Altman analysis revealed a bias of -0.29 mmHg, an SD of 11.42 mmHg, and upper and lower limits of agreement of 22.09 mmHg and -22.67 mmHg, as shown in Figure. 6.6 (a). The regression plot in Figure. 6.6 (b) indicated that readings with actual values below 100 mmHg tend to be overestimated and readings above 100 mmHg tend to be underestimated, which resulted in the rhombus-like structure seen in the Bland-Altman plot. To estimate

the number of readings needed to achieve a precision of margin of error less than 10 mmHg, standard deviations of the differences between actual and predicted values were calculated for all readings with actual values between 95 and 100 mmHg, as this range had the highest SD in the Bland-Altman plot. For the FPM, the SD in this range was found to be 7.423, and the number of readings required to achieve a precision of margin error less than 10 was calculated to be 6. The coefficient of determination (R2) between predicted and actual IP measurements of the test data was found to be 0.822, as shown in Figure.6.6 (b). The p-value of the paired t-test between the actual and predicted values of the test data was 0.0001, indicating that the model can accurately predict internal pressure for most IP values within the human physiological range.

Table. 6.4 DNN Architecture of Four Input Parameter for Internal Pressure Measurement.

Layer type	Layer shape (Rows, columns)	Parameters	Activations
Input Vector	(5,1) *	-	-
First hidden layer	(5,1)	25	Relu
Second hidden layer	(25,1)	150	Relu
Third hidden layer	(10,1)	260	Relu
Output	(1, 1)	11	Relu
*Input vector is 5x1 for 4 input parameters as first parameter is a constant in neural networks.			

	(a)	(b)
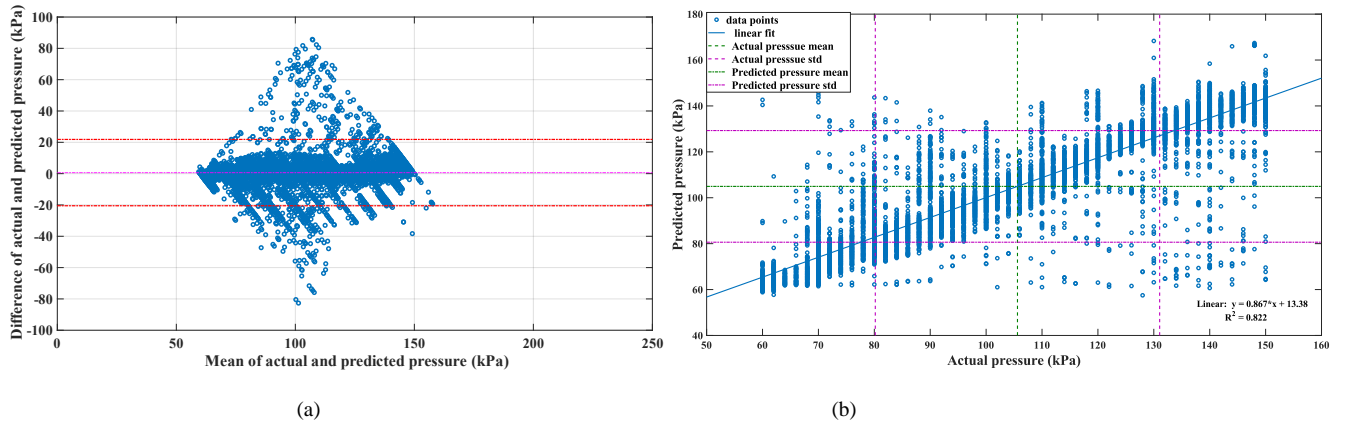
Figure.6.6 (a) Bland Altman plot of actual and predicted pressure with density parameter, (b) Comparison of pressure readings, actual vs predicted with density parameter.
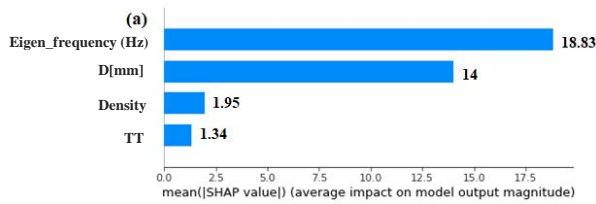
Figure. 6.7. SHAP values for the parameters of the FPM

C. Shape value interpretation

The SHAP (Shapley Additive Explanations) values were calculated for a four-parameter model, as depicted in Figure. 6.7. The results showed that HMF and ID were the primary contributors to the model's output, with SHAP values of 18.83% and 14%, respectively. TD, on the other hand, had a much lower SHAP value of 1.66%. As TD cannot be measured ultrasonically, it was removed from the model without causing a significant loss in accuracy. Therefore, the researchers developed a three-parameter model based on this observation.

D. Accuracy of the three-parameter model

A new DNN model was developed using HMF, ID, and TT as the governing parameters. The model achieved a mean absolute percentage error of 6.6% on the training data and 6.5% on the testing data. Despite neglecting density as a governing parameter, the small drop in prediction accuracy can be attributed to the relatively small dependence of density on hoop frequency compared to the other parameters. The Bland-Altman analysis comparing the predicted and actual internal pressure measurements revealed a bias of 0.17 mmHg and a standard deviation of 10.80 mmHg. The upper and lower limits of agreement (LOA) were calculated to be 21.35 mmHg and -21 mmHg, as shown in Figure. 6.8 (a). The coefficient of determination (R2) between predicted and actual internal pressure

70

measurements was found to be 0.845, as shown in Figure.6.8 (b). The p-value of the paired t-test between the actual and the predicted values of test data was less than 0.0001. For TPM, the standard deviation in the range of 95 to 100 mmHg was 8.086, thus the number of readings required to achieve less than 10% precision of margin of error was calculated to be 6.

(a)	(b)
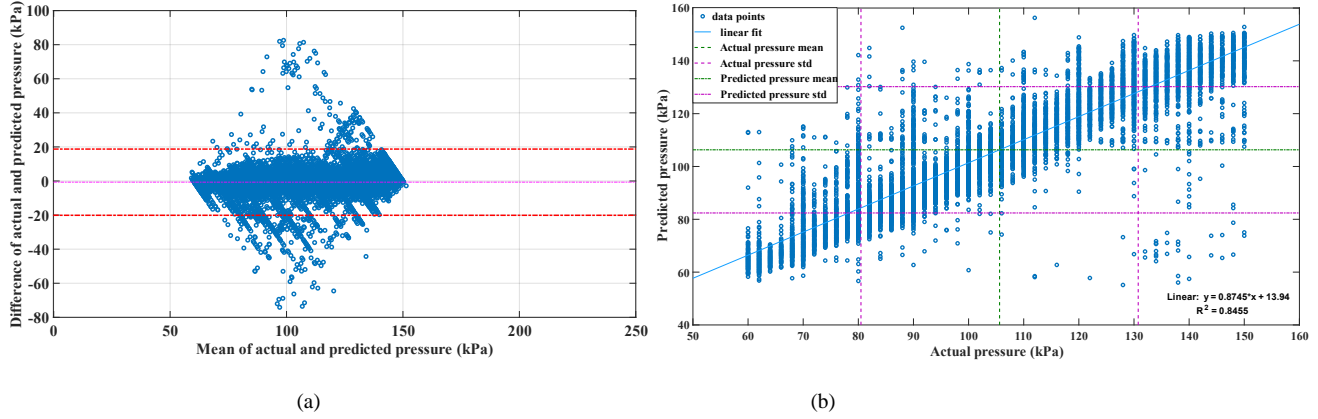
Figure.6.8 (a) Bland Altman plot of actual and predicted pressure using the TPM, (b) Comparison of pressure readings, actual vs predicted using the TPM.

E. *Experimental verification of the models.*

The model's accuracy was verified by comparing it to the results of experiments conducted on tubes suspended in water. The experiments were performed on latex and rubber tubes with thicknesses of 0.46 mm and 0.33 mm, respectively. The coefficient of determination ($R2$) for the three-parameter model was 0.4218 with a p-value of 0.042, while the coefficient of determination ($R2$) for the four-parameter model was 0.8426 with a p-value of 0.0002, as shown in Figure 9. The mean absolute percentage error for the three-parameter model was 8.73% and 3.68% for the four-parameter model, which are within clinically acceptable limits for blood pressure monitors [47]. This demonstrates the usability of the models in actual practice. However, one source of error in the experiment may be attributed to frequency downshift caused by damping [191]. All simulations were done with tubes without any intervening medium, while experiments were conducted with tubes in water. When applying the model to actual human arteries embedded within fat and muscles, the damping factor will be even higher, which may lead to further downshift in HMF peaks. The model's output may be further processed with damping factor estimates to improve measurements in real human arteries. Additionally, the model may be improved by conducting further simulations of arteries suspended in denser and more viscous mediums, or by using transfer learning by collecting data experimentally from multiple tubes with varying TT, ILD, and TD, and retraining the final layers of the models. Another problem with denser mediums is the fast dying-off of oscillations after impulsive unloading, making it more difficult to carry out short-time spectrograph analysis and reducing the accuracy of HMF determination. To overcome this, the speed of rebound of the wall after unloading may be analyzed to develop another model where HMF is replaced with rebound velocity.
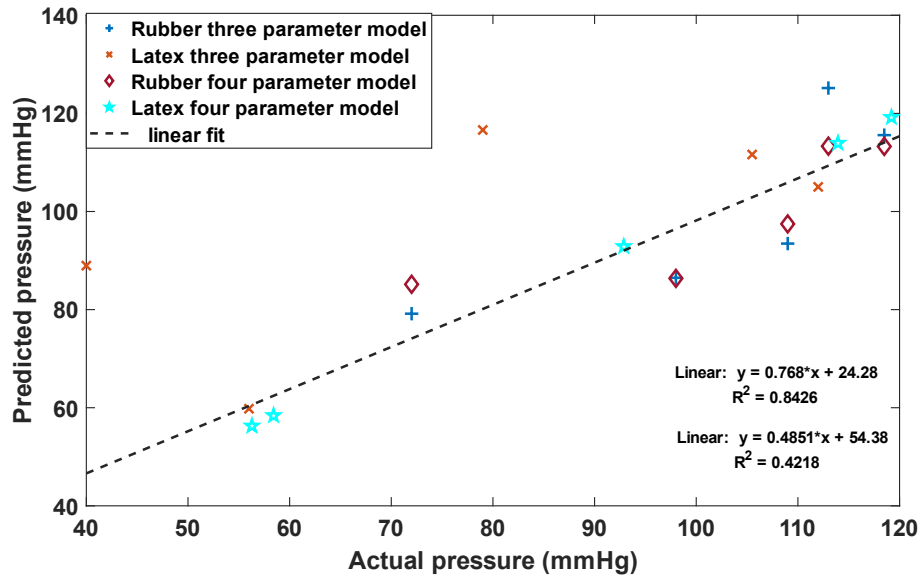
Figure.6.9. Validation of experimental results with both ML models applied on two different tubes taken through various IP.

6.4 Conclusion

In this study, we demonstrated the possibility of cuffless blood pressure measurement using ultrasound. We showed that it is possible to create an impulsive unloading of an artery under pressure using ARFI to make it oscillate in the hoop mode. Immediately after the ARFI pulse, the hoop mode vibration frequency can be determined through fast ultrasound imaging sequence followed by image processing and spectrographic analysis. We designed two different machine learning models that can measure internal pressure of the artery through parameters such as HMF, TT, ILD, and TD. These ML models were designed through extensive FEM eigen frequency simulations. The models were verified through actual experiments on arterial phantoms using custom-made software for the Verasonics research ultrasound system. The model could predict the IP with a mean absolute percentage error of 5.63% in the simulated data, and 3.68% in the experiments. We believe this would be a landmark work that would open further research for ultrasonic measurement of pressure in medical and other fields.

Chapter-7: Design a digital sphygmomanometer (Auscl-D) which is based on auscultatory method.
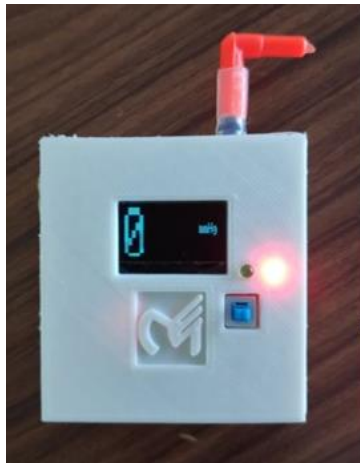
In this work, we propose a low-cost, highly portable, light-weight, easily manufacturable, battery operated, mercury free, auscultation based digital sphygmomanometer – Auscl-D, for easy and accurate BP measurements. The proposed device can be made from easily available components with cheap manufacturing processes available throughout globe, even in remote areas. The device demonstrated to have accuracy comparable to mercury sphygmomanometer, which is the gold-standard for BP measurements. The preliminary clinical trials were conducted at Dayanand Medical College & Hospital (DMCH) Ludhiana, to compare the performance of proposed device with commonly used aneroid sphygmomanometers employing the auscultatory method and validated oscillometric sphygmomanometers from Microlife. The test results show good agreement for systolic and diastolic BP measurements taken using Auscl-D device compared to the aneroid and oscillometric types. This shows the potential of the proposed design to serve as a low-cost, highly portable replacement for conventionally used sphygmomanometers, without the toxicity and reliability issues.

7.1 Introduction

Hypertension is the most prominent factor responsible for multiple cardiovascular and renal complications, engulfing more than quarter of world's population [192][193]. The diagnosis and management of hypertension is dependent on accurate measurement of blood pressure (BP) [7]. Overestimation of blood pressure is associated with various psychological effects, side effects from antihypertensive medications and high treatment costs, whereas underestimation of blood pressure can likely make patients deprived of necessary therapy, leading to high mortality rates from hypertension [4]. The direct measurement of BP is not practical, as it requires intra-arterial assessment. Therefore, BP determination is done via non-invasive ways which majorly includes measurements on arm over the brachial artery, providing useful information for hypertension monitoring and diagnosis [194].

However, even after decades of efforts to train clinicians on various techniques for proper BP measurements, routine clinical practices still suffer from inaccurate BP measurement problem [195]. Patient anxiety during hospital visit also contributes to this now well understood as white-coat hypertension [196]. These are hard to minimize, as humans are prone to accumulating various errors. Along with, the equipment used for BP monitoring can itself act as a source of inaccurate BP measurements, leading to misdiagnosis of hypertension [197]. Moreover, even if the device is operating accurately, the collective accumulation of various errors such as parallax error, prejudice for normal readings, inaccurate unit calibration etc. can lead to inaccurate systolic (SBP) and diastolic blood pressure (DBP) measurements [198]. These errors can be greatly minimized or completely eradicated by using efficient devices for BP measurements. Like by using digital readers for measurements, one can eliminate parallax error and prejudices to a great extent. Similarly, by using efficient algorithms that can automatically calibrate devices, one can avoid errors arising from unit calibration to a great extent.

Majorly, there are two pathways for BP monitoring: auscultatory and oscillometric BP measurements. Oscillometric BP measurements can be easily automated. A lesser degree of specialization or training is required to operate these devices even in high noise situations. But they suffer from poor sensitivity and specificity [199]. On the other hand, devices based on auscultatory measurements are more reliable but suffer from various operational and environmental health issues. For instance, aneroid based sphygmomanometers are more reliable than oscillometric devices but, can drift owing to mechanical jarring or accumulation of errors due to usage of mechanical springs in these devices [17]. Mercury-based sphygmomanometers are considered the gold standard for BP measurements but use environmentally toxic mercury as the chief ingredient. Also, they have to be continuously monitored for various factors such as leakage rate, calibration accuracy, physical assessment [200].

74

As, mercury has been established toxic to humans as well as environment, world's governments need to get rid of mercury-based sphygmomanometers in agreement to Minamata convention [50]. Additionally, both mercury and aneroid sphygmomanometers are bulky devices making them difficult to carry. But still clinicians prefer to use these mercury-based sphygmomanometers, due to reliable BP monitoring and training attained throughout years of their careers [19], [54].

After numerous efforts spanning decades, the leading bodies involved in device validation, have come up with a universal protocol to determine accuracy of BP measuring devices [201]. Various new oscillometric BP measurement devices have been developed to meet these requirements but results still remains unsatisfactory. For instance, easily portable wrist oscillometric offer highly portable BP measurements, but it suffers from poor medical efficacy as it gives unreliable data for very high or low BP measurements [202]. Even when comparing performance of two widely used oscillometric BP measurement devices, huge discrepancies in measurements were found, showing inefficacy of these devices [203]. Other modifications include utilizing finger photoplethysmography (PPG) signal or electronically recording Korotkoff-sounds [204], integrating deep learning algorithms to increase BP measurements accuracy [205], [206]. But these methods need to undergo rigorous clinical trials to prove their efficacy in real-life conditions. Non-invasive beat-to-beat BP measuring devices, such as Finapres [207], chest-based BP monitoring have also been developed [208], but these require bulky, non-portable and expensive equipment, reducing their viability for low-cost BP measurements. Additionally, these suffer from poor BP measurement reliability, as it requires calibration on daily basis [209].

Taking into notice all the limitations stated above, we have designed a digital auscultatory BP measurement device – *Auscl-D,* which displays BP reading digitally, like oscillometric devices, but measurements are performed using auscultation method employing traditional stethoscope and manual pumping system as in an aneroid device. The device is made from easily available components and economical manufacturing processes, making it viable to be purchased or assembled even in remote areas with limited resources. Its digital display provides direct line of sight for clinicians, to accurately visualize BP measurement readings while hearing kortkoff sounds in parallel. Providing advantage over conventional mercury or aneroid based sphygmomanometers, where clinicians have to carefully monitor SBP and DBP readings during rapidly changing device reading under high workload conditions. The device performance was on par against mercury sphygmomanometer in lab conditions and with aneroid and oscillometric sphygmomanometer in clinical setting. Preliminary clinical trials comprising of 30 participants were conducted at DMCH Ludhiana, aimed to compare the performance of Auscl-D with commonly used aneroid and oscillometric sphygmomanometer was conducted. The Aneroid sphygmomanometer is an auscultatory based BP monitoring device, where readings are taken manually by trained clinician from a mechanical dial. On other hand, Microlife is an oscillometric BP monitoring device, in which the average of three BP measurements, taken automatically, is displayed digitally. The correlation and Bland-Altman analysis reveals that the performance of Auscl-D for both SBP and DBP measurements is comparable to commonly used sphygmomanometers in hospitals.

7.2 Materials & Methods

7.2.1 Device design and operation

The proposed BP measurement device is made very compact and light-weight, for easy portability. It uses eco-friendly parts and is also installed with digital display for easy and accurate BP measurement readings, as shown in Figure.7.1. Moreover, it uses cost-effective, easily available components, making it easy to assemble without

requiring any expensive manufacturing processing. The design schematic, device operation and algorithms used for easy operation of the device has been detailed in this section.

A. Components used

All the components used are easily available off-the-shelf and can be assembled without requiring any specialized manufacturing equipment. The device design, showing various components, has been shown in Figure.7.1. The main characteristics of various components used in Auscl-D sphygmomanometer are

- *PCB:* for compact and efficient connectivity among various components, the device has been built-up on a PCB, whose design has been depicted in fig. 1. Various components such as Arduino pro-mini, display screen, pressure sensor, LEDs, battery and charging circuit have been mounted on this single PCB, leading to small size and weight of the proposed device.

- *Arduino pro mini*: rather than using conventional Arduino boards, Arduino pro-mini was used for miniaturizing final device configurations. It contains ATMEGA328 programmable microcontroller which controls the basic operations of the device, taking pressure readings from pressure sensor, which are then fed to OLED display for easy BP measurements. The power LED have been withdrawn from this controller board and rewired to the top of the enclosure panel to display power on state of the device to the user. This micro-controller acts as the brain of the device.

- *Pressure sensor:* for accurate pressure measurement readings, we used Honeywell SSCDAND005PGAA5 board mounted pressure sensor with pressure sensing range of 0-5 psi (purchased commercially). This sensor meets various industrial standards, offering robust and accurate operation under wide temperature range (-20°C to 85°C), while drawing minimal power (< 10nW).

- *OLED Display:* to display pressure reading taken by pressure sensor, 0.96-inch I2C/IIC 128x64 organic-light emitting diode (OLED) display with 4 pins has been installed in the device (commercially purchased). This provides high contrast, brightness, wide viewing angle, while consuming very low power (< 0.08W).

- *Stethoscope and cuff:* for auscultatory BP measurements, cuff is placed over brachial artery and when high pressure is created in cuff, a stethoscope is placed to monitor blood flow (as blood flow moves from turbulent to transition flow and finally to laminar flow) for reliable BP measurements (both stethoscope and cuff purchased commercially). It is connected directly to pressure sensor without any bends or additional air ducts, for eliminating any pressure build-ups or leakages leading to wrong BP measurements. A hook and loop arrangement are made on the surface of the cuff to attach the device on the cuff itself.

- *Lithium-ion battery:* to operate device remotely we provided 3.7 V, 240 mAH Li-Po battery (purchased commercially) enabling device to work for more than 6 hours on single charge. We used TP-4056 charging cum boost converter module (purchased commercially). This module in addition to enabling the charging of the LiPo battery boosts the output voltage to 5 V. This charging module can be operated using 5V, 1A DC power adapter or USB from PC. The battery is fully charged within 15 minutes. The charging circuit and battery are very small in size, which are placed directly under PCB board, increasing the portability of proposed device. The charging module allows for simultaneous operation while charging.

- *LEDs:* two energy efficient LEDs (red and green, purchased commercially) are used to depict device operation, providing visual aid for users. The device in this state has been depicted using red LED and device charging using green LED.
- *Holding box:* all the components (except for stethoscope and cuff) are arranged in compact but effective way in a 3D printed box (made of PLA), leading to small BP measuring device design (6×6×2.3 cm). The box was designed using SolidWorks software. Inlets for pressure sensor and charging are left in the box. Slot is made to fix the OLED display on top of box for easy BP measurements, as shown in Figure.7.1.
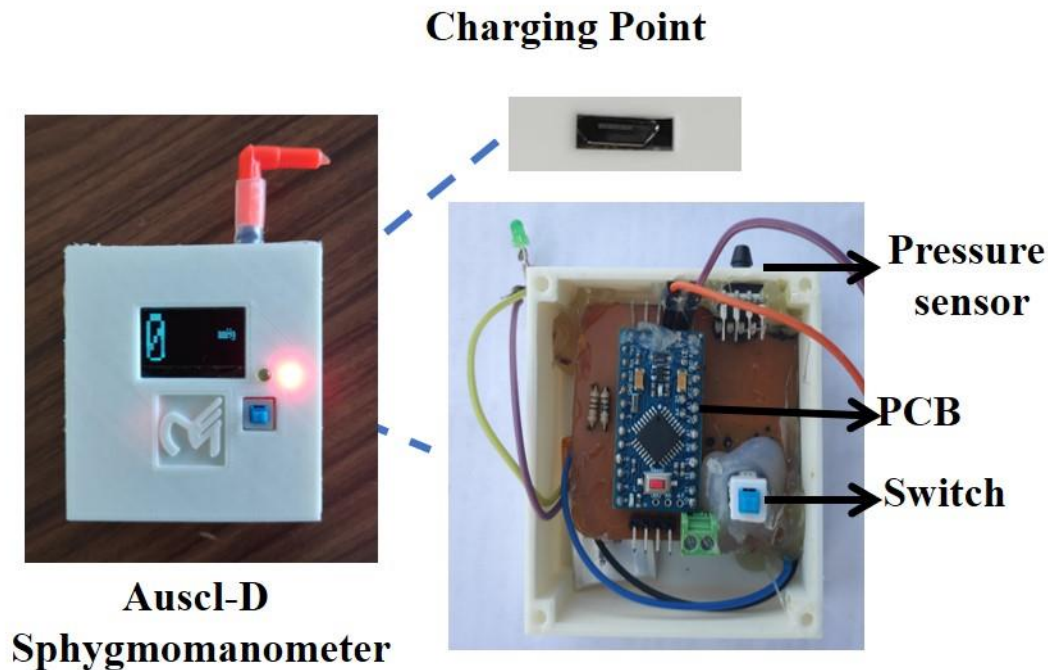
Figure.7.1. Auscl-D sphygmomanometer device architecture and corresponding components used in device.

7.2.2 Device Operation

The device should ideally be mounted on to the cuff that will provide a clear view path to the clinicians. After the person sits comfortably on the chair and the cuff is fastened around to the brachial artery. The clinician places the stethoscope over the brachial artery near the elbow. The small handheld air pump (bulb) having air release valve attached to the cuff is used to apply the pressure above the expected SBP level. No pulsations are heard through the stethoscope at this point. After this, the clinician carefully looks for the Korotkoff sounds through the stethoscope while the pressure in the cuff is slowly released. The very first Korotkoff sound heard i.e. K1marks the systolic pressure and the last sound K5 marks the diastolic pressure [172].

The schematic describing the whole device operation has been depicted in Figure.7.2. When air is pumped into the cuffs, the pressure starts to build up, which is sensed using the pressure sensor. The cuff is connected with the handheld air pump, termed as bulb. An appropriate T-connector has been used enabling proper air flow from cuff to pressure sensor without any additional pressure build-up or losses. The pressure sensor is powered by the

onboard 5 V power supply from the boost converter. The analog output voltage V_{out} is proportional to the pressure (P) at its input port and is calibrated using equation (1)

$$P = \left(\frac{V_{out} - 0.5}{0.8}\right) * 51.71 \text{ mmHg} \tag{1}$$

The Arduino pro mini consisting of ATMEGA328 programmable microcontroller, acts as the brain of the device. It converts the pressure readings into readable form. Mean of five successive pressure readings is taken from the pressure sensor with a couple of milliseconds gap between to minimize the errors associated with electronic BP measurements. Then this pressure reading in mmHg is displayed on the OLED display.
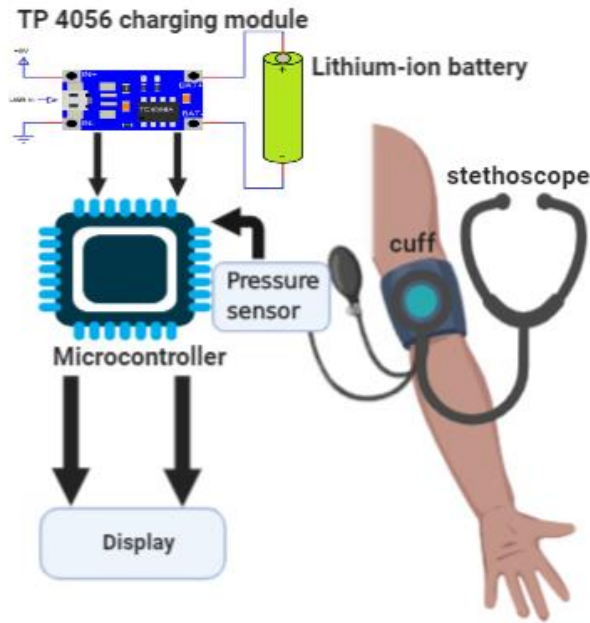
Figure.7.2 Schematic depicting device operation.

7.3 Results

To validate the technical accuracy of Auscl-D, we compared the pressure measurements taken by our device with mercury sphygmomanometer. For obtaining the clinical accuracy, trials were conducted at DMCH, Ludhiana, after due ethical clearance from its IEC. Here we compared the performance of Auscl-D with two commonly used sphygmomanometers namely Aneroid (auscultatory) and Micro-life (Oscillometeric) sphygmomanometers. The results obtained have been discussed in this section.
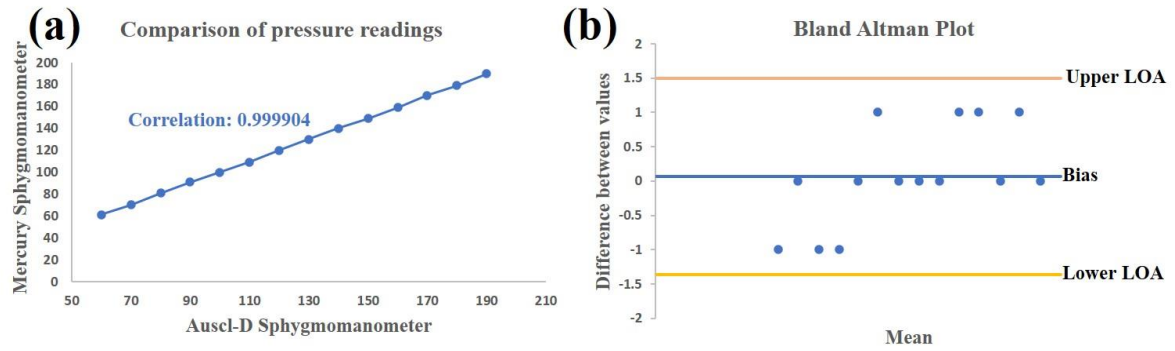
Figure.7.3 Comparison of pressure reading from Auscl-D and Mercury sphygmomanometer and their corresponding (a) correlation values and (b) bland-Altman plot.

7.3.1 Comparison of Auscl-D and Mercury sphygmomanometer

To check the technical accuracy of pressure readings of our proposed device design, we compared Auscl-D pressure readings against mercury sphygmomanometer which is considered as the gold standard for BP measurements. The air valve from cuff was split in two using a T-connector, one valve goes to mercury sphygmomanometer and other to Auscl-D, ensuring equal pressure build-up in both valves. We took data spanning wide pressures ranging from 60 mmHg to 200 mmHg, covering possible SBP and DBP measurements in humans. Results have been presented in Figure.7.3. The pressure readings from two sphygmomanometers are almost equal, as clear by correlation value of 0.9999 (Figure.7.3 (a)). Moreover, the Bland-Altman plot reports the bias value of 0.0714 mmHg with standard deviation (SD) of mere 0.73 mmHg, among the two values. All the pressure readings are well inside the upper and lower limit-of-agreement (LOA) (mean ± 1.96 x SD), as clear from Figure.7.3 (b). Moreover, the maximum difference between the pressure reading taken from two sphygmomanometers is a mere 1 mmHg, which can also be attributed to human or parallax errors associated with BP measurements using mercury sphygmomanometer. Also, both sphygmomanometers have the least count of 1 mmHg, rendering the differences depicted here negligible.

7.3.2 Clinical Trials

To compare the performance of proposed Auscl-D sphygmomanometer against commonly used sphygmomanometers in hospitals, we performed preliminary clinical trials at DMCH Ludhiana. All the measurements were performed by trained clinicians (Figure.7.4). A total of 30 participants, across various age groups (26-70 years, mean±standard deviation: 50.9±11.78 years) and sex (19 male, 11 female), were tested for SBP and DBP measurements, using commonly used aneroid sphygmomanometer against Auscl-D sphygmomanometer. Additionally, a total of 20 participants, across various age groups (27-70 years, mean 48.7±13.45 years) and sex (11 male, 9 female), were tested using validated oscillometric device from MicroLife against Auscl-D. The BP measurements done using Auscl-D and aneroid sphygmomanometer correlates to high degree, with correlation factor of 0.9418 for SBP and 0.8739 for DBP measurements, as shown in Figure.7.5 (a) and 7.5 (b) respectively. Bland-Altman analysis reveals that BP measurements done using Auscl-D sphygmomanometer has bias of 0.73 mmHg with SD value of 5.86 mmHg for SBP and -1.97 mmHg with SD of 5.37 mmHg for DBP measurements, as compared to aneroid sphygmomanometer. The upper and lower limits of

agreement (LOA) were calculated to be 12.22 mmHg and -10.75 mmHg for SBP along with 8.56 mmHg and -12.49 mmHg for DBP, respectively. Figure.7.5 (c) and 7.5 (d), shows that all the measurements are well inside upper and lower LOA for both SBP and DBP measurements, showing the efficacy of proposed design against commonly used aneroid sphygmomanometer. Additionally, the mean absolute error percentage between the measurements from two sphygmomanometers is computed to be 4.12% for SBP and 5.96% for DBP measurements. Likewise, comparison between BP measurements using Auscl-D and MicroLife has been done, by taking SBP and DBP measurements over 20 individuals. The BP measurements correlate to a high degree, with correlation factor of 0.9348 for SBP and 0.9252 for DBP measurements, as shown in Figure.7.6 (a) and 7.6 (b) respectively. Bland-Altman analysis shows that bias between the readings taken using these two sphygmomanometers is 2.05 mmHg with SD value of 5.23 mmHg for SBP and -0.55 mmHg with SD of 3.76 mmHg for DBP measurements. The upper and lower LOA were computed to be 12.29 mmHg and -8.19 mmHg for SBP along with 6.82 mmHg and -7.92 mmHg for DBP respectively. Figure.7.6 (c) and 7.6 (d) shows that all the measurements of SBP and DBP are well inside upper and lower LOA. This shows the efficacy of the proposed design against the commonly used Microlife sphygmomanometer. In addition, the mean absolute error percentage between the measurements from two sphygmomanometers is computed to be 3.67% for SBP and 3.86% for DBP measurements.

Figure 7.4 Real-time BP measurements using Auscl-D sphygmomanometer
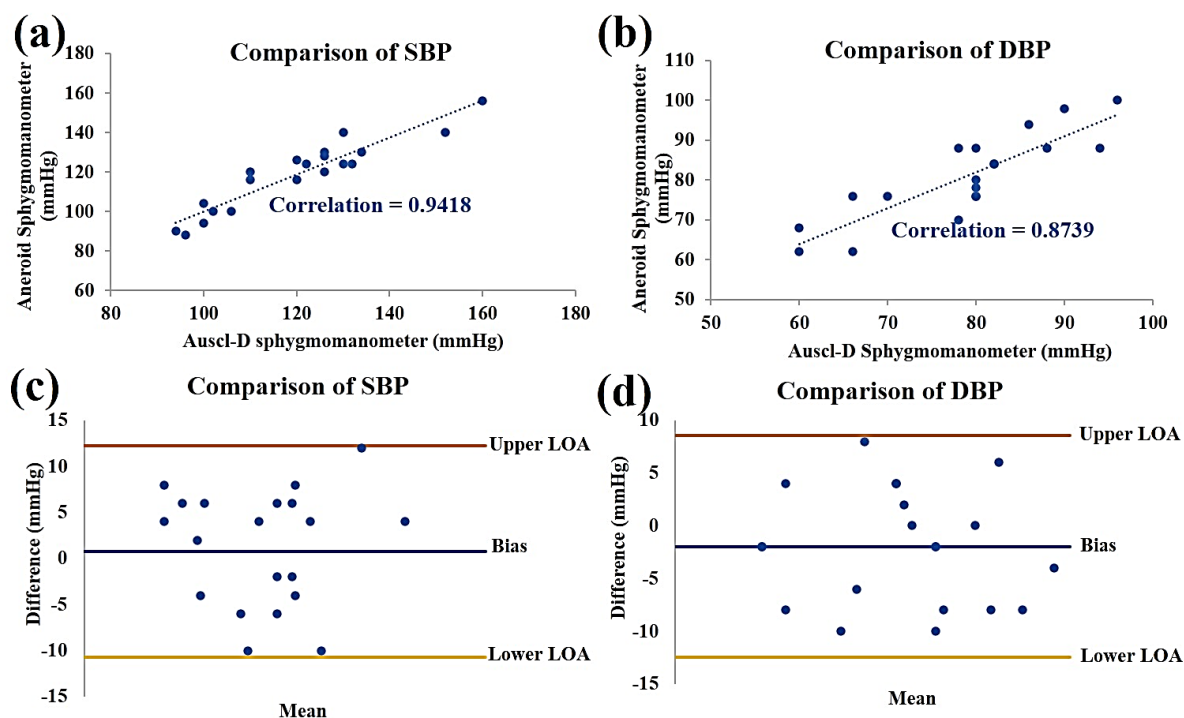
Figure.7.5 Clinical trials for comparison of BP measurements using Auscl-D and Aneroid sphygmomanometer, their corresponding correlation graphs for (a) SBP and (b) DBP pressures along with bland-altman plot for (c) SBP and (d) DBP measurements.
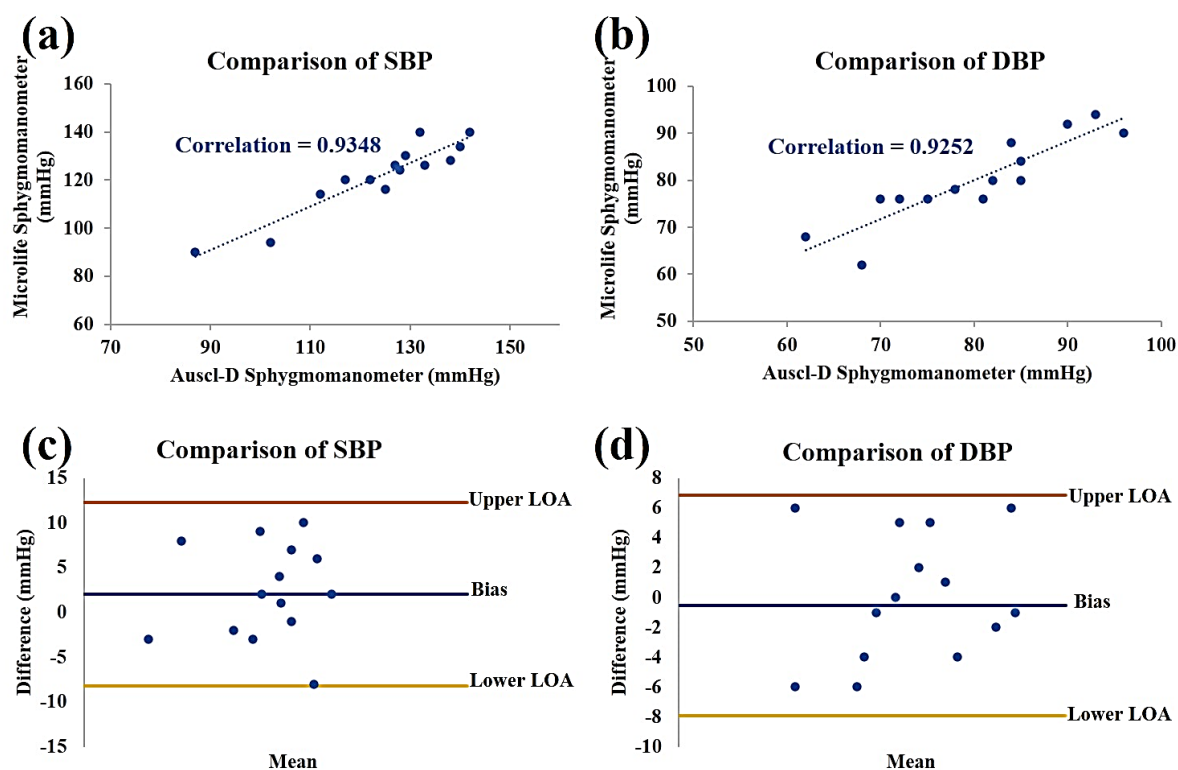
Figure.7.6 Clinical trials for comparison of BP measurements using Auscl-D and MicroLife sphygmomanometer, their corresponding correlation graphs for (a) SBP and (b) DBP along with bland-altman plot for (c) SBP and (d) DBP measurements.

7.4 Discussion

The mean absolute error for BP measurements using proposed Auscl-D sphygmomanometer is well within the accepted limits as compared to commonly used aneroid and oscillometric sphygmomanometers. Moreover, proposed design shows comparable performance as compared to gold-standard mercury-based sphygmomanometer for direct one-to-one comparison of pressure readings (Fig. 3). But same results were not reproduced during clinical trials, which can also be attributed to accumulation of various error, such as clinician errors or prejudices, patient anxiety etc. Additionally, the aneroid and Microlife sphygmomanometers, which are used as reference BP monitoring devices here, are also prone to various errors and limitations [210][211].

7.5 Conclusion

In conclusion, we have designed a low-cost, easy to use, battery operated, mercury free hybrid sphygmomanometer, Auscl-D, that can serve as a viable replacement for commonly used mercury sphygmomanometer. Moreover, its compact and light-wight design enables its usage during transportation or high-stress conditions (as in hospitals). The electronic display enables easy BP measurements without any parallax errors associated with commonly used auscultatory devices. Moreover, the accuracy of this device is found to be matching to mercury sphygmomanometer, as confirmed by individual pressure readings. Also, preliminary clinical trials show that the performance of Auscl-D is on par with commonly used aneroid and validated oscillometric devices, making it a viable, cost-effective, and easily manufacturable replacement for conventional sphygmomanometer.

7.6 Ethical Declaration

The clinical study reported in this paper was conducted at DMCH Ludhiana in conformity with the Declaration of Helsinki. Informed consent was taken from all participants after explaining the operation of the Auscl-D device and experimental procedure. The study was approved by the Institutional ethics committee of DMCH.

Chapter-8: Other different notable work in medical devices.

8.1 A Device to Reduce Vasovagal Syncope in Blood Donors

Syncope is a temporary loss of consciousness caused by a decrease in blood flow to the brain. It is classified into three main categories: reflex syncope, syncope due to orthostatic hypotension, and cardiac syncope. One type of reflex syncope is Vasovagal syncope (VVS), which is triggered by emotional or physical stress and is characterized by symptoms such as sweating, pallor, and nausea. Donating blood is generally safe, but some donors may experience adverse reactions such as VVS. Studies have reported that VVS occurs in 1-2% of blood donations. To prevent VVS, physical maneuvers such as leg crossing and muscle tensing have been proposed, but these methods require training and may not be suitable for all donors. To address this issue, in this work, we propose a low-cost, low-power, compact, and portable electronic massager unit that can be used in blood donation chairs to reduce the rate of VVS in donors. The massager is designed to reduce anxiety before blood donation and improve peripheral blood circulation, thus reducing the risk of VVS. The design and usability of the massager prototype are described in this work [212].

Device Operation

This device should ideally be mounted on the blood donation chair itself. After the patient lies down on the reclining chair, the two cuffs are applied to the calf muscles on both legs (Fig. 5). To operate this device first a low pressure set-point is set by the operator and then the device is powered on. The cuffs start to inflate and deflate as per the pressure ceiling set by the knob. The setpoint is increased slows until can feel a relaxing massaging effect on the calf muscle. If the pressure set-point is set too high, the patient may feel uncomfortable and, in this case, the setpoint should be brought down by appropriate control signal through the knob. After this the blood donation process is started. Once the donation is complete, the device is turned off and the cuffs are gently removed before the patients deboards the donation chair. The final look of the device is shown in Figure.8.1.

Figure.8.1 (a) Electronic components used in device, (b) Placement of device in Blood donor chair, (c) Device demonstration, (d) Final look of the device.

8.2 Development of low cost ambu bag attachment for rapid mass emergency deployment as a ventilator

The novel Coronavirus disease-2019 (COVID-19) has affected the entire world, causing severe impacts on both developed and developing countries and resulting in the deaths of millions. The disease primarily affects the respiratory system and can lead to severe conditions such as acute respiratory distress syndrome (ARDS) or hypoxemia due to widespread lung inflammation. Traditional ventilator devices can be expensive and require trained personnel for proper operation. In developing countries, these types of ventilators are often limited and only found in specialized hospitals. To address the urgent need for ventilators, we propose a low-cost, easy-to-assemble, portable automated AMBU resuscitator system that can be scaled up to combat the ongoing pandemic. During the COVID-19 pandemic, various low-cost mechanical ventilators have been proposed to address the shortage of ventilators. These designs have their own advantages and disadvantages when compared in terms of design, performance, cost, and actuation mechanism. These ventilators require specialized parts that are not readily available in the market, but they are intended to provide ventilation not only inside hospitals but also outside of them, where hospital-grade ventilators are not feasible due to their portability. The proposed ventilators are unable to provide all the modes available in hospital-grade ventilators such as pressure mode, volume mode, and assist mode. Our AARMED ventilator is designed to be rapidly manufactured and requires custom-designed parts such as an arm, belt driver, inlet and outlet connector, and AMBU bag holder, which were first designed in Solidworks and fabricated using an extrusion-based 3D printer. The electrical system development is classified into hardware and software development and include components like Arduino uno, pressure sensor, flow sensor, stepper motor, Jetson Nano, Touch screen, IR sensor. The device also features a user-friendly GUI created using open-source Qt creator software, where a user can control the breathing rate, I:E ratio, peak pressure, tidal volume. Initial testing was performed on the IMT analysis test lung. The various parameters can be controlled by the help of touch screen base GUI and the clinician can also monitor the health condition of the patient on the same GUI. We had also improved the motor capability by using the micro stepping of the stepper motor and we also improved our design and fixed all the previous hardware bugs. The final prototype of the device is shown in Figure.8.2 [213] .

Device operation

This device is having a capability to operate in two different modes along with assist mode. The developed device can be controlled by touch screen-based GUI system by adjusting the BPM slider, pressure slider, volume slider and I:E ratio push buttons. Modes can be easily selected by the toggle switch that can switch between pressure mode and volume mode along with assist or normal mode as shown in the Figure.8.3(c). Pressure, flow rate and volume curves of the patient can be monitored on the plot tab as shown in the Figure. 8.3(b).
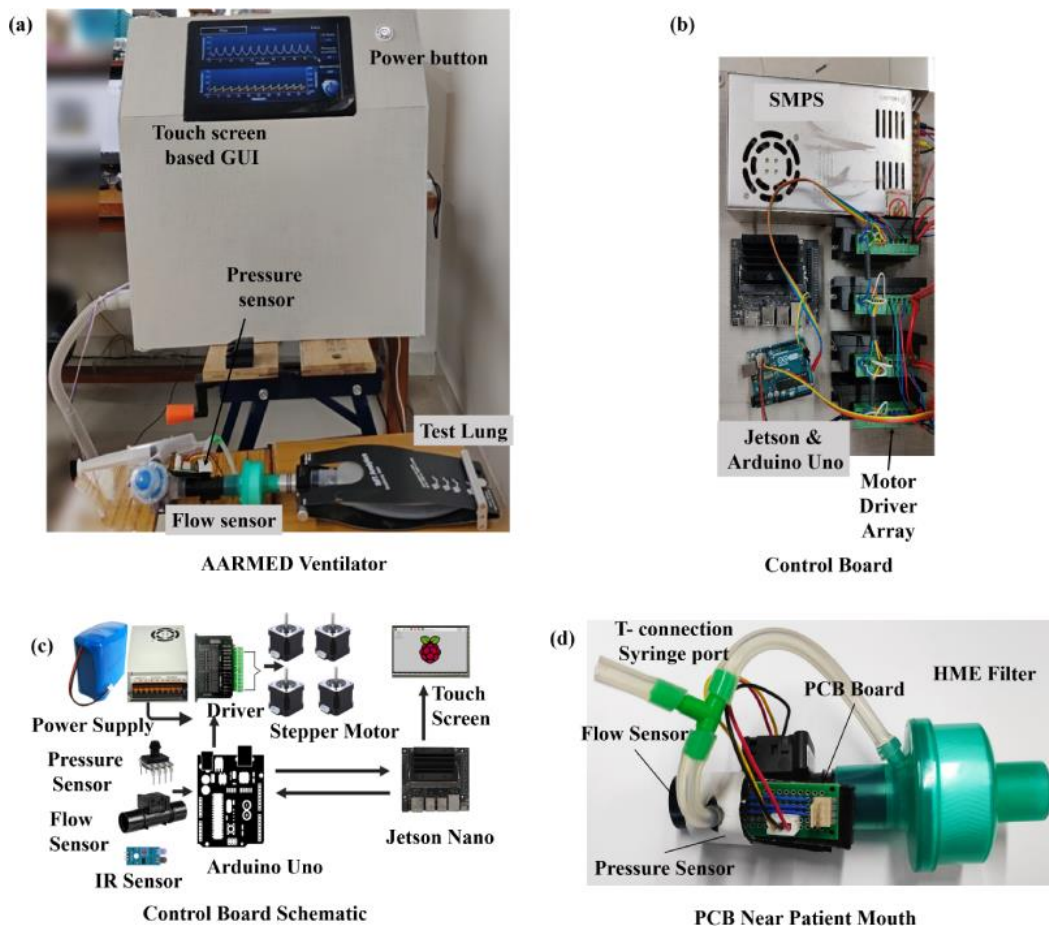
Figure.8.2 Prototype (a) Prototype of ventilator, (b) Control Board, (c) Control Schematic (d) Instrumentation at end of ventilator circuit near patient's mouth.

Figure.8.3 Touch Screen based GUI (a) Splash screen of GUI (b) Display Console (c) Setting Console.

8.3 AMLEX- A Smart Patient Driven Oxygen Rationing Device

Oxygen is one of the second most abundant gas followed by nitrogen in the atmosphere. Still, its availability in hospitals of many developing countries is a significant concern. The COVID-19 virus has severely affected the world in many ways. Especially for poor and developing countries where the medical research, technology development, and facilities are at an infant stage, this pandemic has hit hard and had a profound impact on people living in those countries. COVID-19 is a respiratory disease that affects an individual's lungs, leading to suffocation or oxygen deprivation. One needs external assistance, which is provided via an external oxygen supply. In conventional systems, a constant flow of oxygen is maintained during both the inhalation and exhalation phase of the user, which leads to the wastage of oxygen supplied during the exhalation phase. A novel device has been developed to tackle this problem that halts the flow of oxygen from the reservoir when the user exhales, which is detected by a humidity sensor installed in the mask worn by the user. An adaptive algorithm allows the system to adapt to the different users and environmental conditions. The prototype has been tested in the lab on multiple individuals, and the system showed satisfactory results by average saving of 1.72 Liters of oxygen in 1 min of breathing cycle. The final prototype of the device is shown in Figure.8.4

Device operation

In the present work, we present Amlex, a low cost, intelligent oxygen rationing system controlled by patient's breathing cycles. Specially machined couplings with threads on both ends allow the device to be connected directly onto the opening end of any commercially available oxygen cylinder. The device restricts the flow of oxygen from the cylinder during exhalation, which is detected by a sensor installed in the mask worn by the user in close vicinity to mouth and nose. Amlex utilizes a humidity sensor to detect the humidity concentration variation during the operation, which makes the device usable with any commercial mask with holes in it. The proposed device is operational even with dislocation and leakage in the mask as the algorithm used changes the window size of the threshold values and enables the device to work with accuracy. Here, the window size refers to the difference between upper threshold value and lower threshold value in vertical axis. During the inhalation period, the electro-mechanical actuator (Solenoid valve) opens and allows the oxygen flow from the reservoir (oxygen cylinder). The oxygen is further channeled to the mask via a flexible polymer tube. The electromechanical actuator continuously opens and closes in synchronization with the inhalation and exhalation of the user during the operation. For reliable operation and to prevent any false detection of the breathing phase, an optimal sized window between the threshold values to detect exhalation and inhalation needs to be maintained. Here, window size refers to the difference between upper and lower threshold values in vertical axis. The device's smart algorithm adapts to varying environmental conditions and maintains an optimal window size by continuously updating the threshold values. The device can operate on a battery and line power supply (220V 50Hz AC). An additional flow sensor to measure the flow has also been installed in the device for characterization of oxygen consumption and saving. (This flow sensor is part of the assembly for data analysis and will not be a part of the final product for clinical use) .
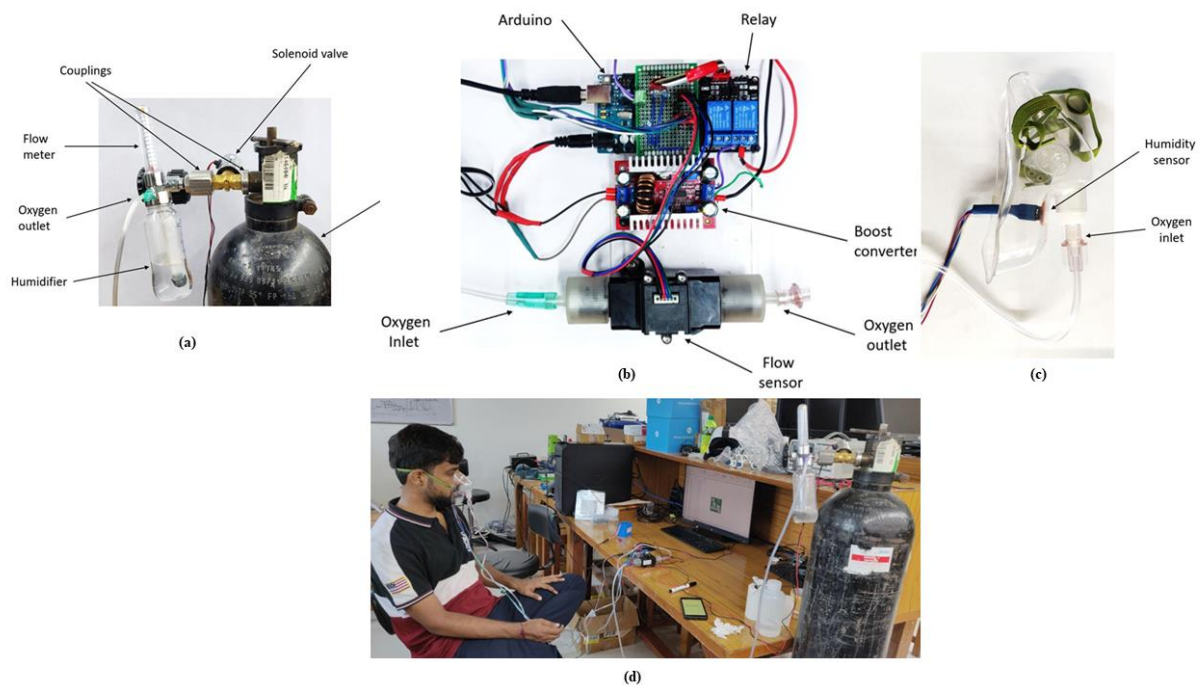
Figure.8.4. (a) This shows the solenoid valve connected to the oxygen cylinder with the help of couplings. The commercially available flow meter can be seen which tells the flow in Liters per minute along with the humidifier whose outlet is connected to the flexible tubing which is further connected to the main device. (b) This shows the setup of the device with the control unit, relays, boost converter, and sensors. (c) This shows the humidity sensor installed in a commercially available mask. (d) This shows a subject using the device while the data is being recorded on the PC

Chapter-9: Conclusion and Future scopes

9.1 Summary of contributions

This thesis presents a novel approach and device capable of non-invasively measuring a patient's blood pressure. The thesis is more pointing towards cuff and cuffless based blood pressure monitoring technologies. The main Key findings of the thesis are as follows.

The thesis discusses about various developments in the medical industry related to measurement devices and equipment, specially focusing on the blood pressure measurement devices. Here we mention that mercury sphygmomanometers are already banned in many countries and are set to be banned in India by the end of 2020. However, a survey conducted by us found that there is a higher perceived accuracy and reliability of mercury sphygmomanometers compared to other devices in the market. To address this issue, the authors propose promoting validated oscillometric devices to change Indian clinicians' perspectives towards non-mercury alternatives for blood pressure measurement.

- In this thesis, we propose the use of the eutectic alloy Galinstan as a substitute for mercury. This material is non-toxic and eco-friendly, but it contains a percentage of gallium which can form oxide when in contact with oxygen. This can cause stickiness and hinders visibility when poured into a conventional manometer. To overcome this issue, we have explored various solutions such as doping the material with other metals, creating a core-shell formation, and coating solutions. However, these methods are not robust or transparent in nature. After extensive literature research, we have proposed a solution of coating the glass tube surface with a thin layer of gallium oxide as a proof of concept. This coating solution shows 98% transparency, stability and does not affect line of sight communication. In this work, we used a method of physical vapour deposition to coat a thin layer of gallium oxide on various surfaces. This coating was found to make surfaces non-wetting when exposed to surface oxidized gallium-based liquid. We conducted various characterizations to support that this lyophobicity is caused by the surface roughness inherent to the gallium deposition technique. The coating is effective in providing a non-wetting path for surface oxidized liquid metal to move freely on. This homogenous material surface treatment for gallium-based liquid metal can remove barriers where wetting is an issue and has potential applications in healthcare products such as thermometers and blood pressure measurements. This technique can be applied to both flat and non-planar surfaces.

- Additive manufacturing (AM), also known as 3D printing, has greatly impacted the manufacturing industry by introducing a range of techniques that can quickly and easily produce complex geometries. This technology also holds great potential in the biomedical field, enabling the creation of intricate, customized products that would have been challenging or impossible to manufacture using traditional methods. The advancement in AM is particularly promising for people with disabilities, as it offers the possibility of receiving custom-made artificial organs, which can significantly improve their quality of life. Here we used this technology to manufacture our device named "Merkfree". All parts of the device were made through the process of 3D printing.

- We have created Merkfree, a mercury-free sphygmomanometer that operates on the same principle as a traditional mercury sphygmomanometer (MS). Merkfree aims to be similar to an MS while eliminating

the use of mercury, in line with the Minamata Convention of WHO. It uses the same auscultation method to measure blood pressure and has been shown to have less than 10% error compared to an MS. The key innovation of Merkfree is the use of Galinstan instead of mercury, which has a lower density and a longer scale height, improving visibility and reducing errors. A new technique was also developed to eliminate the stickiness of Galinstan with glass. In this paper, we describe the components of Merkfree and report the results of clinical trials on 252 patients comparing it to both MS and other sphygmomanometers (OS).

- We demonstrated the feasibility of measuring blood pressure without the use of a cuff by using ultrasound. We used Acoustic Radiation Force Impulse (ARFI) to create an impulsive unloading of an artery under pressure, causing it to oscillate in the "hoop mode." The frequency of this hoop mode vibration can be determined using a fast ultrasound imaging sequence and image processing and spectrographic analysis. We developed two machine learning models that can estimate internal pressure of the artery using parameters such as Hoop Mode Frequency (HMF), Transit Time (TT), Integrated Luminosity Distribution (ILD), and Time Delay (TD). These models were designed using Finite Element Method (FEM) eigen frequency simulations and were verified through experiments on arterial phantoms using custom-made software for the Verasonics research ultrasound system. The model was able to predict internal pressure with a mean absolute percentage error of 5.63% in simulated data and 3.68% in experimental data. This research paves the way for further studies on ultrasonic measurement of pressure in medical and other fields.

- Overall, the study emphasizes the importance of finding new and improved methods of measuring blood pressure, specifically non-invasive and non-mercury alternatives, and the potential for new technologies like superhydrophobic coatings and additive manufacturing to aid in this goal.

9.2 Future scope

After the phase-out of mercury sphygmomanometers in healthcare, a significant gap was created. To fill this gap, the Merkfree device was introduced as an affordable alternative that offers the same accuracy and feel as a mercury sphygmomanometer. The main drawback of these devices is that they are point-in-time measurements, taking approximately 10 minutes to complete. However, cuffless measurement methods address this by providing continuous monitoring. To improve this device, incorporating AI-driven technology and designing it as a handheld system would make it more user-friendly and convenient to use.

References

[1]   P. M. Kearney, M. Whelton, K. Reynolds, P. Muntner, P. K. Whelton, and J. He, "Global burden of hypertension: analysis of worldwide data," *Lancet*, vol. 365, no. 9455, pp. 217–223, Jan. 2005, doi: 10.1016/S0140-6736(05)17741-1.

[2]   "Sleep Apnoea Infographic Can Help People Understand Risks." https://myhillsdentist.com/blog/sleep-apnoea-infographic-can-help-people-understand-risks/ (accessed Jan. 20, 2023).

[3]   J. He and P. K. Whelton, "Epidemiology and prevention of hypertension," *Med Clin North Am*, vol. 81, no. 5, pp. 1077–1097, 1997, doi: 10.1016/S0025-7125(05)70568-X.

[4]   H. Arima, F. Barzi, and J. Chalmers, "Mortality patterns in hypertension," *J Hypertens*, vol. 29 Suppl 1, no. SUPPL. 1, 2011, doi: 10.1097/01.HJH.0000410246.59221.B1.

[5]   C. Y. Wu, H. Y. Hu, Y. J. Chou, N. Huang, Y. C. Chou, and C. P. Li, "High blood pressure and all-cause and cardiovascular disease mortalities in community-dwelling older adults," *Medicine (United States)*, vol. 94, no. 47, p. e2160, 2015, doi: 10.1097/MD.0000000000002160.

[6]   C. Li and T. N. Kelly, "Hypertension in India," *J Hypertens*, vol. 32, no. 6, pp. 1189–1191, 2014, doi: 10.1097/hjh.0000000000000158.

[7]   J. E. Sharman *et al.*, "Lancet Commission on Hypertension group position statement on the global improvement of accuracy standards for devices that measure blood pressure," *J Hypertens*, vol. 38, no. 1, p. 21, Jan. 2020, doi: 10.1097/HJH.0000000000002246.

[8]   "Health matters: combating high blood pressure - GOV.UK." https://www.gov.uk/government/publications/health-matters-combating-high-blood-pressure/health-matters-combating-high-blood-pressure (accessed Dec. 14, 2022).

[9]   E. Agabiti-Rosei *et al.*, "Central blood pressure measurements and antihypertensive therapy: a consensus document," *Hypertension*, vol. 50, no. 1, pp. 154–160, Jul. 2007, doi: 10.1161/HYPERTENSIONAHA.107.090068.

[10]   P. Muntner *et al.*, "Measurement of Blood Pressure in Humans: A Scientific Statement From the American Heart Association," *Hypertension*, vol. 73, no. 5, pp. E35–E66, May 2019, doi: 10.1161/HYP.0000000000000087.

[11]   P. V. G. Kumar, S. Deshpande, and H. R. Nagendra, "Traditional practices and recent advances in Nadi Pariksha: A comprehensive review," *J Ayurveda Integr Med*, vol. 10, no. 4, pp. 308–315, 2019, doi: 10.1016/j.jaim.2017.10.007.

[12]   J. Booth, "A Short History of Blood Pressure Measurement," *J R Soc Med*, vol. 70, no. 11, pp. 793–799, 1977, doi: 10.1177/003591577707001112.

[13]   B. Scheer, A. Perel, and U. J. Pfeiffer, "Clinical review: complications and risk factors of peripheral arterial catheters used for haemodynamic monitoring in anaesthesia and intensive care medicine," *Crit Care*, vol. 6, no. 3, p. 199, 2002, doi: 10.1186/CC1489.

[14]   K. Tegtmeyer, G. Brady, S. Lai, R. Hodo, and D. Braner, "Videos in Clinical Medicine. Placement of an arterial line," *N Engl J Med*, vol. 354, no. 15, p. e13, Apr. 2006, doi: 10.1056/NEJMVCM044149.

[15]   R. Kumar, M. Kumar, G. S. Wander, and A. K. Sahani, "Concept, hardware development, and clinical trials of a Galinstan based Mercury free sphygmomanometer: Merkfree," *Scientific Reports 2022 12:1*, vol. 12, no. 1, pp. 1–10, Sep. 2022, doi: 10.1038/s41598-022-19926-7.

[16]   G. S. Stergiou, P. P. Giovas, C. P. Gkinos, and D. G. Tzamouranis, "Validation of the A&D UM-101 professional hybrid device for office blood pressure measurement according to the International Protocol," *Blood Press Monit*, vol. 13, no. 1, pp. 37–42, Feb. 2008, doi: 10.1097/MBP.0B013E3282C9ACB0.

[17] J. J. S. Waugh, M. Gupta, J. Rushbrook, A. Halligan, and A. H. Shennan, "Hidden errors of aneroid sphygmomanometers," *Blood Press Monit*, vol. 7, no. 6, pp. 309–312, Dec. 2002, doi: 10.1097/00126097-200212000-00003.

[18] G. A. Van Montfrans, "Oscillometric blood pressure measurement: progress and problems," *Blood Press Monit*, vol. 6, no. 6, pp. 287–290, 2001, doi: 10.1097/00126097-200112000-00004.

[19] R. Kumar, A. K. Sahani, and G. S. Wander, "A survey to gauge confidence of Indian clinicians on three primary devices for blood pressure measurement," *Blood Press Monit*, pp. 196–199, 2021, doi: 10.1097/MBP.0000000000000512.

[20] G. Ogedegbe and T. Pickering, "Principles and Techniques of Blood Pressure Measurement," *Cardiol Clin*, vol. 28, no. 4, pp. 571–586, 2010, doi: 10.1016/j.ccl.2010.07.006.

[21] T. G. Pickering *et al.*, "Recommendations for blood pressure measurement in humans and experimental animals. Part 1: Blood pressure measurement in humans: A statement for professionals from the subcommittee of professional and public education of the American Heart Association council on high blood pressure research," *Hypertension*, vol. 45, no. 1, pp. 142–161, Jan. 2005, doi: 10.1161/01.HYP.0000150859.47929.8E.

[22] M. R. Nelson, J. Stepanek, M. Cevette, M. Covalciuc, R. T. Hurst, and A. J. Tajik, "Noninvasive Measurement of Central Vascular Pressures With Arterial Tonometry: Clinical Revival of the Pulse Pressure Waveform?," *Mayo Clin Proc*, vol. 85, no. 5, p. 460, 2010, doi: 10.4065/MCP.2009.0336.

[23] "Development and modelling of arterial applanation tonometry: a review - PubMed." https://pubmed.ncbi.nlm.nih.gov/11847449/ (accessed Dec. 21, 2022).

[24] G. M. Drzewiecki, J. Melbin, and A. Noordergraaf, "Arterial tonometry: Review and analysis," *J Biomech*, vol. 16, no. 2, pp. 141–152, Jan. 1983, doi: 10.1016/0021-9290(83)90037-4.

[25] M. Kachuee, M. M. Kiani, H. Mohammadzade, and M. Shabany, "Cuff-less high-accuracy calibration-free blood pressure estimation using pulse transit time," *2015 IEEE International Symposium on Circuits and Systems (ISCAS)*, vol. 2015-July, pp. 1006–1009, Jul. 2015, doi: 10.1109/ISCAS.2015.7168806.

[26] M. Pour Ebrahim *et al.*, "Blood Pressure Estimation Using On-body Continuous Wave Radar and Photoplethysmogram in Various Posture and Exercise Conditions," *Sci Rep*, vol. 9, no. 1, p. 16346, 2019, doi: 10.1038/s41598-019-52710-8.

[27] D. M. Bard, J. I. Joseph, and N. van Helmond, "Cuff-Less Methods for Blood Pressure Telemonitoring," *Front Cardiovasc Med*, vol. 6, p. 40, Apr. 2019, doi: 10.3389/FCVM.2019.00040/BIBTEX.

[28] D. J. Korteweg, "Ueber die Fortpflanzungsgeschwindigkeit des Schalles in elastischen Röhren," *Ann Phys*, vol. 241, no. 12, pp. 525–542, Jan. 1878, doi: 10.1002/ANDP.18782411206.

[29] D. J. Hughes, C. F. Babbs, L. A. Geddes, and J. D. Bourland, "Measurements of Young's modulus of elasticity of the canine aorta with ultrasound.," *Ultrason Imaging*, vol. 1, no. 4, pp. 356–367, Oct. 1979, doi: 10.1177/016173467900100406.

[30] R. Anchan, "Estimating pulse wave velocity using mobile phone sensors," *The Grants Register 2022*, pp. 376–377, 2021.

[31] Y. Hsu and D. J. Young, "Skin-Coupled Personal Wearable Ambulatory Pulse Wave Velocity Monitoring System Using Microelectromechanical Sensors," *IEEE Sens J*, vol. 14, no. 10, pp. 3490–3497, 2014, doi: 10.1109/JSEN.2014.2345779.

[32] Y.-J. Lee *et al.*, "Magneto-Plethysmographic Sensor for Peripheral Blood Flow Velocity," *IEEE Sens J*, vol. 14, no. 5, pp. 1341–1342, 2014, doi: 10.1109/JSEN.2014.2304752.

[33] S. L.-O. Martin *et al.*, "Weighing Scale-Based Pulse Transit Time is a Superior Marker of Blood Pressure than Conventional Pulse Arrival Time," *Sci Rep*, vol. 6, p. 39273, Dec. 2016, doi: 10.1038/srep39273.

[34] F. Heydari *et al.*, "Continuous Cuffless Blood Pressure Measurement Using Body Sensors," in *2018 IEEE SENSORS*, 2018, pp. 1–4. doi: 10.1109/ICSENS.2018.8630294.

[35] R. Mukherjee, S. Ghosh, B. Gupta, and T. Chakravarty, "A Universal Noninvasive Continuous Blood Pressure Measurement System for Remote Healthcare Monitoring.," *Telemed J E Health*, vol. 24, no. 10, pp. 803–810, Oct. 2018, doi: 10.1089/tmj.2017.0257.

[36] L. W. J. Bogert and J. J. Van Lieshout, "Non-invasive pulsatile arterial pressure and stroke volume changes from the human finger," *Exp Physiol*, vol. 90, no. 4, pp. 437–446, 2005, doi: 10.1113/EXPPHYSIOL.2005.030262.

[37] J. PENAZ, "Photoelectric measurement of blood pressure, volume and flow in the finger'In:Digest of the 10th International Conference on Medical and Biological Engineering," *Dresden*, vol. 104, 1973.

[38] M. S. Ganio, R. M. Brothers, R. A. I. Lucas, J. L. Hastings, and C. G. Crandall, "Validity of auscultatory and Penaz blood pressure measurements during profound heat stress alone and with an orthostatic challenge," *Am J Physiol Regul Integr Comp Physiol*, vol. 301, no. 5, Nov. 2011, doi: 10.1152/AJPREGU.00247.2011.

[39] F. Li, L. Wang, Y. Fan, and D. Li, "Simulation of noninvasive blood pressure estimation using ultrasound contrast agent microbubbles," *IEEE Trans Ultrason Ferroelectr Freq Control*, vol. 59, no. 4, pp. 715–726, Apr. 2012, doi: 10.1109/TUFFC.2012.2249.

[40] C. Tremblay-Darveau, R. Williams, and P. N. Burns, "Measuring absolute blood pressure using microbubbles," *Ultrasound Med Biol*, vol. 40, no. 4, pp. 775–787, 2014, doi: 10.1016/J.ULTRASMEDBIO.2013.10.017.

[41] F. Forsberg, J. Bin Liu, W. T. Shi, J. Furuse, M. Shimizu, and B. B. Goldberg, "In vivo pressure estimation using subharmonic contrast microbubble signals: proof of concept," *IEEE Trans Ultrason Ferroelectr Freq Control*, vol. 52, no. 4, pp. 581–583, 2005, doi: 10.1109/TUFFC.2005.1428040.

[42] A. Crimi, M. Makhinya, U. Baumann, C. Thalhammer, G. Szekely, and O. Goksel, "Automatic Measurement of Venous Pressure Using B-Mode Ultrasound," *IEEE Trans Biomed Eng*, vol. 63, no. 2, pp. 288–299, Feb. 2016, doi: 10.1109/TBME.2015.2455953.

[43] B. W. A. M. M. Beulen, N. Bijnens, G. G. Koutsouridis, P. J. Brands, M. C. M. Rutten, and F. N. van de Vosse, "Toward Noninvasive Blood Pressure Assessment in Arteries by Using Ultrasound," *Ultrasound Med Biol*, vol. 37, no. 5, pp. 788–797, May 2011, doi: 10.1016/J.ULTRASMEDBIO.2011.01.020.

[44] A. M. Zakrzewski and B. W. Anthony, "Noninvasive blood pressure estimation using ultrasound and simple finite element models," *IEEE Trans Biomed Eng*, vol. 65, no. 9, pp. 2011–2022, Sep. 2018, doi: 10.1109/TBME.2017.2714666.

[45] S. Weber, P. Scharfschwerdt, T. Schauer, T. Seel, U. Kertzscher, and K. Affeld, "Continuous Wrist Blood Pressure Measurement with Ultrasound.," *Biomed Tech (Berl)*, vol. 58 Suppl 1, Aug. 2013, doi: 10.1515/bmt-2013-4124.

[46] S. Buchanan, P. Orris, and J. Karliner, "Alternatives to the mercury sphygmomanometer," *J Public Health Policy*, vol. 32, no. 1, pp. 107–120, Feb. 2011, doi: 10.1057/JPHP.2010.38.

[47] G. S. Stergiou *et al.*, "A universal standard for the validation of blood pressure measuring devices: Association for the Advancement of Medical Instrumentation/European Society of Hypertension/International Organization for Standardization (AAMI/ESH/ISO) Collaboration Statement," *Hypertension*, vol. 71, no. 3, pp. 368–374, 2018, doi: 10.1161/HYPERTENSIONAHA.117.10237.

[48] D. Karunasagar, M. V. Balarama Krishna, Y. Anjaneyulu, and J. Arunachalam, "Studies of mercury pollution in a lake due to a thermometer factory situated in a tourist resort: Kodaikkanal, India," *Environ Pollut*, vol. 143, no. 1, pp. 153–158, Sep. 2006, doi: 10.1016/J.ENVPOL.2005.10.032.

[49] N. J. Langford and R. E. Ferner, "EPISODES OF ENVIRONMENTAL POISONING WORLDWIDE," *Occup Environ Med*, vol. 59, no. 12, pp. 855–860, Dec. 2002, doi: 10.1136/OEM.59.12.855.

[50] H. Selin, "Global Environmental Law and Treaty-Making on Hazardous Substances: The Minamata Convention and Mercury Abatement," *Glob Environ Polit*, vol. 14, no. 1, pp. 1–19, 2014, doi: 10.1162/GLEP_A_00208.

[51] D. W. Jones, E. D. Frohlich, C. M. Grim, C. E. Grim, and K. A. Taubert, "Mercury sphygmomanometers should not be abandoned: An advisory statement from the Council for High Blood Pressure Research, American Heart Association," *Hypertension*, vol. 37, no. 2, pp. 185–186, 2001, doi: 10.1161/01.HYP.37.2.185.

[52] "MINAMATA CONVENTION ON MERCURY TEXT AND ANNEXES".

[53] 134 Executive Board, "Public health impacts of exposure to mercury and mercury compounds: the role of WHO and ministries of public health in the implementation of the Minamata Convention." 2014.

[54] U. Kaul *et al.*, "Self-blood pressure measurement as compared to office blood pressure measurement in a large Indian population; the India Heart Study," *J Hypertens*, vol. 38, no. 7, pp. 1262–1270, Jul. 2020, doi: 10.1097/HJH.0000000000002410.

[55] E. Chung, G. Chen, B. Alexander, and M. Cannesson, "Non-invasive continuous blood pressure monitoring: a review of current applications," *Front Med*, vol. 7, no. 1, pp. 91–101, Mar. 2013, doi: 10.1007/S11684-013-0239-5.

[56] S. S. Franklin, L. Thijs, T. W. Hansen, E. O'Brien, and J. A. Staessen, "White-Coat Hypertension," *Hypertension*, vol. 62, no. 6, pp. 982–987, 2013, doi: 10.1161/HYPERTENSIONAHA.113.01275.

[57] H. Pessenhofer, "Single cuff comparison of two methods for indirect measurement of arterial blood pressure: standard auscultatory method versus automatic oscillometric method," *Basic Res Cardiol*, vol. 81, no. 1, pp. 101–109, Jan. 1986, doi: 10.1007/BF01907432/METRICS.

[58] N. R. C. Campbell, A. Chockalingham, J. G. Fodor, and D. W. McKay, "Accurate, reproducible measurement of blood pressure.," *CMAJ: Canadian Medical Association Journal*, vol. 143, no. 1, p. 19, Jul. 1990.

[59] G. A. Van Montfrans, "Oscillometric blood pressure measurement: progress and problems," *Blood Press Monit*, vol. 6, no. 6, pp. 287–290, 2001, doi: 10.1097/00126097-200112000-00004.

[60] J. Liu, H. M. Cheng, C. H. Chen, S. H. Sung, J. O. Hahn, and R. Mukkamala, "Patient-Specific Oscillometric Blood Pressure Measurement: Validation for Accuracy and Repeatability," *IEEE J Transl Eng Health Med*, vol. 5, 2017, doi: 10.1109/JTEHM.2016.2639481.

[61] A. Benmira *et al.*, "From Korotkoff and Marey to automatic non-invasive oscillometric blood pressure measurement: does easiness come with reliability?," *Expert Rev Med Devices*, vol. 13, no. 2, pp. 179–189, Feb. 2016, doi: 10.1586/17434440.2016.1128821.

[62] W. M. Fairbank and M. O. Scully, "A new noninvasive technique for cardiac pressure measurement: resonant scattering of ultrasound from bubbles," *IEEE Trans Biomed Eng*, vol. 24, no. 2, pp. 107–110, 1977, doi: 10.1109/TBME.1977.326112.

[63] G. M. Drzewiecki, J. Melbin, and A. Noordergraaf, "Arterial tonometry: Review and analysis," *J Biomech*, vol. 16, no. 2, pp. 141–152, 1983, doi: 10.1016/0021-9290(83)90037-4.

[64] E. Chung, G. Chen, B. Alexander, and M. Cannesson, "Non-invasive continuous blood pressure monitoring: a review of current applications," *Front Med*, vol. 7, no. 1, pp. 91–101, Mar. 2013, doi: 10.1007/S11684-013-0239-5.

[65] P. Grimm, "Social Desirability Bias," *Wiley International Encyclopedia of Marketing*, Dec. 2010, doi: 10.1002/9781444316568.WIEM02057.

[66] R. Kumar and A. Sahani, "Role of superhydrophobic coatings in biomedical applications," *Mater Today Proc*, vol. 45, Mar. 2021, doi: 10.1016/j.matpr.2021.02.457.

[67] A. Arias *et al.*, "Structural, Optical, and Electrical Characterization of β-Ga_2O_3 Thin Films Grown by Plasma-Assisted Molecular Beam Epitaxy Suitable for UV Sensing," *Advances in Materials Science and Engineering*, vol. 2018, p. 9450157, 2018, doi: 10.1155/2018/9450157.

[68] R. O'Donoghue *et al.*, "Low temperature growth of gallium oxide thin films via plasma enhanced atomic layer deposition," *Dalton Transactions*, vol. 46, no. 47, pp. 16551–16561, 2017, doi: 10.1039/C7DT03427J.

[69] K. Seshan, *Handbook of Thin Film Deposition Techniques Principles, Methods, Equipment and Applications, Second Editon*. 2002. doi: 10.1201/9781482269680.

[70] P. R. Jubu, F. K. Yam, and A. T. Moses, "Deposition of Gallium Oxide Nanostructures at Low Substrate Temperature by Chemical Vapor Deposition," *ECS Journal of Solid State Science and Technology*, vol. 9, no. 3, p. 035006, Mar. 2020, doi: 10.1149/2162-8777/ab7b47.

[71] M. Psarski, J. Marczak, J. Grobelny, and G. Celichowski, "Superhydrophobic Surface by Replication of Laser Micromachined Pattern in Epoxy/Alumina Nanoparticle Composite," *J Nanomater*, vol. 2014, p. 547895, 2014, doi: 10.1155/2014/547895.

[72] M. Liu, S. Wang, and L. Jiang, "Nature-inspired superwettability systems," *Nat Rev Mater*, vol. 2, no. 7, p. 17036, 2017, doi: 10.1038/natrevmats.2017.36.

[73] T. R. Prianka *et al.*, "Recent exploration of bio-mimetic nanomaterial for potential biomedical applications," *Materials Science and Engineering: C*, vol. 93, pp. 1104–1115, 2018, doi: https://doi.org/10.1016/j.msec.2018.09.012.

[74] S. Wang, K. Liu, X. Yao, and L. Jiang, "Bioinspired Surfaces with Superwettability: New Insight on Theory, Design, and Applications," *Chem Rev*, vol. 115, no. 16, pp. 8230–8293, Aug. 2015, doi: 10.1021/cr400083y.

[75] Z. Li and Z. Guo, "Bioinspired surfaces with wettability for antifouling application," *Nanoscale*, vol. 11, no. 47, pp. 22636–22663, 2019, doi: 10.1039/c9nr05870b.

[76] X. Zhang, Y. Si, J. Mo, and Z. Guo, "Robust micro-nanoscale flowerlike ZnO/epoxy resin superhydrophobic coating with rapid healing ability," *Chemical Engineering Journal*, vol. 313, pp. 1152–1159, 2017, doi: 10.1016/j.cej.2016.11.014.

[77] N. M. Alves, J. Shi, E. Oramas, J. L. Santos, H. Tomás, and J. F. Mano, "No Title," *J. Biomed. Mater. Res. A*, vol. 91, no. null, p. 480, 2009.

[78] K. Tadanaga, K. Kitamuro, A. Matsuda, and T. Minami, "No Title," *J. Sol-Gel Sci. Technol*, vol. 26, no. null, p. 705, 2003.

[79] N. Shirtcliffe, G. McHale, M. Newton, and C. C. Perry, "No Title," *Langmuir*, vol. 21, no. null, p. 937, 2005.

[80] R. Asmatulu, M. Ceylan, and N. Nuraje, "No Title," *Langmuir*, vol. 27, no. null, p. 504, 2010.

[81] B. Balu, V. Breedveld, and D. W. Hess, "No Title," *Langmuir*, vol. 24, no. null, p. 4785, 2008.

[82] T. O. Yoon, H. J. Shin, S. C. Jeoung, and Y. I. Park, "Formation of superhydrophobic poly(dimethysiloxane) by ultrafast laser-induced surface modification," *Opt. Express*, vol. 16, no. 17, p. 12715, 2008.

[83] M. Khorasani, H. Mirzadeh, and Z. Kermani, "No Title," *Appl. Surf. Sci*, vol. 242, no. null, p. 339, 2005.

[84] Y. Lai *et al.*, "Transparent superhydrophobic/superhydrophilic TiO2-based coatings for self-cleaning and anti-fogging," *J Mater Chem*, vol. 22, no. 15, pp. 7420–7426, 2012, doi: 10.1039/C2JM16298A.

[85] A. Hooda, M. S. Goyat, J. K. Pandey, A. Kumar, and R. Gupta, "A review on fundamentals, constraints and fabrication techniques of superhydrophobic coatings," *Prog Org Coat*, vol. 142, no. January, p. 105557, 2020, doi: 10.1016/j.porgcoat.2020.105557.

[86] A. S. Lynch and G. T. Robertson, "Bacterial and fungal biofilm infections.," *Annu Rev Med*, vol. 59, pp. 415–428, 2008, doi: 10.1146/annurev.med.59.110106.132000.

[87] P. Chaignon, I. Sadovskaya, C. Ragunah, N. Ramasubbu, J. B. Kaplan, and S. Jabbouri, "Susceptibility of staphylococcal biofilms to enzymatic treatments depends on their chemical composition.," *Appl Microbiol Biotechnol*, vol. 75, no. 1, pp. 125–132, May 2007, doi: 10.1007/s00253-006-0790-y.

[88] A. Elzaabalawy, "Potential of combating transmission of COVID-19 using novel self-cleaning superhydrophobic surfaces : part II — thermal , chemical , and mechanical durability," *International*

Journal of Mechanics and Materials in Design, vol. 0123456789, 2020, doi: 10.1007/s10999-020-09512-y.

[89] H. Zhong *et al.*, "Reusable and Recyclable Graphene Masks with Outstanding Superhydrophobic and Photothermal Performances," 2020, doi: 10.1021/acsnano.0c02250.

[90] S. A. Mahadik, F. P. Sarika, S. M. Brahmanand, and S. S. Thorat, "Biocompatible superhydrophobic coating material for biomedical applications," *J Solgel Sci Technol*, pp. 0–1, 2016, doi: 10.1007/s10971-016-4244-4.

[91] P. Zhang and F. Y. Lv, "A review of the recent advances in superhydrophobic surfaces and the emerging energy-related applications," *Energy*, vol. 82, pp. 1068–1087, 2015, doi: https://doi.org/10.1016/j.energy.2015.01.061.

[92] R. Kumar and A. K. Sahani, "Role of superhydrophobic coatings in biomedical applications," *Mater Today Proc*, vol. 45, pp. 5655–5659, 2021, doi: 10.1016/j.matpr.2021.02.457.

[93] Y. Lei, R. Sun, X. Zhang, X. Feng, and L. Jiang, "Oxygen-Rich Enzyme Biosensor Based on Superhydrophobic Electrode," *Advanced Materials*, vol. 28, no. 7, pp. 1477–1481, Feb. 2016, doi: 10.1002/adma.201503520.

[94] A. De Ninno *et al.*, "An integrated superhydrophobic-plasmonic biosensor for mid-infrared protein detection at the femtomole level," *Physical Chemistry Chemical Physics*, vol. 17, no. 33, pp. 21337–21342, 2015, doi: 10.1039/C4CP05023A.

[95] K. Khanmohammadi Chenab, B. Sohrabi, and A. Rahmanzadeh, "Superhydrophobicity: Advanced biological and biomedical applications," *Biomater Sci*, vol. 7, no. 8, pp. 3110–3137, 2019, doi: 10.1039/c9bm00558g.

[96] T. Xu *et al.*, "Superwettable Electrochemical Biosensor toward Detection of Cancer Biomarkers," *ACS Sens*, vol. 3, no. 1, pp. 72–78, 2018, doi: 10.1021/acssensors.7b00868.

[97] Y. Liu, W. Yao, X. Yin, H. Wang, Z. Han, and L. Ren, "Controlling Wettability for Improved Corrosion Inhibition on Magnesium Alloy as Biomedical Implant Materials," *Adv Mater Interfaces*, vol. 3, no. 8, p. 1500723, Apr. 2016, doi: 10.1002/admi.201500723.

[98] S. Supriadi, B. Suharno, T. Widjaya, S. T. Ayuningtyas, and E. R. Baek, "Development of Superhydrophobic Material SS 17-4 PH for Bracket Orthodontic Application by Metal Injection Molding," *IOP Conf Ser Mater Sci Eng*, vol. 299, p. 12096, 2018, doi: 10.1088/1757-899x/299/1/012096.

[99] D. Patil, S. Aravindan, M. Kaushal Wasson, V. P., and P. V Rao, "Fast Fabrication of Superhydrophobic Titanium Alloy as Antibacterial Surface Using Nanosecond Laser Texturing," *J Micro Nanomanuf*, vol. 6, no. 1, Dec. 2017, doi: 10.1115/1.4038093.

[100] V. Jokinen, E. Kankuri, S. Hoshian, S. Franssila, and R. H. A. Ras, "Superhydrophobic Blood-Repellent Surfaces," *Advanced Materials*, vol. 30, no. 24, 2018, doi: 10.1002/adma.201705104.

[101] C. Liu *et al.*, "A high-efficiency superhydrophobic plasma separator," *Lab Chip*, vol. 16, no. 3, pp. 553–560, 2016, doi: 10.1039/C5LC01235J.

[102] J. Liu *et al.*, "Elastic Superhydrophobic and Photocatalytic Active Films Used as Blood Repellent Dressing," vol. 1908008, no. 30 mL, 2020, doi: 10.1002/adma.201908008.

[103] "Self-cleaning materials for doctors and hospitals." https://www.dr-hempel-network.com/medtec-medical-technology/self-cleaning-materials/ (accessed Aug. 20, 2020).

[104] W. Barthlott and C. Neinhuis, "Purity of the sacred lotus, or escape from contamination in biological surfaces," *Planta*, vol. 202, no. 1, pp. 1–8, 1997, doi: 10.1007/s004250050096.

[105] A. Venkateswara Rao, S. S. Latthe, D. Y. Nadargi, H. Hirashima, and V. Ganesan, "Preparation of MTMS based transparent superhydrophobic silica films by sol-gel method," *J Colloid Interface Sci*, vol. 332, no. 2, pp. 484–490, 2009, doi: 10.1016/j.jcis.2009.01.012.

[106] S. Yu, Z. Guo, and W. Liu, "Biomimetic transparent and superhydrophobic coatings: From nature and beyond nature," *Chemical Communications*, vol. 51, no. 10, pp. 1775–1794, 2015, doi: 10.1039/c4cc06868h.

[107] Z. Guo and W. Liu, "Biomimic from the superhydrophobic plant leaves in nature: Binary structure and unitary structure," *Plant Science*, vol. 172, no. 6, pp. 1103–1112, Jun. 2007, doi: 10.1016/j.plantsci.2007.03.005.

[108] E. Salimi, "Superhydrophobic blood-compatible surfaces: state of the art," *International Journal of Polymeric Materials and Polymeric Biomaterials*, vol. 69, no. 6, pp. 363–372, 2020, doi: 10.1080/00914037.2019.1570510.

[109] J. Bravo, L. Zhai, Z. Wu, R. E. Cohen, and M. F. Rubner, "Transparent superhydrophobic films based on silica nanoparticles," *Langmuir*, vol. 23, no. 13, pp. 7293–7298, Jun. 2007, doi: 10.1021/la070159q.

[110] Q. F. Xu, J. N. Wang, and K. D. Sanderson, "Organic-inorganic composite nanocoatings with superhydrophobicity, good transparency, and thermal stability," *ACS Nano*, vol. 4, no. 4, pp. 2201–2209, 2010, doi: 10.1021/nn901581j.

[111] Y. Lai *et al.*, "Transparent superhydrophobic/superhydrophilic TiO 2-based coatings for self-cleaning and anti-fogging," *J Mater Chem*, vol. 22, no. 15, pp. 7420–7426, 2012, doi: 10.1039/c2jm16298a.

[112] D. Sriramulu, E. L. Reed, M. Annamalai, T. V. Venkatesan, and S. Valiyaveettil, "Synthesis and Characterization of Superhydrophobic, Self-cleaning NIR-reflective Silica Nanoparticles," *Sci Rep*, vol. 6, pp. 1–10, 2016, doi: 10.1038/srep35993.

[113] L. Xu and J. He, "Fabrication of highly transparent superhydrophobic coatings from hollow silica nanoparticles," *Langmuir*, vol. 28, no. 19, pp. 7512–7518, 2012, doi: 10.1021/la301420p.

[114] Y. Xiu, D. W. Hess, and C. P. Wong, "A novel method to prepare superhydrophobic, self-cleaning and transparent coatings for biomedical applications," *Proceedings - Electronic Components and Technology Conference*, pp. 1218–1223, 2007, doi: 10.1109/ECTC.2007.373949.

[115] Y. Li, Z. Zhang, M. Wang, X. Men, and Q. Xue, "Environmentally safe, substrate-independent and repairable nanoporous coatings: Large-scale preparation, high transparency and antifouling properties," *J Mater Chem A Mater*, vol. 5, no. 38, pp. 20277–20288, 2017, doi: 10.1039/c7ta05112c.

[116] S. A. Mahadik, M. S. Kavale, S. K. Mukherjee, and A. V. Rao, "Transparent superhydrophobic silica coatings on glass by sol-gel method," *Appl Surf Sci*, vol. 257, no. 2, pp. 333–339, 2010, doi: 10.1016/j.apsusc.2010.06.062.

[117] H. K. Park, S. W. Yoon, W. W. Chung, B. K. Min, and Y. R. Do, "Fabrication and characterization of large-scale multifunctional transparent ITO nanorod films," *J Mater Chem A Mater*, vol. 1, no. 19, pp. 5860–5867, 2013, doi: 10.1039/c3ta10422b.

[118] Y. Yoon, D. W. Lee, and J. B. Lee, "Fabrication of optically transparent PDMS artificial lotus leaf film using underexposed and underbaked photoresist mold," *Journal of Microelectromechanical Systems*, vol. 22, no. 5, pp. 1073–1080, 2013, doi: 10.1109/JMEMS.2013.2264729.

[119] L. Zhang, C. H. Xue, M. Cao, M. M. Zhang, M. Li, and J. Z. Ma, "Highly transparent fluorine-free superhydrophobic silica nanotube coatings," *Chemical Engineering Journal*, vol. 320, pp. 244–252, Jul. 2017, doi: 10.1016/j.cej.2017.03.048.

[120] Y. Yoo, J. B. You, W. Choi, and S. G. Im, "A stacked polymer film for robust superhydrophobic fabrics," *Polym Chem*, vol. 4, no. 5, pp. 1664–1671, 2013, doi: 10.1039/c2py20963b.

[121] "Surfaces and Interfaces of Biomimetic Superhydrophobic Materials | Wiley." https://www.wiley.com/en-us/Surfaces+and+Interfaces+of+Biomimetic+Superhydrophobic+Materials-p-9783527342648 (accessed Dec. 19, 2020).

[122] R. Di Mundo, F. Palumbo, and R. D'Agostino, "Nanotexturing of polystyrene surface in fluorocarbon plasmas: from sticky to slippery superhydrophobicity," *Langmuir*, vol. 24, no. 9, pp. 5044–5051, 2008, doi: 10.1021/la800059a.

[123] "Processing and Finishing of Polymeric Materials, 2 Volume Set | Wiley." https://www.wiley.com/en-in/Processing+and+Finishing+of+Polymeric+Materials%2C+2+Volume+Set-p-9781118582732 (accessed Dec. 19, 2020).

[124] K. Teshima, H. Sugimura, Y. Inoue, O. Takai, and A. Takano, "Transparent ultra water-repellent poly(ethylene terephthalate) substrates fabricated by oxygen plasma treatment and subsequent hydrophobic coating," in *Applied Surface Science*, Elsevier, May 2005, pp. 619–622. doi: 10.1016/j.apsusc.2004.10.143.

[125] Z. He *et al.*, "Fabrication of a transparent superamphiphobic coating with improved stability," *Soft Matter*, vol. 7, no. 14, pp. 6435–6443, 2011, doi: 10.1039/c1sm05574g.

[126] J. T. Han, S. Y. Kim, J. S. Woo, and G. W. Lee, "Transparent, conductive, and superhydrophobic films from stabilized carbon nanotube/silane sol mixture solution," *Advanced Materials*, vol. 20, no. 19, pp. 3724–3727, Oct. 2008, doi: 10.1002/adma.200800239.

[127] L. Shen, W. Wang, H. Ding, and Q. Guo, "Flame soot stably deposited on silicone coatings possess superhydrophobic surface," *Appl Surf Sci*, vol. 284, pp. 651–656, 2013, doi: 10.1016/j.apsusc.2013.07.149.

[128] C. Jiang, Y. Zhang, Q. Wang, and T. Wang, "Superhydrophobic polyurethane and silica nanoparticles coating with high transparency and fluorescence," *J Appl Polym Sci*, vol. 129, no. 5, pp. 2959–2965, Sep. 2013, doi: 10.1002/app.39024.

[129] M. Knoblauch, J. M. Hibberd, J. C. Gray, and A. J. E. van Bel, "A galinstan expansion femtosyringe for microinjection of eukaryotic organelles and prokaryotes," *Nat Biotechnol*, vol. 17, no. 9, pp. 906–909, Sep. 1999, doi: 10.1038/12902.

[130] T. Liu, P. Sen, and C. J. Kim, "Characterization of nontoxic liquid-metal alloy galinstan for applications in microdevices," *Journal of Microelectromechanical Systems*, vol. 21, no. 2, pp. 443–450, 2012, doi: 10.1109/JMEMS.2011.2174421.

[131] J. Jeon, S. K. Chung, J. B. Lee, S. J. Doo, and D. Kim, "Acoustic wave-driven oxidized liquid metal-based energy harvester," *EPJ Applied Physics*, vol. 81, no. 2, p. 20902, Feb. 2018, doi: 10.1051/epjap/2018180011.

[132] N. Lazarus and S. S. Bedair, "Improved power transfer to wearable systems through stretchable magnetic composites," *Appl Phys A Mater Sci Process*, vol. 122, no. 5, pp. 1–7, May 2016, doi: 10.1007/s00339-016-0067-y.

[133] M. Mayyas *et al.*, "Liquid-Metal-Templated Synthesis of 2D Graphitic Materials at Room Temperature," *Advanced Materials*, vol. 32, no. 29, p. 2001997, Jul. 2020, doi: https://doi.org/10.1002/adma.202001997.

[134] M. B. Ghasemian *et al.*, "Doping Process of 2D Materials Based on the Selective Migration of Dopants to the Interface of Liquid Metals," *Advanced Materials*, vol. 33, no. 43, p. 2104793, Oct. 2021, doi: https://doi.org/10.1002/adma.202104793.

[135] J. Tang *et al.*, "Liquid-Metal-Enabled Mechanical-Energy-Induced CO2 Conversion," *Advanced Materials*, vol. n/a, no. n/a, p. 2105789, Oct. 2021, doi: https://doi.org/10.1002/adma.202105789.

[136] M. Wang, C. Trlica, M. R. Khan, M. D. Dickey, and J. J. Adams, "A reconfigurable liquid metal antenna driven by electrochemically controlled capillarity," *J Appl Phys*, vol. 117, no. 19, p. 194901, May 2015, doi: 10.1063/1.4919605.

[137] J. Yang, X. Wu, J. Song, C. Huang, Y. Huang, and X. Luo, "Cascaded metasurface for simultaneous control of transmission and reflection," *Opt Express*, vol. 27, no. 6, p. 9061, Mar. 2019, doi: 10.1364/oe.27.009061.

[138] "Metallic gallium alloy as a thermometer fluid," May 2003.

[139] D. Kim *et al.*, "Recovery of nonwetting characteristics by surface modification of gallium-based liquid metal droplets using hydrochloric acid vapor," *ACS Appl Mater Interfaces*, vol. 5, no. 1, pp. 179–185, Jan. 2013, doi: 10.1021/am302357t.

[140]   C. Ladd, J.-H. So, J. Muth, and M. D. Dickey, "3D Printing of Free Standing Liquid Metal Microstructures," *Advanced Materials*, vol. 25, no. 36, pp. 5081–5085, Sep. 2013, doi: 10.1002/adma.201301400.

[141]   D. Kim, Y. Lee, D. W. Lee, W. Choi, K. Yoo, and J. B. Lee, "Hydrochloric acid-impregnated paper for gallium-based liquid metal microfluidics," *Sens Actuators B Chem*, vol. 207, no. Part A, pp. 199–205, Feb. 2015, doi: 10.1016/j.snb.2014.09.108.

[142]   L. Tian, M. Gao, and L. Gui, "A Microfluidic Chip for Liquid Metal Droplet Generation and Sorting," *Micromachines*, vol. 8, no. 2. 2017. doi: 10.3390/mi8020039.

[143]   Y. Chen *et al.*, "Liquid metal droplets with high elasticity, mobility and mechanical robustness," *Mater Horiz*, vol. 4, no. 4, pp. 591–597, Jul. 2017, doi: 10.1039/c7mh00065k.

[144]   Z. Chen and J. B. Lee, "Surface Modification with Gallium Coating as Nonwetting Surfaces for Gallium-Based Liquid Metal Droplet Manipulation," *ACS Appl Mater Interfaces*, vol. 11, no. 38, pp. 35488–35495, 2019, doi: 10.1021/acsami.9b12493.

[145]   Y. Chen *et al.*, "Robust Fabrication of Nonstick, Noncorrosive, Conductive Graphene-Coated Liquid Metal Droplets for Droplet-Based, Floating Electrodes," *Adv Funct Mater*, vol. 28, no. 8, p. 1706277, Feb. 2018, doi: 10.1002/adfm.201706277.

[146]   D. Kim *et al.*, "Stretchable and bendable carbon nanotube on PDMS super-lyophobic sheet for liquid metal manipulation," *Journal of Micromechanics and Microengineering*, vol. 24, no. 5, p. 055018, Apr. 2014, doi: 10.1088/0960-1317/24/5/055018.

[147]   I. D. Joshipura *et al.*, "Patterning and Reversible Actuation of Liquid Gallium Alloys by Preventing Adhesion on Rough Surfaces," *ACS Appl Mater Interfaces*, vol. 10, no. 51, pp. 44686–44695, Dec. 2018, doi: 10.1021/acsami.8b13099.

[148]   "Espacenet – search results." https://worldwide.espacenet.com/patent/search/family/006465874/publication/US6019509A?q=pn%3D US6019509A (accessed Jun. 09, 2021).

[149]   A. Fujimoto, Y. Yamada, M. Koinuma, and S. Sato, "Origins of sp3C peaks in C1s X-ray Photoelectron Spectra of Carbon Materials," *Anal Chem*, vol. 88, no. 12, pp. 6110–6114, Jun. 2016, doi: 10.1021/acs.analchem.6b01327.

[150]   Y. Cheng *et al.*, "Structural, morphological, FTIR and photoluminescence properties of gallium oxide thin films," *Journal of Vacuum Science & Technology B, Nanotechnology and Microelectronics: Materials, Processing, Measurement, and Phenomena*, vol. 32, no. 3, p. 03D119, 2014, doi: 10.1116/1.4868523.

[151]   J. Ma *et al.*, "Metallophobic Coatings to Enable Shape Reconfigurable Liquid Metal Inside 3D Printed Plastics," *ACS Appl Mater Interfaces*, vol. 13, no. 11, pp. 12709–12718, Mar. 2021, doi: 10.1021/acsami.0c17283.

[152]   R. K. Kramer, J. W. Boley, H. A. Stone, J. C. Weaver, and R. J. Wood, "Effect of Microtextured Surface Topography on the Wetting Behavior of Eutectic Gallium–Indium Alloys," *Langmuir*, vol. 30, no. 2, pp. 533–539, Jan. 2014, doi: 10.1021/la404356r.

[153]   M. Guvendiren, J. Molde, R. M. D. Soares, and J. Kohn, "Designing Biomaterials for 3D Printing," *ACS Biomater Sci Eng*, vol. 2, no. 10, pp. 1679–1693, Oct. 2016, doi: 10.1021/acsbiomaterials.6b00121.

[154]   I. T. Ozbolat and Y. Yu, "Bioprinting toward organ fabrication: Challenges and future trends," *IEEE Trans Biomed Eng*, vol. 60, no. 3, pp. 691–699, 2013, doi: 10.1109/TBME.2013.2243912.

[155]   M. Silva, I. S. Pinho, J. A. Covas, N. M. Alves, and M. C. Paiva, "3D printing of graphene-based polymeric nanocomposites for biomedical applications," *Functional Composite Materials*, vol. 2, no. 1, 2021, doi: 10.1186/s42252-021-00020-6.

[156]   P. Kumar, D. K. Rajak, M. Abubakar, S. Gazanfar, M. Ali, and M. Hussain, "3D Printing Technology for Biomedical Practice : A Review," *J Mater Eng Perform*, 2021, doi: 10.1007/s11665-021-05792-3.

[157] X. Chen *et al.*, "Scaffold Structural Microenvironmental Cues to Guide Tissue Regeneration in Bone Tissue Applications," *Nanomaterials*, vol. 8, no. 11, Nov. 2018, doi: 10.3390/NANO8110960.

[158] J. Koprnicky, J. Safka, and M. Ackermann, "Using of 3D printing technology in low cost prosthetics," *Materials Science Forum*, vol. 919, pp. 199–206, 2018, doi: 10.4028/WWW.SCIENTIFIC.NET/MSF.919.199.

[159] "Design and optimization of prosthetic foot by - ProQuest." https://www.proquest.com/docview/2001517744 (accessed Jan. 16, 2023).

[160] R. Boorla and T. Prabeena, "Fabrication of patient specific knee implant by fused deposition modeling," *Material Today*, vol. 18, pp. 3638–3642, 2019.

[161] B. I. Oladapo, S. A. Zahedi, and A. O. M. Adeoye, "3D Printing of bone scaffolds with hybrid biomaterials," *Composites Part B: Eng.*, vol. 158, pp. 428–436, 2019.

[162] B. Hu *et al.*, "Improved design of fused deposition modeling equipment for 3D printing of high-performance PEEk parts," *Mech. Mater.*, vol. 137, p. P103139, 2019.

[163] Y. Li, B. S. Linke, H. Voet, B. Falk, R. Schmitt, and M. Lam, "Cost sustainability and surface roughness quality-a comprehensive analysis of products made with personal 3D printers," *CIRPJ. Manufacturing Sci. Technol.*, vol. 16, pp. 1–11, 2017.

[164] H. Singh and S. Bhattacharjee, "Fundamentals of Food Printing," *Food Printing: 3D Printing in Food Industry*, pp. 19–34, 2022, doi: 10.1007/978-981-16-8121-9_2.

[165] S. Preethi Soundarya, A. Haritha Menon, S. Viji Chandran, and N. Selvamurugan, "Bone tissue engineering: Scaffold preparation using chitosan and other biomaterials with different design and fabrication techniques," *Int J Biol Macromol*, vol. 119, pp. 1228–1239, Nov. 2018, doi: 10.1016/J.IJBIOMAC.2018.08.056.

[166] T. Oner *et al.*, "3D Segmentation of intervertebral discs: from concept to the fabrication of patient-specific scaffolds," *J.3D Printing Med.*, vol. 1, pp. 91–101, 2017.

[167] A. E. Jakus *et al.*, "Hyperelastic 'bone': A highly versatile, growth factor-free, osteoregenerative, scalable, and surgically friendly biomaterial," *Sci Transl Med*, vol. 8, no. 358, Sep. 2016, doi: 10.1126/SCITRANSLMED.AAF7704.

[168] S. H. Jariwala, G. S. Lewis, Z. J. Bushman, J. H. Adair, and H. J. Donahue, "3D Printing of Personalized Artificial Bone Scaffolds," *3D Print Addit Manuf*, vol. 2, no. 2, pp. 56–64, Jun. 2015, doi: 10.1089/3DP.2015.0001.

[169] V. Tuncay and P. M. A. van Ooijen, "3D printing for heart valve disease: a systematic review," *Eur Radiol Exp*, vol. 3, no. 1, p. 9, Feb. 2019, doi: 10.1186/S41747-018-0083-0/FIGURES/6.

[170] E. L. Nyberg *et al.*, "3D-Printing Technologies for Craniofacial Rehabilitation, Reconstruction, and Regeneration," *Ann Biomed Eng*, vol. 45, no. 1, pp. 45–57, Jan. 2017, doi: 10.1007/S10439-016-1668-5.

[171] M. Rautamo, K. Kvarnström, M. Sivén, M. Airaksinen, P. Lahdenne, and N. Sandler, "Benefits and Prerequisites Associated with the Adoption of Oral 3D-Printed Medicines for Pediatric Patients: A Focus Group Study among Healthcare Professionals," *Pharmaceutics 2020, Vol. 12, Page 229*, vol. 12, no. 3, p. 229, Mar. 2020, doi: 10.3390/PHARMACEUTICS12030229.

[172] G. Beevers, G. Y. H. Lip, and E. O'Brien, "Blood pressure measurement," *BMJ*, vol. 322, no. 7292, pp. 981 LP – 985, Apr. 2001, doi: 10.1136/bmj.322.7292.981.

[173] S. Thavarajah, W. B. White, and G. A. Mansoor, "Terminal digit bias in a specialty hypertension faculty practice," *J Hum Hypertens*, vol. 17, no. 12, pp. 819–822, 2003, doi: 10.1038/sj.jhh.1001625.

[174] D. Dias, J. Paulo, and S. Cunha, "Wearable Health Devices-Vital Sign Monitoring, Systems and Technologies", doi: 10.3390/s18082414.

[175] G. Ogedegbe and T. Pickering, "Principles and techniques of blood pressure measurement," *Cardiol Clin*, vol. 28, no. 4, pp. 571–586, 2010, doi: 10.1016/j.ccl.2010.07.006.

[176] R. Mukkamala *et al.*, "Toward Ubiquitous Blood Pressure Monitoring via Pulse Transit Time: Theory and Practice," *IEEE Trans Biomed Eng*, vol. 62, no. 8, pp. 1879–1901, Aug. 2015, doi: 10.1109/TBME.2015.2441951.

[177] X. Ding and Y. T. Zhang, "Pulse transit time technique for cuffless unobtrusive blood pressure measurement: from theory to algorithm," *Biomed Eng Lett*, vol. 9, no. 1, p. 37, Feb. 2019, doi: 10.1007/S13534-019-00096-X.

[178] K. Nightingale, M. S. Soo, R. Nightingale, and G. Trahey, "Acoustic radiation force impulse imaging: in vivo demonstration of clinical feasibility," *Ultrasound Med Biol*, vol. 28, no. 2, pp. 227–235, Feb. 2002, doi: 10.1016/S0301-5629(01)00499-9.

[179] M. L. Palmeri, J. J. Dahl, D. B. Macleod, S. A. Grant, and K. R. Nightingale, "On the feasibility of imaging peripheral nerves using acoustic radiation force impulse imaging," *Ultrason Imaging*, vol. 31, no. 3, pp. 172–182, Jul. 2009, doi: 10.1177/016173460903100303.

[180] S. A. Eyerly, S. J. Hsu, S. H. Agashe, G. E. Trahey, Y. Li, and P. D. Wolf, "An In Vitro Assessment of Acoustic Radiation Force Impulse Imaging for Visualizing Cardiac Radiofrequency Ablation Lesions," *J Cardiovasc Electrophysiol*, vol. 21, no. 5, pp. 557–563, May 2010, doi: 10.1111/J.1540-8167.2009.01664.X.

[181] K. Nightingale, "Acoustic Radiation Force Impulse (ARFI) Imaging: a Review," *Curr Med Imaging Rev*, vol. 7, no. 4, p. 328, Nov. 2011, doi: 10.2174/157340511798038657.

[182] L. Demi, "Practical Guide to Ultrasound Beam Forming: Beam Pattern and Image Reconstruction Analysis," *Applied Sciences 2018, Vol. 8, Page 1544*, vol. 8, no. 9, p. 1544, Sep. 2018, doi: 10.3390/APP8091544.

[183] S. Latha, D. Samiappan, and R. Kumar, "Carotid artery ultrasound image analysis: A review of the literature," *Proc Inst Mech Eng H*, vol. 234, no. 5, pp. 417–443, May 2020, doi: 10.1177/0954411919900720.

[184] H. A. Chami *et al.*, "Brachial Artery Diameter, Blood Flow and Flow-mediated Dilation in Sleep-Disordered Breathing," *Vasc Med*, vol. 14, no. 4, p. 351, 2009, doi: 10.1177/1358863X09105132.

[185] I. Wendelhag, T. Gustavsson, M. Suurküla, G. Berglund, and J. Wikstrand, "Ultrasound measurement of wall thickness in the carotid artery: fundamental principles and description of a computerized analysing system," *Clinical Physiology*, vol. 11, no. 6, pp. 565–577, 1991, doi: 10.1111/j.1475-097X.1991.tb00676.x.

[186] C. K. McGarry *et al.*, "Tissue mimicking materials for imaging and therapy phantoms: A review," *Phys Med Biol*, vol. 65, no. 23, 2020, doi: 10.1088/1361-6560/abbd17.

[187] W. A. Riley, R. W. Barnes, G. W. Evans, and G. L. Burke, "Ultrasonic measurement of the elastic modulus of the common carotid artery: The atherosclerosis risk in communities (aric) study," *Stroke*, vol. 23, no. 7, pp. 952–956, 1992, doi: 10.1161/01.STR.23.7.952.

[188] V. Kumar, Balendra, and A. Sahani, "A brute force methodology for automated data extraction and analysis for Finite Element Analysis," in *2022 IEEE Delhi Section Conference (DELCON)*, 2022, pp. 1–4. doi: 10.1109/DELCON54057.2022.9753247.

[189] "KerasTuner." https://keras.io/keras_tuner/ (accessed Oct. 06, 2022).

[190] A. I. Farrer *et al.*, "Characterization and evaluation of tissue-mimicking gelatin phantoms for use with MRgFUS.," *J Ther Ultrasound*, vol. 3, p. 9, 2015, doi: 10.1186/s40349-015-0030-y.

[191] J. Zhang *et al.*, "Structural damage identification using damping: a compendium of uses and features," *Smart Mater Struct*, vol. 26, no. 4, p. 043001, Mar. 2017, doi: 10.1088/1361-665X/AA550A.

[192] P. K. et al. Whelton, "2017 ACC/AHA/AAPA/ABC/ACPM/AGS/APhA/ASH/ASPC/NMA/PCNA Guideline for the Prevention, Detection, Evaluation, and Management of High Blood Pressure in Adults: A Report of the American College of Cardiology/American Heart Association Task Force on Clinical Pr," *Hypertension*, vol. 71, no. 6, pp. e13–e115, 2018.

[193]   D. et al. Ettehad, "Blood pressure lowering for prevention of cardiovascular disease and death: a systematic review and meta-analysis," *The Lancet*, vol. 387, no. 10022, pp. 957–967, 2016.

[194]   P. et al. Muntner, "Measurement of Blood Pressure in Humans: A Scientific Statement From the American Heart Association," *Hypertension*, vol. 73, no. 5, pp. e35–e66, 2019.

[195]   Ş. Ulusoy, G. Özkan, B. Güvercin, Y. Sökmen, and Y. Erdem, "Do physicians measure patients' blood pressure, and are those measurements reliable?," *J Hum Hypertens*, vol. 32, no. 3, pp. 203–211, Mar. 2018.

[196]   S. S. Franklin, L. Thijs, T. W. Hansen, E. O'Brien, and J. A. Staessen, "White-Coat Hypertension," *Hypertension*, vol. 62, no. 6, pp. 982–987, 2013.

[197]   J. E. Sharman and T. H. Marwick, "Accuracy of blood pressure monitoring devices: a critical need for improvement that could resolve discrepancy in hypertension guidelines," *Journal of human hypertension V1 - 33*.

[198]   C. D. Deakin and J. L. Low, "Accuracy of the advanced trauma life support guidelines for predicting systolic blood pressure using carotid, femoral, and radial pulses: observational study," *BMJ V1 - 321*, pp. 673–674, 2000.

[199]   B. Shahbabu, A. Dasgupta, K. Sarkar, and S. K. Sahoo, "Which is more accurate in measuring the blood pressure? A digital or an aneroid sphygmomanometer," *Journal of Clinical and Diagnostic Research*, vol. 10, no. 3, pp. LC11–LC14, Mar. 2016, doi: 10.7860/JCDR/2016/14351.7458.

[200]   S. Ghareeb *et al.*, "Results of a project to calibrate mercury sphygmomanometer blood pressure-measuring devices in Egypt," *J Hum Hypertens*, 2020, doi: 10.1038/s41371-020-00424-0.

[201]   G. S. Stergiou *et al.*, "A universal standard for the validation of blood pressure measuring devices: Association for the Advancement of Medical Instrumentation/European Society of Hypertension/International Organization for Standardization (AAMI/ESH/ISO) Collaboration Statement," *Hypertension*, vol. 71, no. 3, pp. 368–374, 2018, doi: 10.1161/HYPERTENSIONAHA.117.10237.

[202]   E. Casiglia, V. Tikhonoff, F. Albertini, and P. Palatini, "Poor Reliability of Wrist Blood Pressure Self-Measurement at Home: A Population-Based Study," *Hypertension*, vol. 68, no. 4, pp. 896–903, Oct. 2016, doi: 10.1161/HYPERTENSIONAHA.116.07961.

[203]   G. Sarganas, R. Kuhnert, C. Gohlisch, M. van der Giet, and H. Neuhauser, "Comparison of two blood pressure oscillometric devices: Datascope Accutorr Plus and Mobil-O-Graph PWA and conversion of blood pressure values from one device to the other," *Blood Press Monit*, vol. 25, no. 1, 2020.

[204]   E. Shalom *et al.*, "Systolic blood pressure measurement by detecting the photoplethysmographic pulses and electronic Korotkoff-sounds during cuff deflation," *Physiol Meas*, vol. 41, no. 3, 2020, doi: 10.1088/1361-6579/ab7b41.

[205]   B. G. Celler, P. N. Le, A. Argha, and E. Ambikairajah, "Blood Pressure Estimation Using Time Domain Features of Auscultatory Waveforms and GMM-HMM Classification Approach," *Conf Proc IEEE Eng Med Biol Soc*, vol. 2019, pp. 208–211, 2019, doi: 10.1109/EMBC.2019.8857920.

[206]   F. Pan, P. He, F. Chen, J. Zhang, H. Wang, and D. Zheng, "A novel deep learning based automatic auscultatory method to measure blood pressure," *Int J Med Inform*, vol. 128, pp. 71–78, 2019, doi: https://doi.org/10.1016/j.ijmedinf.2019.04.023.

[207]   M. Waldron, S. David Patterson, and O. Jeffries, "Inter-Day Reliability of Finapres (®) Cardiovascular Measurements During Rest and Exercise.," *Sports Med Int Open*, vol. 2, no. 1, pp. E9–E15, Jan. 2018, doi: 10.1055/s-0043-122081.

[208]   F. Heydari *et al.*, "Clinical study of a chest-based cuffless blood pressure monitoring system," *Med Devices Sens*, vol. 3, no. 5, p. e10091, Oct. 2020, doi: 10.1002/MDS3.10091.

[209]   B. Silke and D. McAuley, "Accuracy and precision of blood pressure determination with the Finapres: an overview using re-sampling statistics," *J Hum Hypertens*, vol. 12, no. 6, pp. 403–409, 1998, doi: 10.1038/sj.jhh.1000600.

[210] Y. Ostchega, R. J. Prineas, T. Nwankwo, and G. Zipf, "Assessing Blood Pressure Accuracy of an Aneroid Sphygmomanometer in a National Survey Environment," *Am J Hypertens*, vol. 24, no. 3, pp. 322–327, Mar. 2011, doi: 10.1038/AJH.2010.232.

[211] J. N. Amoore, "Oscillometric sphygmomanometers: a critical appraisal of current technology," *Blood Press Monit*, vol. 17, no. 2, pp. 80–88, Apr. 2012, doi: 10.1097/MBP.0B013E32835026B0.

[212] R. Kumar and A. K. Sahani, "A Device to Reduce Vasovagal Syncope in Blood Donors," *Annu Int Conf IEEE Eng Med Biol Soc*, vol. 2021, pp. 2136–2139, Nov. 2021, doi: 10.1109/EMBC46164.2021.9630891.

[213] M. Kumar, R. Kumar, V. Kumar, A. Chander, V. Gupta, and A. K. Sahani, "A Low-cost Ambu-bag Based Ventilator for Covid-19 Pandemic," *2021 IEEE Biomedical Circuits and Systems Conference (BioCAS)*, pp. 1–5, Oct. 2021, doi: 10.1109/BIOCAS49922.2021.9644985.

Appendix

DAYANAND MEDICAL COLLEGE & HOSPITAL
LUDHIANA

Institutional Ethics Committee

Ref No. :- DMCH/R&D/2021/58

Date :- 3|5|21

Dr. Gurpreet S Wander,
Professor & Head
Dept. of Cardiology,
DMC & H, Ludhiana

Ref: IEC No: 2021-654 "A comparative study of Galinstan based Sphygmomanometer with traditional Mercury Sphygmomanometer & Oscillometric BP apparatus"

Subject: Institutional Ethics Committee (IEC) Approval

Dear Dr. Wander,

The Institutional Ethics Committee (IEC) reviewed, discussed & approved your research project in its meeting held on **29-05-2021 (Saturday)** at **11:00** am on Zoom in Research & Development Centre, DMC & Hospital, Ludhiana.

The IEC should be informed:

1. About the progress of the study.
2. Any Serious Adverse Events occurring in the course of the study within 24 hours of their occurrence.
3. Any changes in ICF and other documents.
4. Protocol Deviation(s).
5. Any change in the protocol and patient information/informed consent documents, prior to their implementation.

Page: 1 of 2

Principal	: 0161 4687501	EPABX	: 0161 4687777, Ext 7395
Medical Supdt.	: 0161 4687504	Fax	: 0161 2302620
Dean Academics	: 0161 4687503	DMC Email	: dmchldh@glide.net.in
		Website	: www.dmch.edu

106

DAYANAND MEDICAL COLLEGE & HOSPITAL
LUDHIANA

Institutional Ethics Committee

Ref No. :- DMCH/R&D/2021/5R

Date :- 31|5|21

The Final report of the study shall be submitted to Ethics Committee, even if the study is abandoned for any reason(s). Please Inform the IEC in case of any change of study procedure, site and investigator. This permission is only for period mentioned above. Annual report will have to be submitted to IEC. Members of IEC have right to monitor the trial with prior intimation.

Moreover, please submit any abstract/full papers that are presented/published thereof as early as possible to the ethics committee office.

Kind regards,

Dr. Gagandeep Singh

Secretary
Institutional Ethics Committee (IEC)
Dayanand Medical College & Hospital
Addendum:-The Following members of the IEC were present in the meeting held on 29-05-21 and were involved in the approval process:

Sr. No	Members	Designation
1.	Prof. Arvind Malhotra	Chairman
2.	Prof. Gagandeep Singh	Member Secretary
3.	Prof. Sandeep Kaushal	Member
4.	Prof Anu Sharma	Member
5.	Prof. Ramit Mahajan	Member
6.	Prof Sanjeev K Uppal	Member
7.	Adv. R K Sharma	Member
8.	Mrs. Rashi Gupta	Member
9.	Mrs. Leena Chopra	Member

Dr. Gurpreet S Wander did not participate in the voting process being part of the study.

Page: 2 of 2

PARTICPANT INFORMED CONSENT FORM (PICF)

Protocol Study number: __2021-654__ Patient identification number for this study: _____ Title of the project: **A comparative study of Galinstan based Sphygmomanometer with traditional Mercury Sphygmomanometer & Oscillometric BP apparatus.** Name of Principal investigator: **Dr Gurpreet Singh Wander** Tel. No(s)_____ The contents of the information sheet dated_____ that was provided have been read carefully by me / explained in detail to me, in a language that I comprehend, and I have fully understood the contents. I confirm that I have had the opportunity to ask questions. The nature and purpose of the study and its potential risks / benefits and expected duration of the study, and other relevant details of the study have been explained to me in detail. I understand that my participation is voluntary and that I am free to withdraw from the study at any time, without giving any reason, without my medical care or legal right being affected. I understand that the information collected about me from my participation in this research and sections of any of my medical notes may be looked at by responsible individuals from Dayanand Medical College & Hospital, Ludhiana. I give permission for these individuals to have access to my records. I also give my consent to publish my data for academic purposes provided my identity is kept confidential. I agree to take part in the above study.

--------------------------------- Date:

(Signatures / Left Thumb Impression) Place:

Name of Participant: __SHAILLY KATOCH__ Son/Daughter/spouse of: MR. RAKESH THAKUR
Complete postal address: V.P.O. Majherna, Teh. Baijnath, Dist. Kangra - 1441-176063 HP

This is to certify that the above consent has been obtained in my presence.

Signatures of the Principal Investigator Date:

Place:

1) Witness – 1

--------------- Muskan

Signature

Name: MUSKAN (CRC)

Address: HCIO DMC Heart Inst Ludhiana.

2) Witness – 2

Signature

Name: Hamith (Nurse)

Address: HDHI LDH

108